MICROTWEEZERS FOR STUDYING VIBRATING CARBON NANOTUBES

A Dissertation

Presented to the Faculty of the Graduate School

of Cornell University

in Partial Fulfillment of the Requirements for the Degree of

Doctor of Philosophy

by

Arthur William Barnard

January 2015

MICROTWEEZERS FOR STUDYING VIBRATING CARBON NANOTUBES

Arthur William Barnard, Ph.D.

Cornell University 2015

Vibrational modes in suspended carbon nanotubes (CNTs) are incredibly soft, which makes them sensitive to small forces and prime candidates as force sensors. This same property, combined with the stiffness of the CNT to stretching, makes them an unusual mechanical system characterized both by large thermally-activated fluctuations and strong nonlinear interactions between the resonance modes. To understand how these thermal fluctuations manifest themselves in the resonance of CNTs, we developed an electrically-contacted micro-tweezer platform. The platform is capable of lifting a pristine CNT off of its growth substrate, directly applying strain to the free-standing doubly-clamped CNT, and controlling its proximity to electrical gates. Using the unprecedented level of measurement precision offered by our novel setup, we preformed the first-ever single-shot ring-down measurements on CNTs, to map the resonance spectra as a function of strain and we directly measured the thermal motion of single-walled CNTs at room temperature. These measurements, in agreement with our original theoretical predictions, convincingly show that thermally-inducted fluctuations of CNT resonance modes are in fact the source of the remarkably high mechanical dissipation that has been ubiquitously observed in room-temperature CNT resonators. This result is not material dependent and the underlying physics should apply to all nanoscale 1D resonators.

In addition to this key result, we use the microtweezer platform to couple CNT resonators to high-Q optical microdisk resonators. With this hybrid system, we demonstrate remarkably strong optomechanical coupling and make the first-ever observation of the optical spring-effect on CNT mechanical resonators.

BIOGRAPHICAL SKETCH

Arthur Barnard was born in Delmar, NY in 1986. Upon graduating from Bethlehem high in 2004, he began his college education at Cornell University in Ithaca NY. During his undergraduate years he actively explored various research areas and was recognized with the Paul Hartmann prize in experimental physics when he graduated with a B.S. in Applied Engineering Physics in 2008. He then decided to continue his graduate work under the guidance of Prof. Paul McEuen at Cornell University with whom he had started work as an undergraduate researcher. Arthur will move out of New York state for the first time to start his postdoctoral research at Stanford University.

Dedicated to my parents

ACKNOWLEDGMENTS

This thesis marks the conclusion of over ten years of time spent at Cornell, and thus is a notable milestone for me personally as well as academically. I have had the great privilege of spending the majority of my adult life doing work that I love and getting to learn from passionate educators and motivated colleagues. While research was both my vocation and my hobby, the people with whom I was interacted made this decade most meaningful.

First and foremost, I would like my adviser Professor Paul McEuen. I would like to thank Paul for giving me the space and resources to engage my scientific curiosities and for being a kind and responsive adviser throughout. I would also like to thank Prof. Jiwoong Park for being on my thesis committee and for regular scientific exchanges and candid advice regarding professional matters. Finally, I would like to thank Prof. Mukund Vengalattore, whose experimental work has always inspired me, for being on my committee.

I would like to thank Prof. Michal Lipson and Mian Zhang for their time and contributions to our studies of carbon-based opto-mechanics.

Working in the McEuen group has been extraordinarily rewarding, both for the breadth of research experience it afforded me, as well as the chance to work alongside a group of inspired, inspiring, and well-rounded individuals. During the course of my time in the group I have been fortunate to work with many graduate students, post docs and , undergraduate researchers. I would like to thank the senior members of the group (Nate, Arend, Luke, Scott, Xiadong, Zaohui, Yaqiong) for setting high expectations; my research contemporaries for their valuable scientific exchange and continued support (Melina, Sam, Jonathan, Issac), and the newer members of the group (Kathryn, Peter, Alejandro) for their enthusiasm and patience for my disorganization. A special thanks to Sam for her kindness, generosity, and close friendship over the years.

I would like to thank the various members of the Stewart Little co op. for making sure that I

was well fed and socially engaged during the hectic final years of graduate school.

Last but not least I would like to thank my family for their continued support. My parents for an upbringing that nurtured my general curiosity and my brothers and dad for engaging in regular scientific discourse. Finally I would like to thank my wife, Chinmayee, for her constant enthusiasm and loving companionship.

CONTENTS

LIST OF FIGURES

Chapter 1

Introduction

Carbon nanotubes (CNTs) are a unique macromolecule, formed by a hexagonal lattice of carbon atoms seamlessly stitched into a cylinder. These cylinders can be arbitrarily long, while their diameters can be as small as a few atoms across [1]. The underlying carbon lattice endows CNTs with a host of attractive properties like their superior mechanical strength, conductivity, and chemical stability while their small diameters are the source of emergent nanoscale phenomena including exotic optical and electronic properties. The overlap of their robustness and their intrinsic dimensionality has led CNTs to be extensively studied both for their fundamental physical characteristics and for their role as active elements in applied technologies.

For example, the mechanical strength and extremely small size of CNTs, both in terms of mass and bending rigidity [2], endows CNTs with unique and attractive resonance properties that have been studied and exploited in diverse experimental manifestations. Specifically, since the first realization of a CNT electromechanical resonator in 2004 by V. Sazonova et. al [3], a spur of research in the area has demonstrated the CNT resonators are remarkably tunable and extremely sensitive to their surroundings [3–5], while having intrinsic mechanical resonance frequencies that can be exploited in radio frequency electronics [6]. In fact, as a result of their extreme sensitivity, researchers have observed strong coupling between electronic and mechanical degrees of freedom [7]. Further, the high sensitivity has also been exploited for mass-sensing applications [5,8–11], resulting in the ability to weigh a single proton [5].

While these remarkable accomplishments are made possible by the well-studied electronic [12–15] and static mechanical properties of CNTs [2], the most basic understanding of the dynamical properties of vibrating CNTs has been perplexing. For example, CNTs resonances exhibit apparent dissipation far exceeding that of any well-understood dissipation mechanisms observed in other nano-mechanical systems, and furthermore, this dissipation proves to be highly-dependent on both device geometry and temperature.

It is in the context of trying to understand these emergent physical phenomena where the research contributions presented in this thesis begin. In chapter 2, we explore the intuition from polymer physics that thermal fluctuations can dramatically alter the mechanical behavior of nanoscale polymers and we relate this to CNT resonator dissipation. Our analysis [16] consists of performing numerical simulations of thermally activated, free-standing CNTs, and developing a mean-field theory to describe their observed behavior (both in tensioned and in buckled CNT resonators). While there have been several previous theoretical attempts to understand dissipation in CNT resonators [17–19, 19–21] , our work was the first to propose a mechanism that made predictions that were in good quantitatively agreement with past experimental observations.

Our theoretical work also showed the important role of mechanical strain in influencing CNT resonator dissipation. This served to highlight the fact that there is an inherent confounding attribute of on-chip CNT resonator fabrication: there is a fixed, built-in strain which is difficult to accurately characterize. While on-chip fabrication is clearly attractive and justified in many cases, the need to control and modify the geometry of free-standing CNTs led us to develop a new technique for picking up and manipulating CNTs in diverse environments.

Nanomanipulation of CNTs is certainly not without precedent [22–25], and has been employed since the early days after the first discovery of carbon nanotubes [26] Most notably, CNTs have been attached to atomic force microscope tips in order create ultra-sharp mechanical probes [22]. Invariably, however, due to their small size, picking up and manipulating CNTs is a complex process and has traditionally relied on piezo actuators installed inside of electron microscopes. While novel

use of these tools is an impressive feat, the complexity of the apparatus as well as the inherently harsh environment in electron microscopes has hampered the widespread use of nanomanipulated CNTs in technological or scientific pursuits.

Our contribution to the realm of nanomanipulation of CNTs is the development of a micro-tweezer apparatus (Chapter 3) that can pick up an electrically contacted CNT from a growth substrate using basic electrical detection and standard optics. The tweezer system is designed with a specific focus on applying controllable strain to CNTs as their resonance properties are measured electrically. Our method is a cost-effective means of rapidly searching for and finding CNTs.

Prior to describing our main experimental results regarding CNT resonators, we discuss a series of novel experiments with the micro-tweezer system (Chapter 4), outside the framework of CNT resonators. In particular we show various applications of scanned-laser microscopy, in order to study freestanding CNTs as they are manipulated in diverse environments.

In Chapter 5, we detail our measurements of CNT resonator thermal mechanics and show how fluctuation broadening (the effect we predict in chapter 2) does, in fact, seem to explain the observed dissipation in CNT resonators—our main key result. In service of this goal, we refined a number of sensitive measurement techniques and were able to directly measure the room temperature fluctuations of CNT resonators and perform the first-ever ringdown measurements on CNT resonators. These new tools allowed us to gain further insight into the emergent thermal physics of reduced dimensional systems.

Finally, among the various possible applications of the tweezer system, we examined the opto-mechanical coupling of CNTs to optically resonant cavities (Chapter 6). The field of cavity optomechanics studies numerous phenomena arising from the enhanced coupling of light to mechanics, including optical cooling and parametric amplification [27,28] and has promise in the realm of quantum computation [29–32]. While various nanomechanical structures have been coupled to optical cavities [31, 33, 34], the prospect of doing so with CNTs is particularly promising due to their soft spring constants, their varied optical properties, and their ability to be manipulated and detected

electrically. Collaborating with Prof. Michal Lipsons group at Cornell and employing their expertise in optical microdisk resonators, we were able to measure the optical cross-section of a CNT, map optical cavities evanescent field with subwavelength precision, as well as demonstrate the optical spring effect in a CNT mechanical resonance mode. This was the first-ever demonstration of optical stiffening of a CNT resonance mode.

The work in this thesis amounts to two intertwined lines of research; one technical and the other scientific. We proposed a theoretical explanation for an emergent physical phenomenon experienced by CNT resonators, built the necessary tools to study it, and ultimately performed measurements that supported our theory. In the process of this pursuit, the novel nanomanipulation tools we constructed became instrumental in realizing new, promising measurement schema.

Chapter 2

Theory of fluctuation broadening in carbon nanotube resonators

Carbon nanotube (CNT) resonators, with their nanometer-scale cross section [1] and very small bending rigidity for flexural modes [2], exist in a unique regime where thermal fluctuations of individual resonance modes may drastically affect resonance properties such as the quality factor Q. In overdamped environments such as liquids, the effects of thermal fluctuations have been studied for decades [35], but the behavior of reduced elastic objects (such as CNTs) in *underdamped* environments is largely unexplored. Experimental work has shown CNT resonators to be highly tunable [36] as well as functional as RF transceivers [6] and atomic mass detectors [8, 9], but these resonators have consistently exhibited much broader than expected decay widths, or in other words, low Qs [3, 36]. Specifically, the quality factor Q, the key parameter measuring the degree to which an oscillating mode is decoupled from its environment, is typically less than $Q \sim 100$ at room temperature. These low Qs are not consistent with known dissipation mechanisms seen in other nanomechanical resonator systems [17]. Analytical phonon-phonon scattering studies establish a theoretical upper bound on Q in CNTs that is well above experimental values, with $Q \lesssim 50,000$ at 300 K [10, 37]. Molecular-dynamics simulations of short CNTs ($L \sim 50nm$) show interesting behaviors in cantilevered and free CNT segments [18–21] due to anharmonic atomic potentials, and those that make an explicit determination of quality factor in thermal equilibrium [19, 20] give

$Q \sim 1,000$ at room temperature. Typically, however, experiments are performed on CNTs with $L \gtrsim 1\ \mu m$, and the anharmonic elastic effects that dominate in short length CNTs do not contribute significantly at this longer length scale.

An alternative explanation for these altered properties comes from the field of polymer physics, where the effects of fluctuations on the physics of 1D elastic objects has a long and storied history. A key length-scale that characterizes their properties is the persistence length $\ell_p = \frac{\kappa}{k_B T}$, where κ is the bending rigidity. Subject to thermal forces, the 1D elastic object will fluctuate and lose correlations in shape for lengths longer than ℓ_p. Thus, short 1D structures ($L \ll \ell_p$) such as microfabricated nanobeam resonators behave like rigid rods, with thermal amplitudes small compared with the size of the structure. On the other hand, long 1D structures ($L \gg \ell_p$) such as organic polymers are forced into fluctuating, coiled, high-entropy configurations. Micron-scale CNTs are between these regimes, in the semiflexible polymer limit ($L \lesssim \ell_p$) [35], where the bending energy and configurational entropy contribute comparably to the total free energy. In overdamped environments, the behavior of semiflexible polymers is now well understood [38], but the behavior of a nanoscale *resonator* in the semiflexible polymer limit has not been explored.

Numerical Model. In light of the typical experimental conditions and the analogy to polymer physics, we model the CNTs as 1D linear-elastic objects. By simulating purely continuum elastic behavior, we isolate the specific influence of entropic forces on measured quantities, including both quality factor and thermally-induced frequency shifts. Quantum mechanical effects are neglected, as the thermal occupation of all modes considered are in the classical limit. CNTs are modeled as elastic beams with bending rigidity $\kappa = \pi \frac{Cd^3}{8}$ and extensional rigidity $K = \pi C d$, where $C \approx 345\ J/m^2$ [39] is the 2D elastic modulus of graphene and d is the tube diameter. Each CNT was discretized into 100 or more masses joined by axial and torsional linear springs, as illustrated in fig. 2.1. For N masses, this yields a system of $3N$ 2^{nd}-order, or $6N$ 1^{st}-order differential equations describing the time dynamics in 3D of all masses. For a given SWCNT, the tubes linear mass

density μ is related to graphenes 2D mass density $\sigma = 7.67 \times 10^{-7} \frac{kg}{m^2}$ by $\mu = \pi d \sigma$. Thus for a given discretization length Δx, this gives a mass of $m = \mu \Delta x = \pi \sigma d \Delta x$. The linear spring constant between masses is then related to the rigidity K by $k_{stretch} = \frac{K}{\Delta x}$. Finally, there is a torque applied proportional to the angle between two adjoining segments related to the bending rigidity κ: $|\tau| = \frac{\kappa}{\Delta x} |\theta|$. With these values, the initial conditions are solved for by numerically approaching a steady state solution using the Newton-Raphson method to find the zero of the $3N \times 3N$ force constant matrix $\frac{\partial^2 U}{\partial x_n \partial x_m}$. Eigenmode shapes and eigenfrequencies at zero temperature are calculated by diagonalizing this force constant matrix.

At finite temperature, the resonance modes are thermalized by including a global damping coefficient γ, and applying stochastic momentum kicks to each mass in all directions, with amplitudes set by γ, the temperature T and the time step size Δt:

$$\frac{\Delta p}{\Delta t} = \sqrt{\frac{6\pi\sigma d k_B T}{\Delta x \Delta t}} U(-1, 1) \tag{2.1}$$

where $U(-1, 1)$ denotes a uniform random distribution in the range from -1 to 1. These kicks constitute a discretized version of the well-known Langevin force. In all of the simulated data in this chapter, $\gamma \leq 250 kHz$ which is smaller than all observed linewidths, and thus not the dominant source of apparent broadening. With the equations of motion set; time series are computed using the 4^{th} order Runge-Kutta method. To further confirm that the imposed damping is not consequential in our simulations; we compared the dynamics to a dissipationless (adiabatic) system using using Stoermers rule [40]. The initial thermal occupation of the resonance modes in the adiabatic case appear sufficient to allow the energy to flow between modes and reproduce the statistics observed in the dissipative case.

Numerical Measurements. Studying the thermally driven dynamics of CNT resonators using our numerical model gives us complete access to the trajectory of the NT motion, allowing us to measure and study the interaction between the many resonance modes in a number of complex ways.

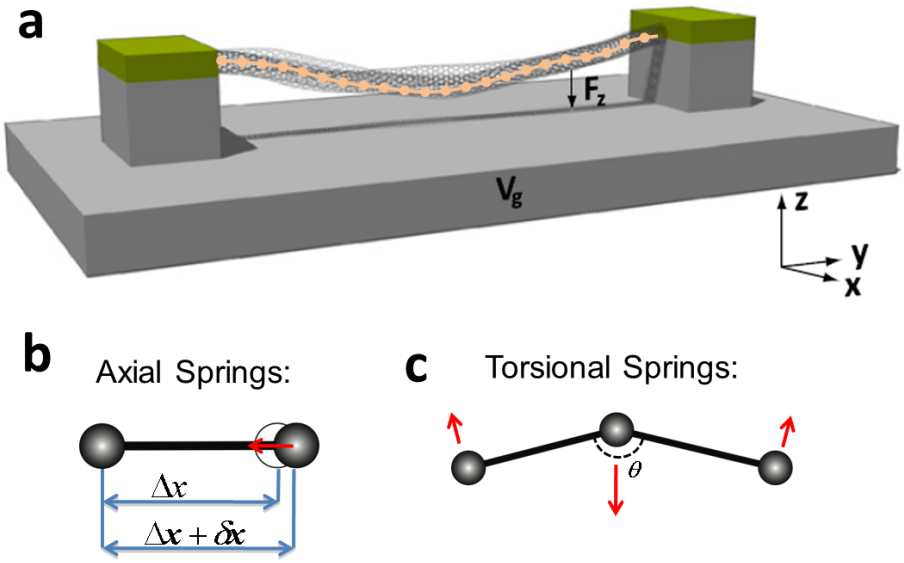

Figure 2.1: a) Schematic of CNT resonator model geometry. CNT is suspended between two electrodes (in yellow) and has a controllable downward force F_z electrostatically applied by a voltage to the underlying substrate. The tube is modeled as a linear-chain of masses and springs. The global stiffnesses of the tube K and κ translate in linear (b) and torsional (c) spring constants based on the separation Δx

For this chapter we focus our simulations on a typical experimental case of a CNT with $L = 3\ \mu m$ and $d = 2\ nm$. We investigate resonance properties of this CNT at different zero-temperature strains ϵ_0, temperatures T, and externally applied forces F_z by quasi-statically sweeping at most one parameter and measuring the power spectral density of the mean z-displacement (defined in Fig. 2.1a) of the nanotube: $S_z(f) = \lim_{t_m \to \infty} E\left[\frac{|\mathcal{F}(z_{t_m}(t))|^2}{t_m}\right]$ where t_m is the finite time over which the Fourier transform is taken and E denotes an ensemble average. The mean z-displacement was the chosen parameter to analyze as it is typically measured in experiments [4]. By virtue of the fluctuation dissipation theorem, $S_z(f)$ serves as a measure of the linear-response function of the CNT system. From $S_z(f)$, we measure thermal frequency shifts $\Delta f \equiv f - f(T = 0K)$ and quality factor $Q \equiv \frac{f}{\delta f}$. This definition of Q is employed as the linewidth δf is directly measured in experiments.

Strain Dependence. We first study the qualitative behavior of this CNT as a function of strain at 100 K. In the tensioned limit, to the left of Fig. 2.2, the eigenmodes, labeled by their

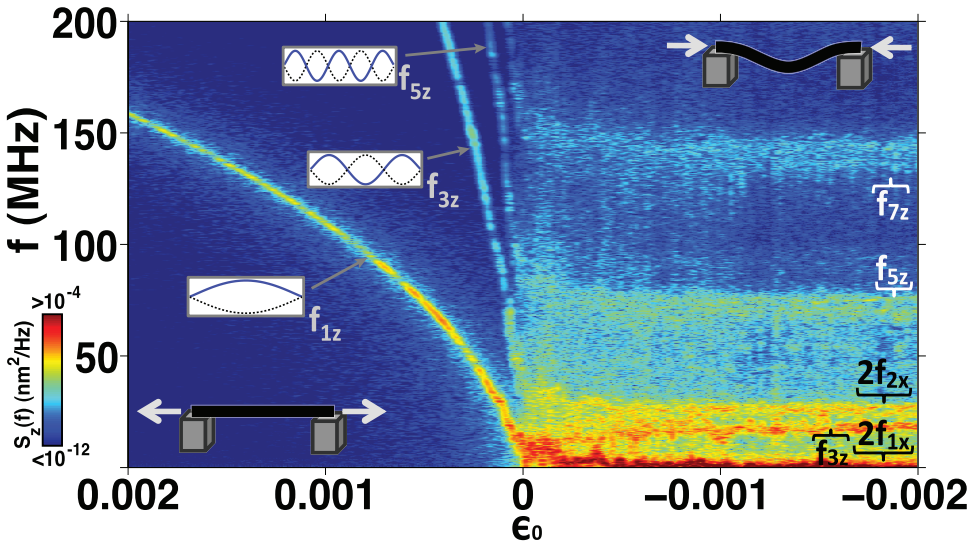

Figure 2.2: Simulated power spectral density of the z-motion of the nanotube as a function of strain ϵ_0 at $T = 100\ K$ with logarithmic colorscale. A small F_z is applied to keep the buckled tube oriented vertically. The tube is taken from tensile strain on the left to compressive strain on the right, as illustrated by the insets. Eigenmode shapes are inset, as are labels for the eigenfrequencies.

modeshape, tune like a tensioned string, giving a frequency: $f_n \approx \frac{n}{2L}\sqrt{\frac{N}{\mu}}$ where $N = K\epsilon$ is the axial tension. Modes without mean z-displacements, including the even in-plane (z-direction) eigenmodes and all out-of-plane (x-direction) eigenmodes, are not visible. Thus, only modes with $n = 1, 3, 5...$ are seen.

With negative strain, the nanotube undergoes a Euler buckling transition, as illustrated in the upper right corner of Fig. 2.2. With the resulting built-in slack, the CNT can bend without stretching leading the spectral lines to no longer tune significantly with strain. The linewidths, however do tune with strain (this can be seen in Fig. 2.6). Also, there are emergent spectral lines corresponding to the motion of out-of-plane modes, as labeled to the right of Fig. 2.2. We analyze these temperature-dependent linewidths in the tensioned case and buckled case separately and discuss the different nonlinear coupling mechanisms [41–43] that apply to each.

2.1 Tensioned Nanotube

We select a fixed tensile zero-temperature clamping condition $\epsilon_0 = 2 \times 10^{-4}$, and simulate the nanotube motion at 6 temperatures, incrementing by 50 K from 50 K to 300 K and plot in Fig.

2.3a the power spectral density over a frequency range spanning up to the $n = 5$ mode. The frequencies of the modes shift linearly with T and, as shown in Fig. 2.3c, the peaks also broaden with $Q^{-1} \sim T$. At 300K, $Q \sim 40$.

Calculation of Q for tensioned NT. The quality factor and frequency shifts can be understood to arise from the change in length of the CNT caused by thermal fluctuation in each eigenmode. The n^{th} eigenmode is given by $u_{na}(y,t) = a_n(t)\xi_{na}(\frac{y}{L})$, where ξ_{na} is the dimensionless modeshape with unit RMS displacement, a_n is a time varying amplitude function, and both the amplitude a and index a refers to either the x or z direction. The tube elongates by the length $\beta_{na}\frac{a_n^2}{2L}$ where $\beta_{na} \equiv \int_0^1 \xi'_{na}(x)^2 dx$ for each independent eigenmode–β_{na} is a dimensionless 1st order perturbation of the path-length integral. Because the tension of the resonator is affected quadratically by the deflection of each resonance mode, the time averaged tension is non-trivially modified by the RMS amplitude of each resonance mode:

$$\langle \epsilon \rangle \approx \epsilon_0 + \sum_{n,a} \beta_{na} \frac{\langle a_n^2 \rangle}{2L^2}. \tag{2.2}$$

where brackets denote a time average over the period of oscillation [44]. Assuming that $\langle a_n \rangle$ obey Boltzmann statistics in thermal equilibrium and that a_n fluctuate incoherently, we are able to solve for the mean strain shift $\overline{\Delta\epsilon}$ and strain variance σ_ϵ^2 as detailed below.

Assuming Maxwell-Boltzmann statistics, we can substitute for the RMS amplitude of the n^{th} mode:

$$\langle a_n^2 \rangle = \frac{k_B T}{k_{na}} \approx \frac{k_B T}{\beta_{na}\frac{K\epsilon}{L} + \alpha_{na}\frac{\kappa}{L^3}} \tag{2.3}$$

where k_{na} is the effective spring constant, and $\alpha_{na} \equiv \int_0^1 \xi''_{na}(x)^2 dx$ parameterizes the bending associated with the n^{th} eigenmode. Combining Eqns. 2.2 and 2.3 yields:

$$\langle \epsilon \rangle \approx \epsilon_0 + \frac{k_B T}{2NL} \sum_{n,a} \frac{1}{1 + \frac{\alpha_{na}}{\beta_{na}}\frac{\kappa}{NL^2}}. \tag{2.4}$$

In the case of a tensioned string, $\beta_{na} \approx n^2\pi^2$ and $\alpha_{na} \approx n^4\pi^4$. Therefore, in the high tension limit, the argument in the series in Eqn. 2.4 is of order unity for small n, which leads to the conclusion that all low n modes contribute equally to the shifts in strain. Consequently, we aim to carry out this sum, and relate it to the total number of fluctuating degrees of freedom that contribute to the tension shift. In the high-tension limit, the series argument is slowly varying, so it can be approximated by an integral:

$$\sum_{n,a} \frac{1}{1+\frac{\alpha_{na}}{\beta_{na}}\frac{\kappa}{NL^2}} \approx 2\int_0^\infty \frac{1}{1+\frac{n^2\pi^2\kappa}{NL^2}}dn \tag{2.5}$$

where the 2 is due to the sum over the a index. Solving the integral yields:

$$2\int_0^\infty \frac{1}{1+\frac{n^2\pi^2\kappa}{NL^2}}dn = \frac{2}{\pi}\sqrt{\frac{NL^2}{\kappa}}\int_0^\infty \frac{1}{1+n'^2}dn' = \sqrt{\frac{NL^2}{\kappa}} \tag{2.6}$$

which we define as n_f, the apparent number of fluctuating degrees of freedom affecting the tension. The main intuition here is that high frequency modes do not appreciably modify the strain, since most of their elastic energy is stored in bending rather than in stretching. With n_f calculated, we have a solution for the strain shift:

$$\overline{\Delta\epsilon} = \langle\epsilon\rangle - \epsilon_0 \approx \frac{k_BT}{2NL}n_f = \frac{L}{2n_f\ell_p}. \tag{2.7}$$

It should be noted that $\overline{\Delta\epsilon}$ is a length-dependent thermal expansion parameter that is distinct from the intrinsic thermal expansion simulated for CNTs [18]. Since n_f is dependent on ϵ, the above equation needs to be solved self-consistently, which can be accomplished by iterative numerical analysis. The negative curvature shown in Fig. 2.3c is a result of this modification of n_f. From Eqn. 2.7, $\overline{\Delta\epsilon}$ leads to $\Delta f \sim T$, which is consistent with the simulated data (fig 2.3b).

Next, we calculate the fluctuations in ϵ in order to determine the expected spectral linewidth for a given mode, and thus determine the expected Q. We start be relating the variance of the

strain to the calculable variance of squared-amplitudes of all resonance modes:

$$\sigma_\epsilon^2 = \sum_{n,a} \left| \frac{\partial \epsilon}{\partial a_n^2} \right|^2 \sigma_{a_n^2}^2 = \sum_{n,a} \frac{\beta_{na}^2}{4L^4} \left(\overline{a_n^4} - \overline{a_n^2}^2 \right). \tag{2.8}$$

Due to Maxwell-Boltzmann statistics, we know the probability distribution for the squared amplitudes of the resonance modes, and thus can calculate and substitute for $\overline{a_n^4}$ and $\overline{a_n^2}$:

$$p\left(a_n^2\right) da_n^2 = \frac{k_{na}}{k_B T} e^{\frac{-k_{na} a_n^2}{k_B T}} da_n^2 \Rightarrow \overline{a_n^2} = \frac{k_B T}{k_{na}}; \overline{a_n^4} = 2\left(\frac{k_B T}{k_{na}}\right)^2. \tag{2.9}$$

As above, we can carry out the series to calculate the strain variance:

$$\sigma_\epsilon^2 = \sum_{n,a} \frac{\beta_{na}^2}{4L^4} \left(\frac{k_B T}{k_{na}}\right)^2 = \left(\frac{k_B T}{2NL}\right)^2 \sum_{n,a} \frac{1}{1 + \left(\frac{\alpha_{na}}{\beta_{na}} \frac{\kappa}{NL^2}\right)^2} \tag{2.10}$$

$$\sum_{n,a} \frac{1}{1 + \left(\frac{\alpha_{na}}{\beta_{na}} \frac{\kappa}{NL^2}\right)^2} \approx$$

$$\frac{2}{\pi} \sqrt{\frac{NL^2}{\kappa}} \int_0^\infty \frac{1}{\left(1 + n'^2\right)^2} dn' = \frac{1}{2} \sqrt{\frac{NL^2}{\kappa}} \tag{2.11}$$

$$\sigma_\epsilon^2 = \frac{1}{8} \left(\frac{k_B T}{NL}\right)^2 \sqrt{\frac{NL^2}{\kappa}} = \frac{L^2}{8 n_f^3 \ell_p^2}. \tag{2.12}$$

The strain fluctuations directly lead to frequency fluctuations, and thus affect the resonance width. We then are able to calculate the expected quality factor:

$$Q^{-1} = \frac{\delta f_{FWHM}}{f} = \sqrt{8 \ln(2)} \frac{\sigma_f}{f} = \sqrt{2 \ln(2)} \frac{\sigma_\epsilon}{\epsilon}. \tag{2.13}$$

The $\sqrt{8 \ln(2)}$ factor relates the variance of a gaussian distribution to its FWHM. Although it is not regularly assumed that a resonance peak will have a gaussian profile, the above theory and Kubo formalism implies this. In this respect, the simulated power spectral density displays mostly

gaussian peaks with Lorentzian tails, as seen in Fig. 2.3. With this we predict for the inverse quality factor for tensioned nanotubes:

$$Q^{-1} = \frac{\sqrt{\ln 2}}{2} \frac{L}{n_f^{\frac{3}{2}} \epsilon \ell_p} \tag{2.14}$$

Eqn. 2.14 is our first key result. The dominant T-dependence comes from $\ell_p^{-1} \sim T$, but both n_f and ϵ have weak T-dependence as a result of entropic stretching. The quantity $n_f^2 \ell_p$ is the persistence length for a tensioned beam and parameterizes how far fluctuations drive the CNT out of equilibrium. The $n_f^{\frac{3}{2}}$ dependence then can be understood to arise from an additional linewidth broadening $\sim n_f^{\frac{1}{2}}$ due to averaging over n_f uncorrelated degrees of freedom. Eqn. 2.14 accurately describes the numerical results, shown in fig. 2.3c, and shows that fluctuation broadening can account for the experimentally observed $Q \sim 100$ at room temperature [3, 40].

2.2 Buckled Nanotube

Next, we study a nanotube under compressive strain, picking $\epsilon_0 = -4 \times 10^{-3}$. Applying a small downward force $F_z = 0.6\ pN$ that mimics the force applied by the gate in experiments, simulations were performed at logarithmically spaced temperatures from 3.1 K to 300 K, as shown in Fig. 2.4. In contrast to the tensioned regime, there is complex structure in the spectra, with many spectral features growing non-linearly with T. Linear theory predicts that f_{3z} and f_{5z} would be the only visible spectral lines in Fig. 2.4. The other emergent modes can be identified as either oscillations of out-of-plane modes producing z-displacement at twice their natural frequency ($2f_{1x}$, $2f_{2x}$, and $2f_{3x}$) and mixes of in-plane modes ($f_{5z} - f_{3z}$ and $f_{5z} + f_{3z}$). Focusing on the lowest observed in-plane mode (f_{3z}), we observe $Q^{-1} \sim T$ (Fig. 2.4 inset) and a decrease in frequency with increasing temperature. From this we extract $Q \sim 5$ for this mode at 300 K.

Further insight is gained by smoothly tuning frequencies by quasi-statically varying the mag-

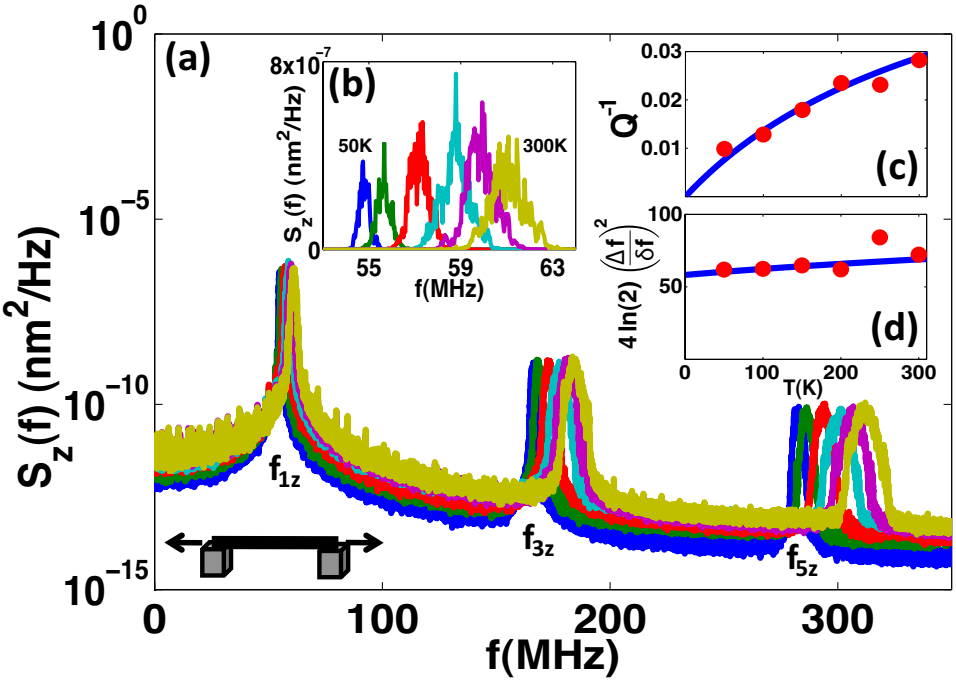

Figure 2.3: a) Power spectral density of a tensioned nanotube with $\epsilon_0 = 2\times10^{-4}$. Six temperatures are plotted from 50-300 K spaced evenly in T. b) is a linear plot of $S_z(f)$ for f_{1z} showing that the frequency shift Δf and linewidth δf both scale linearly with T c) inverse quality factor of f_{1z} vs. temperature. d) dimensionless fixed ratio of Δf to δf that corresponds to n_f, the number of independent fluctuating modes contributing to spectral broadening and frequency shifts. In c) and d) data are circles, and theory is a line. The line in c) corresponds to Eqn. 2.14 and in d) n_f in Eqn. 2.8

nitude of the electrostatic force $F_z = \frac{1}{2}C'V_g^2$, as shown in Fig. 2.5a, where V_g corresponds to the electrostatic voltage applied to the gate illustrated in Fig. 2.1a and $C' = \frac{dC}{dz}$ is the derivative of the tube-gate capacitance assuming a 400 nm gap. The spectral lines tune with force and the frequency-doubled out-of-plane spectral lines cut across the in-plane spectral lines. At 0 K, linear theory predicts there to be no coupling. However, at the intersections, there are observable avoided crossings, even at 10 K as seen in Fig. 2.5a. This behavior is consistent with experiments [4]. To study this, we fix F_z at a crossing indicated by the dotted line in Fig. 2.5a, quasi-statically sweep the temperature, and measure $S_z(f)$ (shown in the inset of Fig. 2.5a). Here, we observe a sub-linear T-dependence of the splitting at the avoided crossing. At 300 K the frequency splitting is nearly $1/5^{th}$ of the resonance frequency, indicating a strong coupling strength induced entirely by thermal fluctuations.

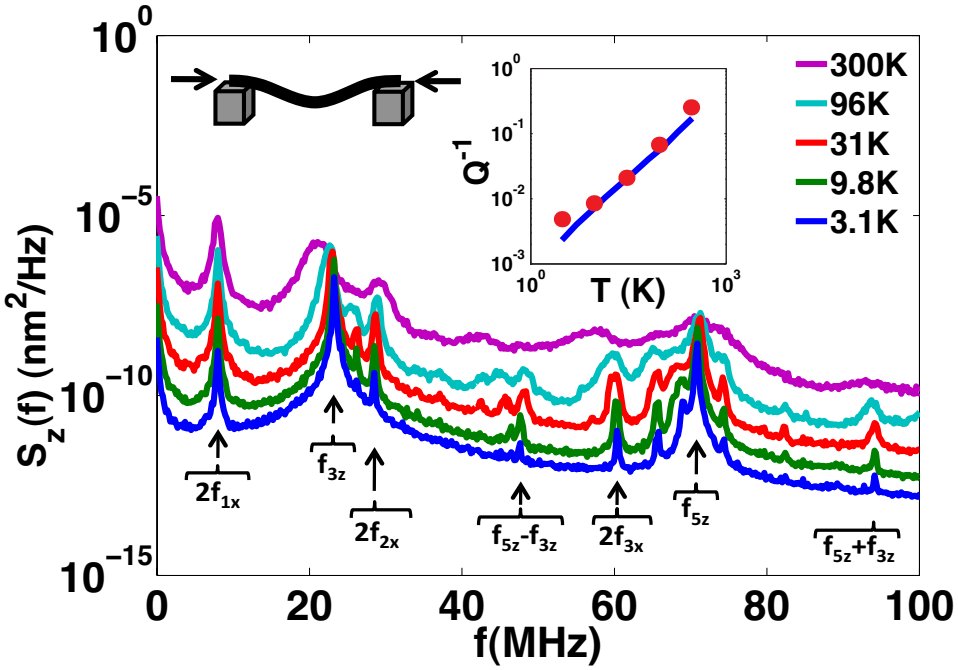

Figure 2.4: Power spectral density of buckled nanotube with $\epsilon_0 = -4 \times 10^{-3}$ with $F_z = 0.6\ pN$ at logarithmically spaced temperatures. The built-in intrinsic damping dominates the apparent linewidth at the lowest temperature. Inset is a plot of Q^{-1} of the f_{3z} mode. Simulation data are shown as red dots, and theoretical predictions from Eqn. 2.29 are plotted as a blue line. Labels beneath each spectral line correspond to their expected origin.

Analytical model. We build an analytical model for this behavior by first modeling the CNT as an inextensible object. In this framework, when an out-of-plane mode has finite amplitude, the CNT must move up in the z-direction to preserve length, as illustrated in Fig 2.5d. To start we make a simplifying assumption, in which we assert that the in-plane deflection is in the shape of the static buckling. The inextensibility tied in with this assumption constrains that the differential length $dL = \sqrt{\beta_{1z}\,|\epsilon|}dz_1 - 2\sum_n \frac{\beta_{1x}x_n}{L}dx_n$ is zero, where $z_1\xi_{1z}(\frac{y}{L})$ is the equilibrium deflection of the tube. ξ_{1z} is a linear combination of in-plane modes, requiring to 2^{nd} order that $z_{nNL} = z_n + \frac{\eta_n}{L}\sum_m \beta_{mx}x_m^2$ where $\eta_n \equiv \frac{\langle\xi_{1z}|\xi_{nz}\rangle}{\langle\xi_{nz}|\xi_{nz}\rangle}\frac{2}{\sqrt{\beta_{1z}|\epsilon|}}$ in which the brackets are an inner product defined by $\langle a(x)|b(x)\rangle = \int_0^1 a(x)b(x)dx$ [44] .

Focusing on a single pair of in- and out-of-plane modes, we can write down the Lagrangian:

$$L = \frac{1}{2}m\dot{z}_{ip}^2 + \frac{1}{2}m\dot{x}_{op}^2 - \frac{1}{2}k_{ip}\left(z_{ip} - \frac{\eta}{L}\beta_{op}x_{op}^2\right)^2 - \frac{1}{2}k_{op}x_{op}^2. \tag{2.15}$$

Solving for the equations of motion, we get:

$$m\ddot{z}_{ip} = -k_{ip}\left(z_{ip} - \frac{\eta}{L}x_{op}^2\right) \tag{2.16}$$

$$m\ddot{x}_{op} = -k_{op}x_{op} - 2k_{ip}\frac{\eta}{L}x_{op}\left(z_{ip} - \frac{\eta}{L}x_{op}^2\right). \tag{2.17}$$

Eqns. 2.16 and 2.17 are nonlinearly coupled equations that we now seek to simplify, as our main goal is to understand how the resonance frequencies shift based on the amplitudes of the relevant modes, as opposed to the detailed phase relationships. Consequently, we will recast the coupling in terms of a mean-field interaction matrix. Since, the coupling is quadratic in x_{op}, we express Eqn. 2.16 in terms of its apparent in-plane deflection:

$$z_{op} \equiv \frac{\eta}{L}\beta_{op}x_{op}^2 \tag{2.18}$$

In order to substitute into Eqn. 2.17 we rewrite Eqn. 2.18 in terms of x_{op} and compute the 2^{nd} derivative respectively:

$$x_{op} = \sqrt{\frac{z_{ip}L}{\eta\beta_{op}}} \tag{2.19}$$

$$\ddot{x}_{op} = -\frac{1}{4}\frac{(\dot{z}_{op})^2}{z_{op}^2} + \frac{1}{2}\frac{\ddot{z}_{op}}{z_{op}}. \tag{2.20}$$

This gives:

$$m\left(2\ddot{z}_{op} - \frac{(\dot{z}_{op})^2}{z_{op}}\right) = -4k_{op}z_{op} + 8k_{ip}\frac{\eta}{L}z_{op}\left(z_{ip} - z_{op}\right). \tag{2.21}$$

The solution to Eqn. 2.21 in the absence of coupling is:

$$z_{op} = \bar{z}\left[\cos\left(2\omega t + \phi\right) + 1\right] \tag{2.22}$$

where $\omega = \sqrt{\frac{k_{op}}{m}}$. In the weak coupling limit, we can assume that z_{op} retains this approximate functional form while the frequency may be perturbed by the interaction term. With this approximation

in mind, we calculate all of the relevant terms seen in Eqn. 2.21:

$$\frac{\left(\dot{z}_{op}\right)^2}{z_{op}} = 4\omega^2\bar{z}\left(1-\cos\left(2\omega t+\phi\right)\right) \tag{2.23}$$

$$\ddot{z}_{op} = -4\omega^2\bar{z}\cos\left(2\omega t+\phi\right) \tag{2.24}$$

The first effect we solve for is due to the term containing z_{op}^2 which originates from the x_{op}^3 term in Eqn. 2.21. Neglecting the $z_{op}z_{ip}$ term, and dropping all oscillating terms we solve for the modified frequency:

$$\omega^2 = \omega_{op}^2 + 3\bar{z}\omega_{ip}^2\frac{\eta\beta_{op}}{L}. \tag{2.25}$$

Next, we solve for the effect due to the $z_{op}z_{ip}$ term. Here we substitute $z_{ip} = \bar{z}_{ip}cos\left(\omega_{ip}+\theta\right)$, and assuming $|2\omega_{op}-\omega_{ip}| \ll |2\omega_{op}+\omega_{ip}|$, we retain only terms close in frequency to $2\omega_{op}$ and get:

$$2\ddot{z}_{op} - \frac{\left(\dot{z}_{op}\right)^2}{z_{op}} = -4\omega_{op}^2 z_{op} + \left[8\omega_{ip}^2\frac{\eta\beta_{op}}{L}\bar{z}_{op}\right]z_{ip} \tag{2.26}$$

Combining the conclusions from Eqns. 2.25 and 2.26, substituting for $\bar{z}_{op} = 2\frac{\eta\beta_{op}}{L}\left\langle x^2\right\rangle$ we rewrite Eqn. 2.16 and Eqn. 2.21 to obtain linearized equations of motion:

$$m\ddot{z}_{ip} = -k_{ip}z_{ip} + k_{ip}z_{op} \tag{2.27}$$

$$\begin{aligned} m\ddot{z}_{op} = &\left[16k_{ip}\left(\frac{\eta\beta_{op}}{L}\right)^2\left\langle x^2\right\rangle\right]z_{ip} - \\ &\left[4k_{op}+24k_{ip}\left(\frac{\eta\beta_{op}}{L}\right)^2\left\langle x^2\right\rangle\right]z_{op} \end{aligned} \tag{2.28}$$

Finally we express the coupled equations in matrix form, symmetrizing the off-diagonal elements by taking the geometric mean, so that the eigenvectors are in the basis of the original, uncoupled solutions. This results in our interaction matrix in the following form:

$$\begin{bmatrix} -k_{ip} & \alpha(T)k_{ip} \\ \alpha(T)k_{ip} & -4k_{op} - \frac{3}{2}\alpha^2(T)k_{ip} \end{bmatrix} \begin{bmatrix} z_{ip} \\ z_{op} \end{bmatrix} = m \begin{bmatrix} \ddot{z}_{ip} \\ \ddot{z}_{op} \end{bmatrix} \tag{2.29}$$

where $\alpha(T) \equiv \frac{4\eta\beta_{op}\sqrt{\langle x_{op}^2 \rangle}}{L}$ and $\langle x_{op}^2 \rangle$ is time-averaged over the period of oscillation.

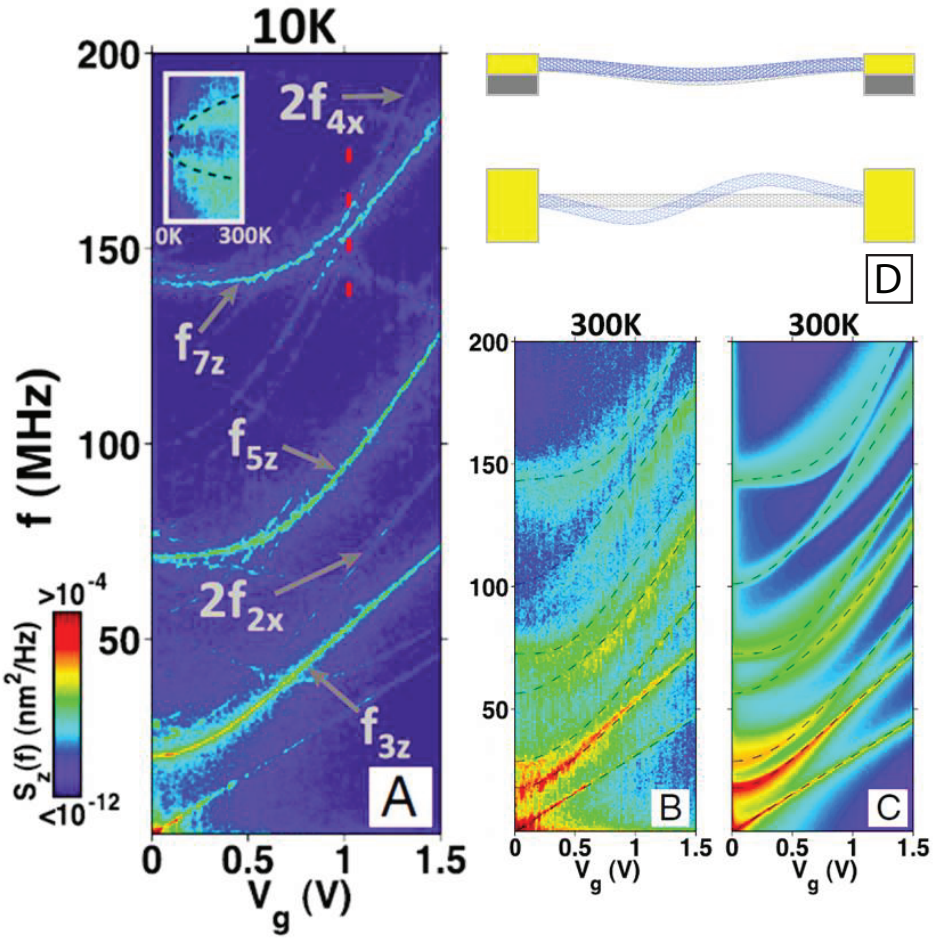

Figure 2.5: a) color-map of power spectral density at 10 K of the mean z-displacement of a buckled nanotube resonator as a function of gate voltage assuming tube is 400nm above the gate. Modes are labeled as defined in Fig. 2.3 and colorscale is identical to that in Fig. 2.2. T-dependence from 0 K to 300 K of the apparent avoided-crossing at 150 MHz is shown in the inset at a fixed V_g indicated by the red dotted line b) 300 K data of same force sweep in a). c) plots the theoretical power spectral density, based on the generalized version of Eqn. 2.29 described in the text, for the same conditions as in b). The dashed lines in b) and c) correspond to the theoretical central frequencies from the generalized version of Eqn. 2.29.

Using $\langle x_{op}^2 \rangle = \frac{k_B T}{k_{op}}$ gives $\alpha(T) \sim \sqrt{T}$, which when substituted into Eqn. 2.29 predicts average frequency shifts. At an avoided crossing, $k_{ip} \approx 4k_{op}$ gives the prediction that $\Delta f \approx \frac{1}{2}\alpha(T)f_{ip}$. This

matches the simulated T-dependence, as shown by the theoretical prediction that is overlaid on top of the data in the inset of Fig. 2.5a.

By extending Eqn. 2.29 to the full interaction matrix, populating each mode according to Boltzmann statistics, and weighting the resulting frequency probability distribution by the squared-amplitude distribution we are able to generate a theoretical $S_z(f)$ map, which is shown in Fig. 2.5c. It compares well with the simulated results at 300 K shown in Fig. 2.5b. In addition, the linewidths in the theoretical $S_z(f)$ give an accurate prediction of the simulated Qs, as shown in the inset of Fig. 2.4. The specific degree of coupling is geometry dependent, and thus not fully analytically generalizable, but Eqn. 2.29 predicts for the lowest in-plane mode f_{3z} that:

$$Q^{-1} \approx 0.04 \frac{L}{|\epsilon| \ell_p}. \tag{2.30}$$

Eqn. 2.30 (derivation shown in the next section) explains the strain dependence of the spectral fluctuations seen in the right half of Fig. 2.2: Q improves with increased buckling as the geometric coupling between modes decreases. Furthermore, due to its coupling with higher frequency modes, the lowest in-plane mode is predicted to decrease frequency with increasing temperature at low V_g, which is frequently observed in experiment [4, 9].

Calculation of Q for buckled NT. Solving for the quality factor of the buckled NT follows an analogous procedure to that in the tensioned NT, where Q is obtained by averaging over a statistical distribution of frequencies. Eqn. 2.29 can be solved for eigenfrequencies that are dependent on the amplitude of the out-of-plane mode:

$$\omega_{\pm}^2 = \frac{\omega_{ip}^2 \left(1+4\alpha^2(T)\right)+4\omega_{op}^2}{2} \pm \tag{2.31}$$

$$\frac{\left|\omega_{ip}^2 \left(1-4\alpha^2(T)\right)-4\omega_{op}^2\right|}{2} \sqrt{1+\frac{\alpha^2(T)\,\omega_{ip}^4}{\left(\omega_{ip}^2\,(1-4\alpha^2(T))-4\omega_{op}^2\right)^2}} \tag{2.32}$$

In the weak coupling limit, the lower eigenfrequency in Eqn. 2.31 (which corresponds to dominant

the in-plane motion) reduces to:

$$\omega_- \approx \omega_{ip}\left(1-\frac{\alpha^2(T)}{8}\frac{1}{\left(\frac{2\omega_{op}}{\omega_{ip}}\right)^2-1}\right). \tag{2.33}$$

In the low-tension limit, the ratio of the lowest in-plane and out-of-plane flexural modes for a Euler-buckled beam is a fixed value giving:

$$\frac{1}{\left(\frac{2\omega_{op}}{\omega_{ip}}\right)^2-1}=2.4. \tag{2.34}$$

Finally, $\alpha^2(T)\propto\langle x_{op}^2\rangle$, so we can solve for:

$$\sigma_f=\left|\frac{\partial f}{\partial x_{op}^2}\right|\sigma_{x_{op}^2} \tag{2.35}$$

$$\sigma_f=\frac{1}{2\pi}\left|\frac{\partial\omega_-}{\partial x_{op}^2}\right|\sigma_{x_{op}^2}=\frac{\omega_{ip}}{2\pi}0.3\frac{64\pi^4\eta^2}{L^2}\frac{L^3k_BT}{16\pi^4\kappa} \tag{2.36}$$

$$\frac{\sigma_f}{f}=1.2\eta^2\frac{L}{\ell_p} \tag{2.37}$$

Carrying out the appropriate inner products gives $\eta^2=\frac{0.05}{|\epsilon|}$ which when substituted into the above equation gives:

$$\frac{\sigma_f}{f}=0.06\frac{L}{|\epsilon|\,\ell_p} \tag{2.38}$$

Here, the relationship between the variance and FWHM of the distribution is not set by a gaussian distribution. The line-shape is notably skewed, and according to the simplified approach outlined above, the lineshape is represented by an exponential probability function. This gives $0.69\sigma_f\approx\delta f_{FWHM}$, which in turn gives Eqn. 2.37.

Quality factor vs. strain. Having made explicit predictions for Q in both the tensioned and bucked cases, we revisit the qualitative observations made in Fig. 2.2 and test them quantitatively.

As demonstrated above, Q of a CNT resonator changes with ϵ_0 since it influences the coupling between resonance modes, both by modifying thermal amplitudes and by changing equilibrium geometry. Under tension, the resonance widths narrow with increasing tension, since all modes decrease their thermal amplitudes and thus tend to couple less strongly amongst one another. In addition to this effect, the bare frequencies increase as $\sim \epsilon_0^{\frac{1}{2}}$ leading to an additional increase in Q with ϵ_0. Eqn. 2.14 accounts for these two effects and when expressed with the full dependence on ϵ we see:

$$Q \sim \epsilon^{\frac{7}{4}}. \tag{2.39}$$

Solving for Eqn. 2.14 at $100K$ over a range of positive strain gives the blue line shown Fig. 2.5a

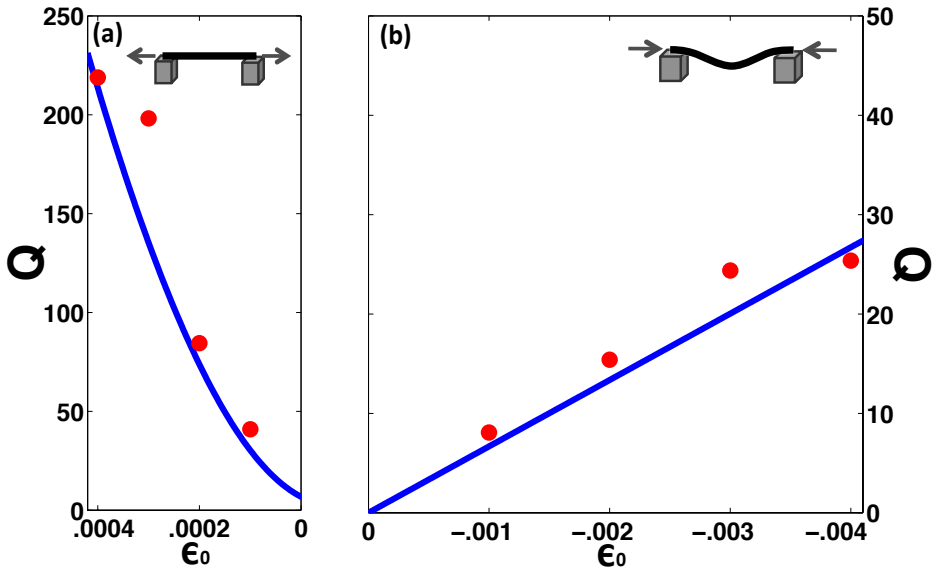

Figure 2.6: Q vs. ϵ_0 at 100K. Eqn. 2 and Eqn. 4 are shown as blue lines in a) and b) respectively. Corresponding simulation results are shown as Red circles.

which is plotted along with simulation results.

Under compression, the bare frequencies of most modes do not vary significantly with strain, however the coupling between resonance modes goes inversely with $|\epsilon|$. Eqn. 30, computed over a range of negative strain, gives the blue line in Fig. 2.5b which is similarly plotted along with simulation results.

2.3 Discussion

These results show that fluctuation broadening dominates the behavior of CNT resonators over a broad range of temperatures, and appears to be the main cause of temperature-dependent quality factors measured in both tensioned and untensioned resonators. Understanding the mechanism behind fluctuational broadening in CNT resonators draws on the ideas of polymer physics and underscores how thermal fluctuations can strongly modify the vibrational spectrum and decay widths in reduced dimensional nanoscale objects. To date there is limited experimental data characterizing Q over a broad temperature range in CNT resonators, but thus far, data remain at or below our theoretical upper bound [3, 4, 45]. We predict a specific dependence of Q on ϵ_0 and T which can be tested by experiments that vary these parameters independently on individual CNT resonators. Specifically, varying ϵ_0 at a fixed T will be the most informative for this work, as the interpretation will be less obscured by systematic strain shifts that occur due to thermal expansion of the system.

This work implies a fundamental limit on Q in high aspect ratio resonators at finite temperatures. Tailoring the geometry of these systems is necessary to mitigate thermally-induced mode-coupling and thus improve Q.

Chapter 3

Fabrication of CNT microtweezers

The results presented in Chapter 2 propose detailed properties of CNT resonance behavior, which may indeed explain the underlying mechanism of experimental observations made thus far, but a more basic point it advances is that the boundary conditions (e.g. strain) can entirely alter the mode-coupling dynamics. From an experimental stand-point, this implies that either precise measurement of, or control over the boundary conditions may be crucial to understanding their resonator dynamics, yet this proves quite challenging for CNT resonators created using traditional fabrication techniques. Specifically, on-chip fabrication necessitates fixed boundary conditions, and CNT growth methods produce inconsistent tension or slack.

Research that circumvents the limiations of on-chip fabrication of CNT mechanical devices has substantial historical precedence. Because CNTs are not readily seen optically, piezo-driven nanomanipulators have been used to push, bend, and pull on CNTs inside scanning electron microscopes (SEMs) and transmission electron microscopes (TEMs) in order to study their mechanical properties as well as to produce novel technologies (e.g. nanotube-tipped AFM). This approach has yielded varying degrees of success, but the complexity of such an apparatus combined with the harsh electron environment in SEMs and TEMs limits their suitability in performing sensitive, time-intensive measurements.

Using micro manipulation in order to characterize CNT mechanical resonances in an attractive approach as it enables dynamical control of the boundary conditions. Indeed, preliminary

work operating in SEMs has been able to tune CNT resonances by applying strain [46], but the aforementioned challenges limits the scope of these investigations. Therefore, developing a new, versatile manipulation system that can operate without the aid of electron microscopy seems crucial in advancing our understanding of CNT entropic thermal physics.

Motivated by this and other scientific goals, we designed a micro-tweezer appatratus that centered around picking up a CNT off a growth substrate, measuring the CNTs properties both electrically and optically, controlling the CNTs proximity to external physical systems, and mechanically applying strain to the CNT, all while avoiding the need to image the CNT. Our approach was to construct an electrically-contacted dual-cantilever system that can change the separation of the cantilevers, much like a pair of tweezers. With a CNT spanning the gap between the tweezers (fig 3.1a), we create a closed electrical circuit and detect the CNTs presence and electrical properties.

In order to open and close our microtweezer system, we use a flexural actuation method, that is analogous to the technique used in forming mechanical breakjunctions. As shown in fig. 3.1b, the tweezers and the electrode tabs are connected to a flexible base. By supporting the edges and depressing the center, the separation can be precisely controlled. Historically, microtweezers have been fabricated using thermomechanical actuators, however, that is not suitable for our system, both due to the relative imprecision of thermomechanical actuation, and the undesirable heat-loading in low-temperature applications.

Finally, in order to manipulate and detect the CNT system, the tweezers are mounted at a downward angle and the spanning CNT is maneuvered near an electrical gate. This geometry is electrically analogous to that used in on-chip CNT resonator studies, and enables us to electrically sense the CNT motion.

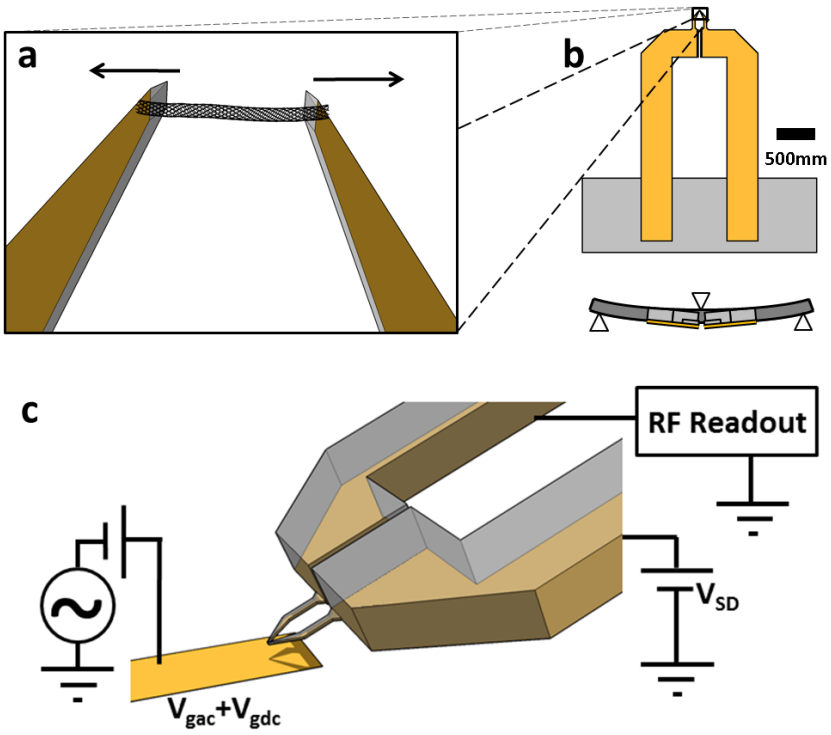

Figure 3.1: Tweezer concept for manipulating and straining electrically contacted CNT a) CNT is to span two electrically-contacted electrodes whose separation can be controlled b) Tweezer design with two electrode tabs connecting to tweezer cantilevers. The tweezers can be opened and closed by flexing the base (schematically shown in a front-view projection.) c) The tweezers are then maneuvered in the vicinity of 3rd electrode on a different substrate with the tweezers tilted downward to allow the tube to interact in close proximity. RF electronics are used to drive and detect the CNT resonator motion.

3.1 Tweezer Microfabrication

Our design approach involves microfabricating tweezers as a passive, consumable part of the overall apparatus so that we can rapidly test multiple CNT devices over a short experimental timescale. As discussed in the previous section, our tweezer operation requires two independent, electrically-contacted cantilevers held together on a flexible base. We chose to use gold as our electrode material and a photopolymer called SU-8 as the flexible cantilever support system. Gold is an attractive electrode material because it is malleable, and thus less prone to fracture, as well as because it is known to make good electrical contact with CNTs. SU-8 is chosen because it is easy to bend as compared to oxides, nitrides, or metals, and is ideal for thick-film patterning.

The fabrication method we developed borrowed techniques from SU-8 MEMS literature [47,48]. The three primary challenges to overcome in the fabrication protocol are 1) maintaining sufficient adhesion between SU-8 and gold, 2) patterning SU-8 with low-stress and high aspect-ratios, and 3) releasing tweezers from their underlying substrate while maintaining mechanical integrity.

Our first successful fabrication protocol works as follows. After electron-beam evaporation of chromium and gold (Cr/Au) onto a carrier wafer, the base of the tweezer electrodes are patterned with a positive-tone photoresist, and the gold is removed using wet-etching, resulting in a pattern shown in fig. 3.2b. After this, an adhesion promotor, 3-mercaptopropyl trimethoxysilane (MPTS) is used prior to spinning and patterning of $15\mu m$ thick SU-8 cantilevers using contact lithography (fig 3.2c). The cantilevers are Pre-baked and post-exposure baked (PEB) at $50°C$ to prevent excessive cross-linking and thus avoiding fusing the tweezers at the tips. Following an O_2 plasma clean, the gold layer is removed using an Argon ion-mill (fig 3.2d), which self-alligns the electrodes to the cantilevers. Next, a $140\mu m$ thick SU-8 frame is patterned overlaying the entire tweezer structure, with the exception of the cantilevers (fig 3.2e). Here, the Pre-bake and PEB were performed at $40°C$. Finally, the tweezers are released in Cr-etchant, transferred to DI and allowed to air dry, resulting in successful cantilevers (fig 3.2f).

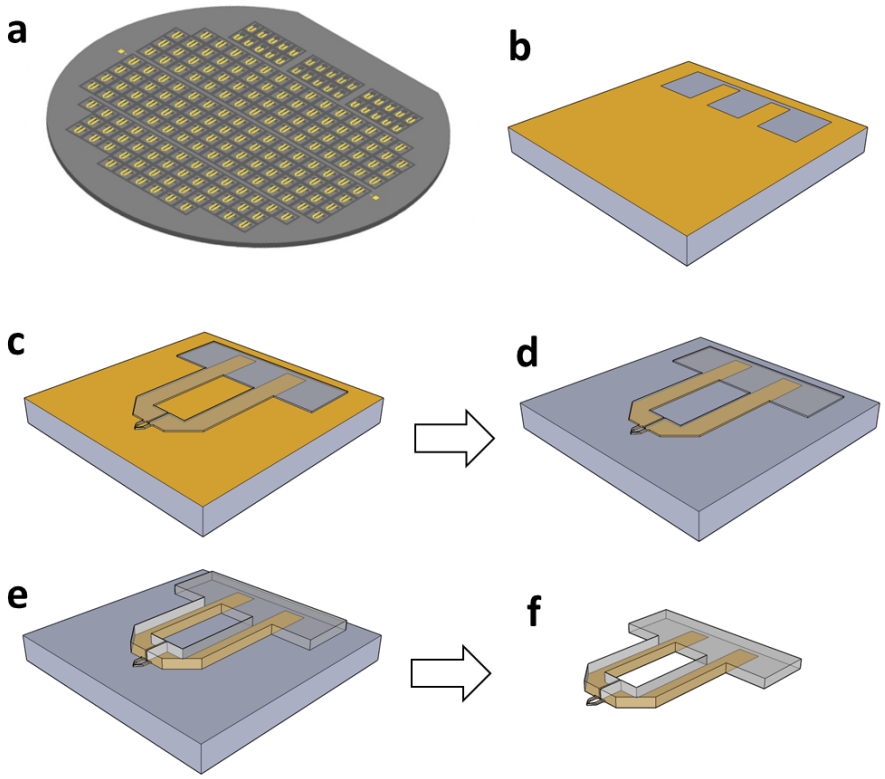

Figure 3.2: a) Batch fabrication of tweezers on top of a carrier wafer. b) After Cr/Au deposition, the base of tweezer cantilevers are definied. c) Cantilevers are patterned out of $15\mu m$ thick SU-8. d) Electrodes are then fully defined using etching or ion-milling. e) $140\mu m$ frame is patterned out of SU-8 for rigidity. f) Tweezers are released from carrier wafer in Cr etchant

This fabrication protocol was successful, and indeed tweezers built using it were used in many of our first experiments, but it posed two notable challenges. First, due to the high-aspect ratio of the cantilever tips, the bake temperature and exposure dose needed to be minimized, and in doing so, the SU-8/Au adhesion is frequently compromised. Second, because there is only $\sim 200nm$ gold on the cantilevers, the gold film was easily damaged and/or scraped off at the tips.

Both of these challenges are solved using a second fabrication protocol, shown in fig. 3.3. Rather than defining the cantilevers out of SU-8 with a thin gold layer beneath, the cantilevers are fabricated directly out of $5\mu m$ thick electroplated gold (fig 3.3a). A thick-film of SU-8 is then patterned as the frame in fig. 3.3b, which is analogous to fig 3.2e; from this point forward the protocol is identical. The resulting gold cantilevers are not able to elastically deform as much as SU-8 cantilevers, however, the gold is thin enough to be flexible. In some cases the ability to

plastically deform gold helps with fine-tuning the cantilevers alignment *in situ*.

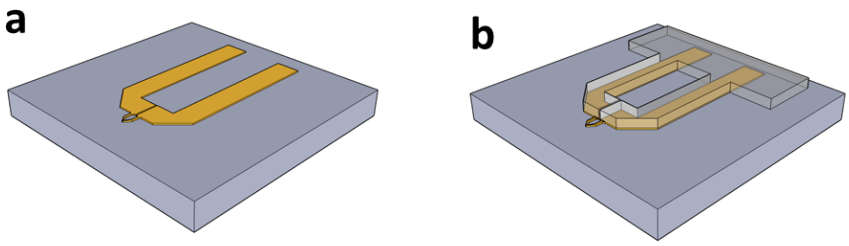

Figure 3.3: Simplified fabrication with electroplated cantilevers. a) After a Cr/Au seed-layer deposition, tweezers and electrodes are formed out of 3-5μm electroplated gold. The gold seed layer is etched away and b) the thick SU-8 frame is patterned as in fig. 3.2e.

3.2 Tweezer actuation system

3.2.1 Tweezer holder

As outlined in fig. 3.1b, actuating the tweezers requires supporting the edges of the tweezer base while pressing down in the middle. In order to accomplish this, we use a commercial four-layer, metal-reinforced piezo flexural actuator with $\pm 250\mu m$ free travel in order to smoothly apply strain over a broad range.

The design concept for the tweezer actuator is relatively straightforward, however, numerous size constraints need to be factored in to constructing the final structure. In particular, the holder needs to: 1) accomodate a lengthy actuator, which is necessary for its large range of motion, 2) be low profile enough to fit above a substrate and beneath a microscope element, and 3) hold the tweezers at a downward angle such that the tweezer tips are the lowest part of the apparatus. In the most confined configuration, based on the cryostat we operated in, the tweezers and their holder needed to fit $23mm$ deep into a $10mm$ gap with $1mm$ clearance.

In order to fulfill these criteria, the holder was designed to fit into the space of a $5.5mm$ wide, $4mm$ tall, and $45mm$ long box held at a 10.3° angle downward from horizontal. The completed

assembly is shown in fig. 3.4a. The assembly is constructed out of a holder body, tweezer clamp plate, actuator clamp, pushrod, and a commercial flexural actuator (fig 3.4b). The tweezer clamp plate is machined out of thin stainless steel sheetmetal and fits into a reccession such that when installed, it is flush with the holder body. The plate needs to be thin so that the tweezers are held very near to the bottom of the holder, yet rigid so that it serves as a stiff fulcrum. The front of both the holder body and the clamp plate were, in fact, tapered in order to increase the clearance (theoretical maximum of $450\mu m$). Although, not illustrated, the plate also serves to immobilize wire leads that make electrical contact to the tweezers electrode tabs. Flexion of the tweezer base is driven by a copper push-rod that passes through a hole bored in the holder body. The pushrod is aligned such that it makes contact at the center of the tweezer base. In order to drive the pushrod, the flexural actuator is rigidly mounted near the rear of the holder body with a gap to allow the front of the actuator to move freely. The actuator is held to the holder body by the actuator clamp, which is made out of a steel band that is tensioned by set-screws that push against the holder body.

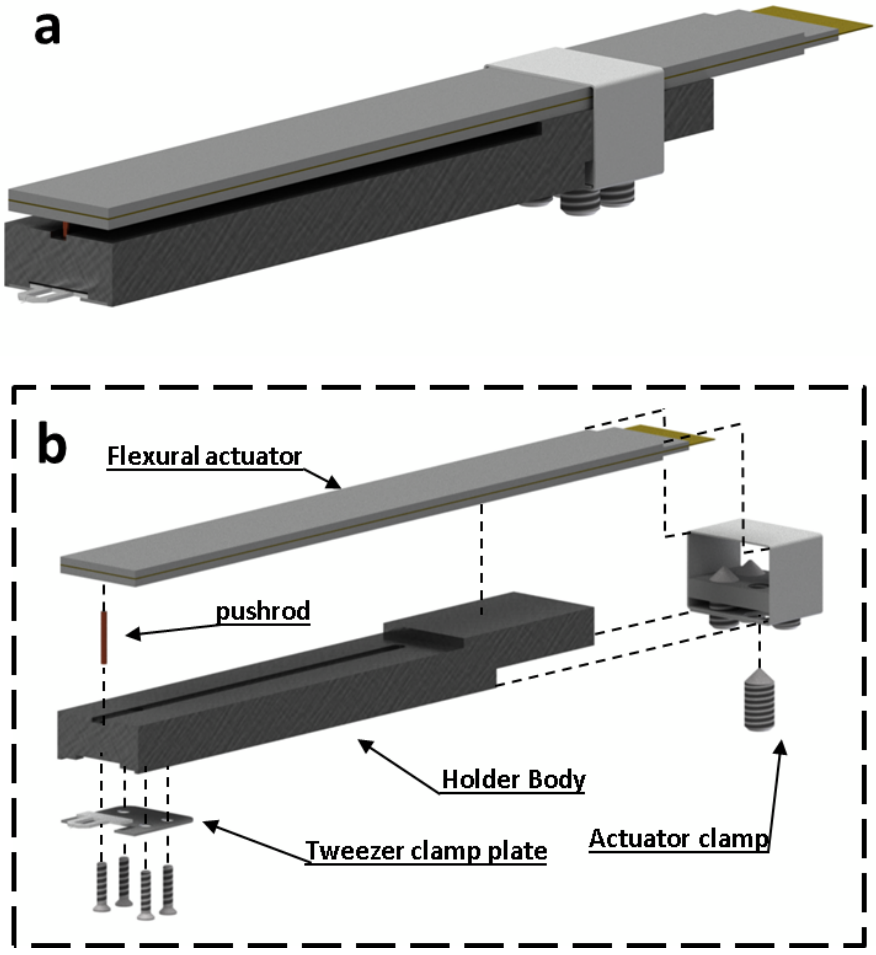

Figure 3.4: a) assembled tweezer holder and actuator. The design is focused on maintaining a low profile for operation in tight spaces. b) exploded diagram of the tweezer holder assembly. The tweezer clamp plate serves as the side fulcrums for bending the tweezers, while the flexural actuator applies force to the center of the tweezer frame with a pushrod. The actuator is fixed to the holder body with a sheet-metal clamp, which uses set screws to pull downward on the actuator

3.2.2 Tweezer actuator assembly

The final main active component of the tweezer actuation system, is a 3-axis piezo stage that enables scanning of the tweezers near a substrate of interest. For this stage, we use a commercially available, miniTRITOR stage provided by the Piezosystem Jena company, which is capable of operating in vacuum and cryogenic environments and has $38\mu m$ of travel for all axes.

The piezo stage needs to be rigidly mounted to a support post and the scanning surface needs to hold the tweezer holder at the 10.3° angle without exceeding the $10mm$ gap requirement. The

completed and assembled design is shown fig. 3.5a. As can be seen in the exploded diagram (fig 3.5b), the tweezer holder (1) is fastened to scanning arm (2) with machine screws into two tapped holes in the holder. The scanning arm is offset so that the tweezers are centered in front of the support post. These main components are attached to the scanning stage with two attachment plates, which are necessary to rigidly fasten elements with the given screw-hole positions in the piezo stage. As can be seen in fig 3.5b, the fastening of the scanning arm (2) to its associated attachment plate appears redundant, however, the scanning arm was designed to attach to different scanning stages to be described below. This is also why only three fasteners are used to mount the scanning arm, as the alignment of the fourth hole conflicts with the fastener below.

The geometry diagrammed in fig. 3.5 is used in our resonance measurements, and is tailored to meet specifications of the cryostat, described in the next section. As the technique is not confined to operating only in vacuum environments, we constructed two additional manifestations which will be noted in the next chapter.

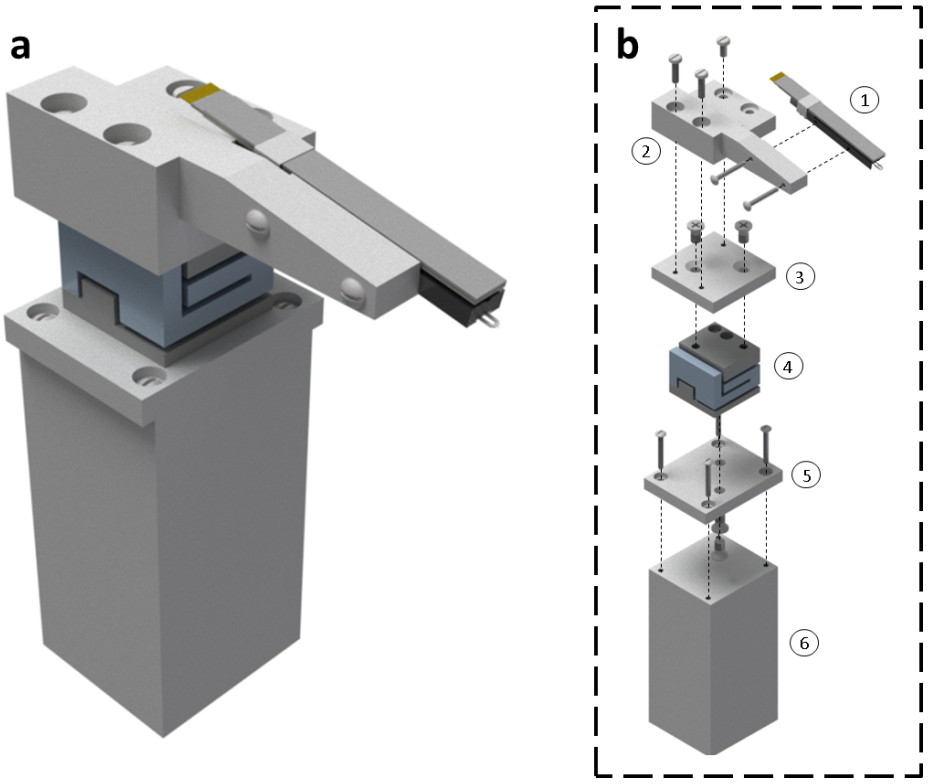

Figure 3.5: a) Tweezer actuator assembly with 3-axis piezo cube. The tweezer holder is held with a 10.3° down slope to satisfy a clearance criterion of re-entrant windows used in our cryostat. b) exploded view of tweezer actuator assembly. The tweezer holder (1) (shown in fig. 3.4) is attached to a scanning arm (2), mounted to a 3-axis pizeo scanner (4) which is attached to a rigid post (6). Between these main components are connector plates (3) and (5) which satisfy the constraints set by the screw placement on the actuator and the post geometry. (2) and (3) could be combined in this architecture, but (2) is designed with screw placements to enable attachment to another piezo stage

3.3 Cryostat for CNT Micromanipulation

Motivated in part by our interest in measuring the thermal physics of CNT resonators, we designed a custom-built electro-optomechanical probe station built around a Janis cryostat framework, which was funded as a capital project by the Kavli Institute at Cornell for Nanoscience. As photographed in fig. 3.6a, the probe station is a table-top flowthrough cryostat with one traditional RF probe arm. Distinguishing the Kavli cryostat from a standard cryogenic probestation, there are two fiber optic feedthroughs visible from the front of the cryostat in fib 6a, two RF feedthroughs (not visible in the image) and a reentrant window for relatively high NA (0.42) long-working distance optics.

Inside the cryostat, we have two independent 3-axis attocube stages, (fib 6b (3) and (4)), a coaxial RF probe (2) with mounting for a GSG probe, and the home-built tweezer actuator assembly (1). Unlike the piezo stage in the tweezer actuator assembly, the attocube stages operate on a stick/slip inertial principle and thus have up to $1cm$ of range. Over the course of a measurement, the main attocube stage (3) is used to coarsely bring a substrate of interest into the vicinity of the tweezers, and the miniTRITOR stage is used to finely scan the tweezers position. In some measurements a third structure is brought into the system with the auxiliary attocube stage (4) for example, we used tapered fibers to couple into optical cavities, which is discussed further in Chapter 6.

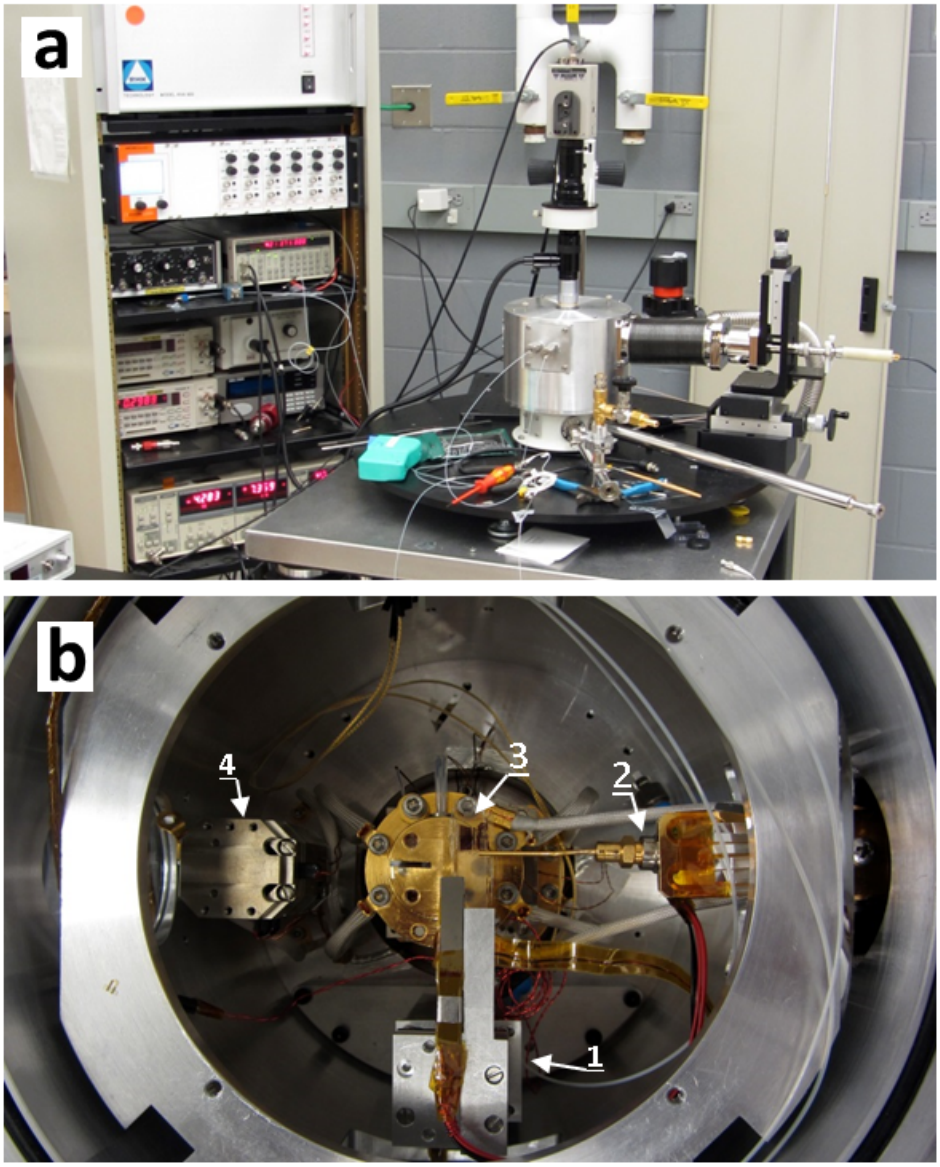

Figure 3.6: a) Kavli cryostat is a custom fitted Janis flowthrough He-cryostat, with fiber optic feedthroughs, RF feedthroughs, and a reentrant window for high NA optics. There is one manually controlled RF probe arm visible to the right while all other controls are internal piezo stages seen in b). b) is a top view of the cryostat with the top-plate removed. 1) is the tweezer actuator assembly. 2) is the RF probe arm. 3) is a scnnable attocube stage, and 4) is a secondary scannable attocube stage on which a tapered optical fiber holder can be installed (discussed in Ch. 6)

3.4 Nanotube source substrate

Having established how micro-tweezers are fabricated, and how they are both maneuvered and actuated inside of a cryostat, we next need a means of attaching CNTs across the tweezer electrodes.

Illani *et. al.* pioneered a four-electrode method in which suspended tubes on a growth substrate are contacted and then cut using joule heating by electrically biasing the exterior electrodes. Our approach, instead, involves effectively peeling CNTs off a low adhesion energy corrugated substrate, illustrated in the fig. 3.7 inset.

Motivated, in part, by being able to use our system on an inverted microscope, our CNT source substrate was fabricated out of a $170\mu m$ fused-silica wafer. In order to form the corrugated surface, periodic arrays were lithographically patterned onto the silica substrate using chromium as a hard mask which was patterned in a stepper machine. The corrugations were then formed through a CHF_3 Reactive ion etching (RIE) process. Serendipitously, by failing to use sufficient O_2 plasma cleaning in the etching process [49], the etched surface was substantially roughened as is evident in fig. 3.7. This additional roughness serves to reduce the contact area of the CNTs to the underlying substrate, thus ensuring that the CNTs will be easy to peel up. Next, a 2Åthick iron layer is electron-beam evaporated onto the roughened substrate; this will serve as the CNT growth catalyst. Finally, CNTs are grown on the source substrate using a standard Ethanol-based growth method [50]: 300sccm of Ar bubbled through Ethanol, 250 sccm of Ar, and 100 sccm of H_2 at a growth temperature of $925°C$. The flow conditions are such that CNTs grown by this method are flow aligned.

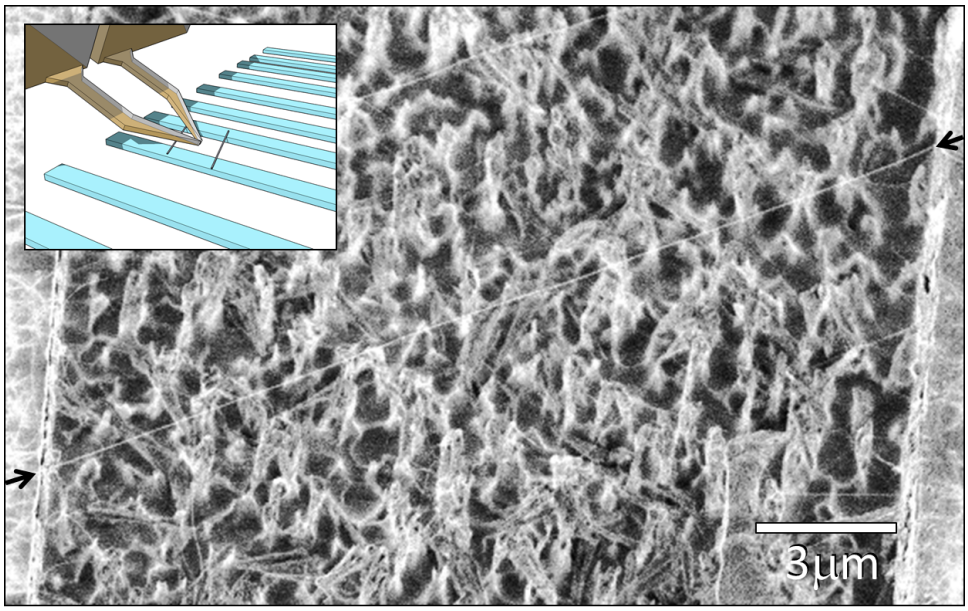

Figure 3.7: Nanotube source substrate for picking up CNTs. Inset: schematic of tweezers over CNT source substrate. CNT source substrate is fabricated out of RIE etched fused-silica with a roughened pattern to reduce surface contact. A thin layer of Fe is evaporated on and a standard ethanol flow aligned growth is used to produce small-diameter few-walled CNTs

3.5 Protocol for picking up and measuring CNT

With CNTs successfully grown on the source substrate, we can now use our tweezer system to pick-up and visualize a CNT. As stated in the introduction, this method uses conductance feedback to infer if successful contact is made to the CNT, thus alleviating the need to directly see the tube in the process.

The CNT source substrate is mounted onto the primary attocube stage and brought into the vicinity of the tweezers, as illustrated by fig. 3.8a. Figure 3.8a also schematically represents the relative orientation of the CNTs grown on the substrate. Via a LabView computer interface, the user then applies a voltage to one tweezer electrode and monitors the current through a preamplifier on the other electrode. Then, as seen in fig 3.8d, the tweezers are moved to the right, relative to the source substrate. As the tweezers moves, intermittent contact is frequently made to a tube, yielding a short pulse of measured current. The user continues scanning the tweezers near the surface until robust contact is made to a tube. At this point, the source substrate is lowered away (fig. 3.8b)

while the CNT remains intact. Given that the tube was not directly imaged in the process, there is uncertainty at this point as to the location of the CNT, and even if only one tube was picked up. This is easily resolved by simply increasing the bias and optically observe the CNT luminesce in vacuum. Visualizing the tube will be important for measuring the length and orientation of the particular CNT being measured.

In this chapter, we have demonstrated a versatile means of making electrical contact to a free-standing, optically accessible CNT with a home-built micro-tweezer system that can move the CNT in 3-dimensions as well as apply strain to it. Using current feedback, this method overcomes the challenges presented by micromanipulation in SEMs, and thus paves the way for diverse applications and measurements of CNTs. Our main body of work focuses on studying suspended, vibrating CNTs, however, in the next chapter we will survey the variety of measurements and potential applications that we explored.

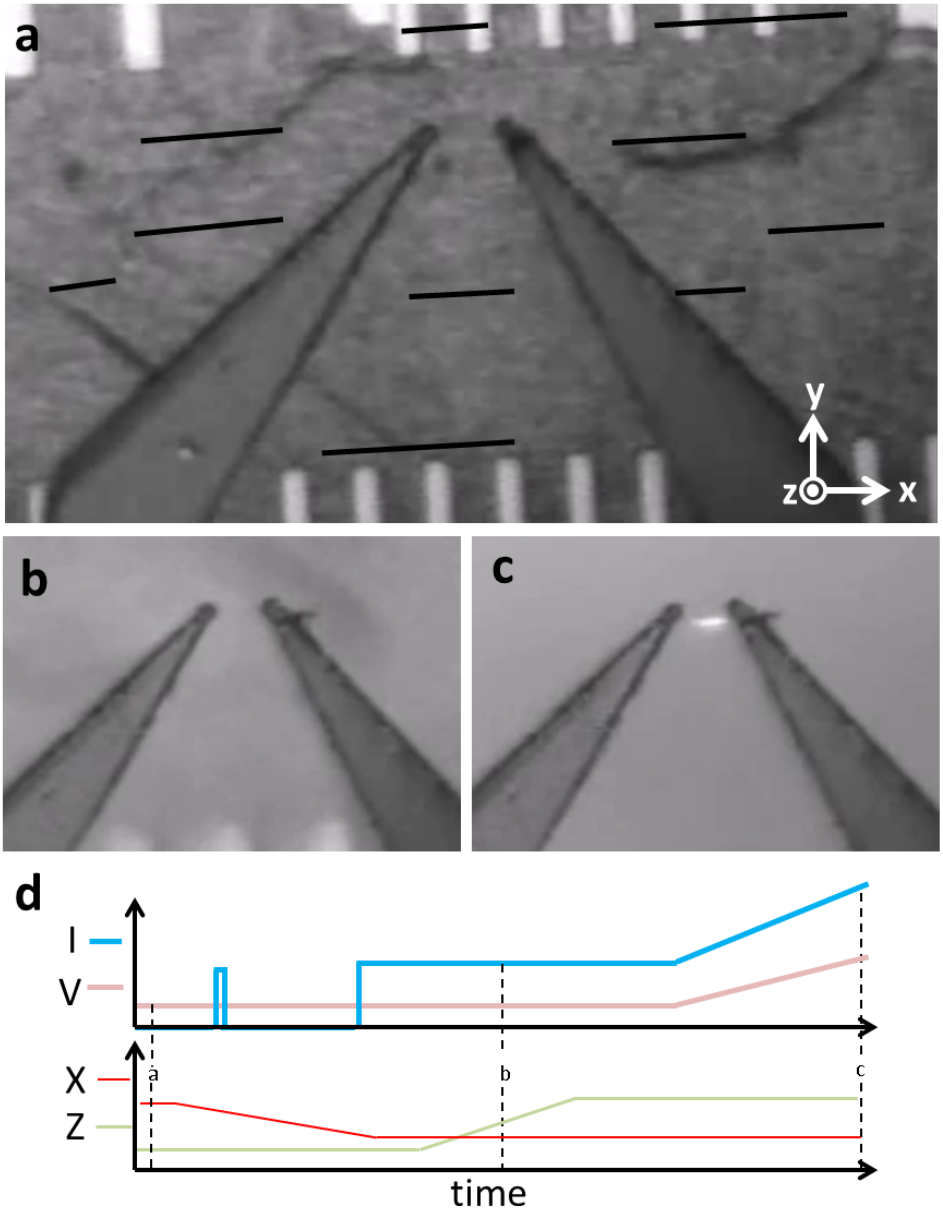

Figure 3.8: Picking up CNTs with electrical feedback. a)tweezers are positioned in close proximity to CNT source substrate. Orientation of CNTs is schematically drawn with black lines. With a bias across the tweezers, they are moved in the x-direction, in this instance to the left as indicated in d) The tweezers are moved until continuous contact is made, and lifted up as seen in b). c) Turning up the bias causes luminescence, providing a means of directly visualizing the CNT position. d) are schematic time traces of three control parameters Voltage, V; x-position, X; and z-position, Z as well as the response, current, I. dotted lines indicate where (a),(b), and (c) fall in the time-series

Chapter 4

Applications of CNT microtweezers: Optics, Electronics, Mechanics, and Bioprobes

As discussed in Chapter 3, we developed the tweezer apparatus in order to access important degrees of freedom in studying CNT resonance behavior. The tools and techniques developed in that pursuit, in fact, opens doors to diverse applications beyond this singular goal. In this chapter we survey the breadth of possible avenues our approach enables, demonstrating novel ways to image, manipulate, and utilize the CNT-tweezer system. The simplicity and portability of the tweezer apparatus makes it easily transferable and thus we are not limited to operating in a vacuum cryostat.

4.1 Tweezer actuator designs

In total, we constructed three nanotube actuator systems. The first, described in Chapter 3 is devoted to use in a vacuum cryostat. The next, shown in fig. 4.1, is a vacuum compatible, compact tweezer system meant for use in either cryogenic probe-stations, or on any bench-top apparatus. The final, shown in fig. 4.2, is an inverted microscope-mounted system for opto-electromechanical measurements in air or in liquid. All of these architectures similarly rely on electronic detection of CNTs, therefore they only require rudimentary optical imaging to successfully pick-up and

manipulate CNTs.

4.1.1 Compact tweezer scanner

Predating our construction of a devoted cryostat system, we designed and built a versatile, portable CNT tweezer scanner capable of being installed in an unmodified cryogenic probestation. This design utilizes the tweezer holder and xyz piezo cube used in the cyrostat-mounted system (described in Chapter 3). The primary attributes of this system are its compact size and its configurability for use in diverse measurement apparata. The design uses a tripod base constructed out of fine adjuster screws in order to planarize the tweezers and bring them within the travel range of the z-piezo.

The tweezer scanner has $38\mu m$ of travel in all directions, so it is necessary to place the tweezer scanner within this level of precision. Although not diagrammed in fig. 4.1, this is accomplished with a low-profile forklift that is moved with a xyz micropositioner. This allows us to move the whole system over centimeters and then mechanically decouple the micropositioner from the tweezer scanner in order to minimize vibration and drift.

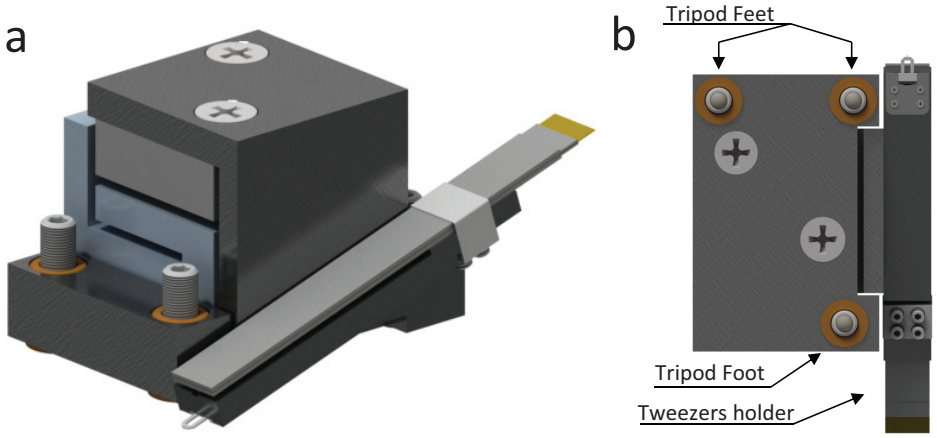

Figure 4.1: a) Orthographic rendering of compact tweezer scanner. Using the same tweezer holder and xyz piezo cube as described in Ch. 3 this tweezer scanner fits into a $23 \times 27.5 \times 44mm$ volume and is both vacuum compatible and designed to sit steadily on any planar surface. The xyz piezo cube is mounted on an adjustable tripod base, so the tweezers may be planarized to a surface of interest. b) A bottom view of the compact tweezer scanner with tripod feet located surrounding the center of gravity for stability.

4.1.2 Inverted microscope-mounted system

One important apparatus that the tweezers system can interface well with is an inverted microscope. In particular, we had previously constructed an optical microscope system that is equipped with high-NA objectives, fluorescence imaging capabilities, and a scanning laser system with a $1064nm$ $800mW$ diode laser, a Kr-Ar laser, and a supercontinuum white-light source. This set-up was built as a multipurpose tool for optoelectronic studies of nanomaterials in ambient (air or liquid) environments, with a particular focus on interfacing nanomaterials with biology. Added to this system, we attached a homebuilt tweezer arm mounted to a commercial micropositioner. As detailed in figure 4.2, we built the tweezer actuator system onto the shaft of a stepper motor that was in turn mounted to the micropositioner. The stepper motor serves to planarize the tweezers, but can also be configured for optical tomography.

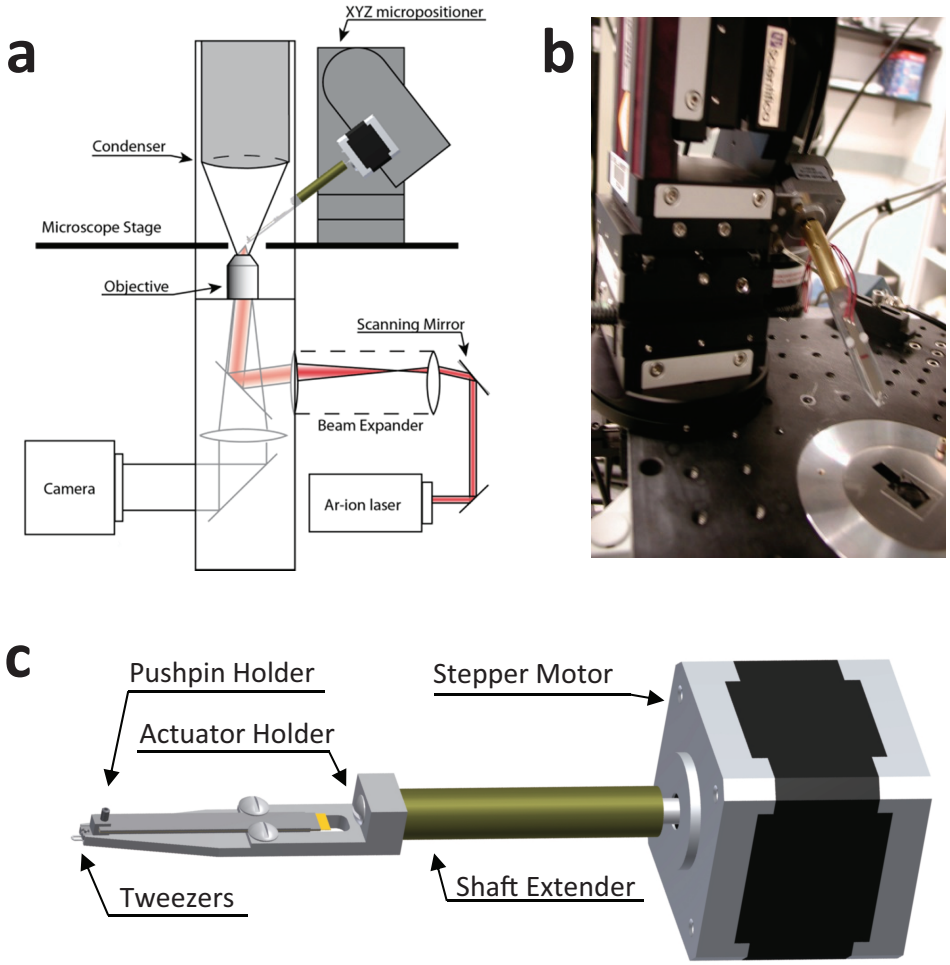

Figure 4.2: a) Schematic of tweezer apparatus built on an Olympus IX-71 inverted microscope. The tweezers are mounted to a Scientifica Patchstar micropositioner via a home-built rotation arm (shown in c). Attached to the optical microscope is a home-built scanning laser system for use in laser-based imaging techniques. The objective is mounted on a piezo positioner allowing programmatic control of focus. b) Image of assembled and installed tweezer apparatus. c) Rotation arm design. A commercially available stepper motor attaches to the commercial micropositioner. The tweezer actuator is then mounted on the stepper motor shaft to provide rotational control. Compared to design in fig. 3.5 in Ch. 3, there are fewer space constraints. A push pin holder is held directly onto the actuator with a set-screw. The actuator holder is attached to the shaft extender with with insulating attachments, separating the electrical grounds.

4.2 Optical imaging of CNT-tweezer system

The inverted microscope-mounted system relies on electrical feedback to indicate when a CNT is picked up, as was the case in the cryostat discussed in Chapter 3. While the cryostat allowed direct imaging of the CNT by incandescence, the microscope system utilizes the scanned laser to map the CNT position while interrogating its optoelectronic properties. Once a CNT is picked up, the CNT

source substrate can be moved away from the optical path of the microscope, and the tweezers and CNT can be imaged without any substrate or optical element between them and the objective (fig. 4.3a).

Optical characterization of CNTs is a mature field as reviewed in [51–54], but the unique geometry of the tweezers system is particularly well-suited for optics techniques because the CNT is freestanding without any structures in the beam-path. The first and most straightforward method we use is photocurrent microscopy (PCM). In PCM, a focused laser spot is raster-scanned over the CNT, and the resulting current is collected in a preamplifier and recorded. The resulting drain current is mapped into a colorscale image. In fig 4.3b, red indicates positive drain current and blue indicates negative drain current. The tweezers are visible due to a photothermal effect: the laser heated electrode drives a net flow of majority carriers towards to the colder electrode. On top of the electrode background, the CNT is visible due to a combination of photothermal and a direct photocurrent.

The next imaging technique we demonstrate is photoconductance [53]. This is a differential measurement that determines how the presence of the laser affects the overall conductivity of the CNT. We perform this measurement by applying an AC voltage on the source tweezer electrode and measure the resulting current with lock-in detection on the drain electrode while raster scanning the laser. An example photoconductance map is shown in fig. 4.3c, where blue is low conductance, and red is high conductance. There is notable background near the electrodes, but the signal from the tube itself is seen towards the center.

PCM and photoconductance measurements both rely on measuring induced currents in a CNT, however we can also image CNTs using purely optical means. By simply collecting the back-reflected light as the laser is scanned we can directly see the CNTs position. Fig. 3d is an example of two CNTs made visible by reflectance imaging. Previous work studying Rayleigh scattering from CNTs [51, 55, 56] required specialized measurement geometries to combat the effects of background scattering, suggesting that microtweezer approach may be fruitful in future studies.

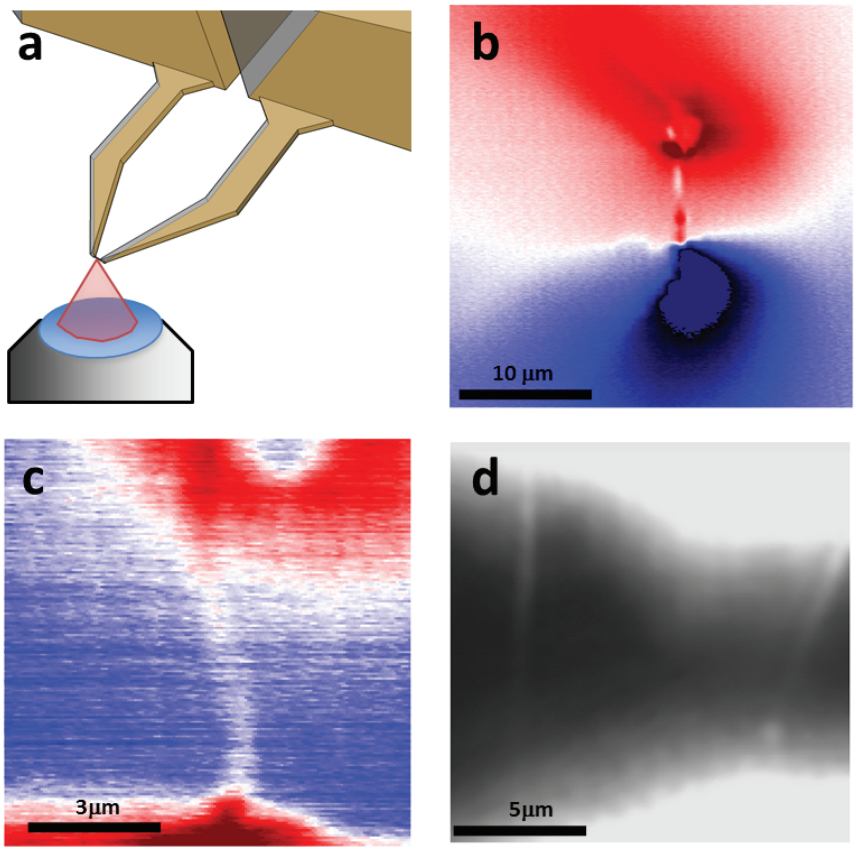

Figure 4.3: a) Schematic of tweezer with CNT above inverted micrscope objective. The physical gap between the tweezer electrodes reduces optical backscattering. b) photocurrent micrograph of single CNT spanning tweezer electrodes: blue indicates negative currents while red indicates positive. c) photoconductance micrograph of single CNT. conductance changes of 0.1% are seen in the tube. d) direct reflection measurements of two CNTs. There is minimal background due to the open architecture.

4.3 Electric measurements of CNT system

As a two-electrode system, the stand-alone tweezers offer limited access to the semi-conducting properties of CNTs. However, with the introduction of a gate electrode, the tweezers-CNT-gate combination creates a field-effect transistor with the CNT as the active element. The CNT field effect transistor has been studied for years [12–15], however, because the tweezers can be moved with respect to the gate substrate, we can modify the device geometry *in situ*. In particular, we modify the gate capacitance by moving the tweezers away from the substrate, as shown in the

schematic in fig. 4.4a. Holding the source-drain bias constant, we measure the CNT conductance at a series of calibrated steps in z, as seen in fig. 4.4b. The apparent effect is that the conductance vs. V_g response broadens with increased height.

The conductivity of a semiconductor goes as $\sigma = \sum n_e e \mu_e$ where n_e is the mobile charge carrier density, e is the charge of a single charge carrier, and μ_e is the mobility of charge carriers. Because e is constant and μ_e is a function of n, this means the variation in conductance stems from changing n. The gate voltage V_g serves to tune the carrier density capcitively: $n = c_g V_g / A$ where c_g is the capacitance/length and A is the cross-sectional area. This ultimately implies for any given CNT that the conductance goes as $G(c_g(z) \cdot V_g)$.

By taking the curve $G = G(c_g(z_0) \cdot V_g)$, where z_0 is the closest measured distance to the gate, and using nonlinear least-squares fitting to $G = G(c_g(z) \cdot V_g)$ for all z, we measure the relative capacitance vs. height, and plot it in fig. 4.4c. Had the initial height been well-known, this actually could serve as a purely electrostatic means of measuring the diameter of a CNT. This kind of measurement will be used routinely in subsequent chapters as a direct calibration of the detected vibrational motion of CNTs.

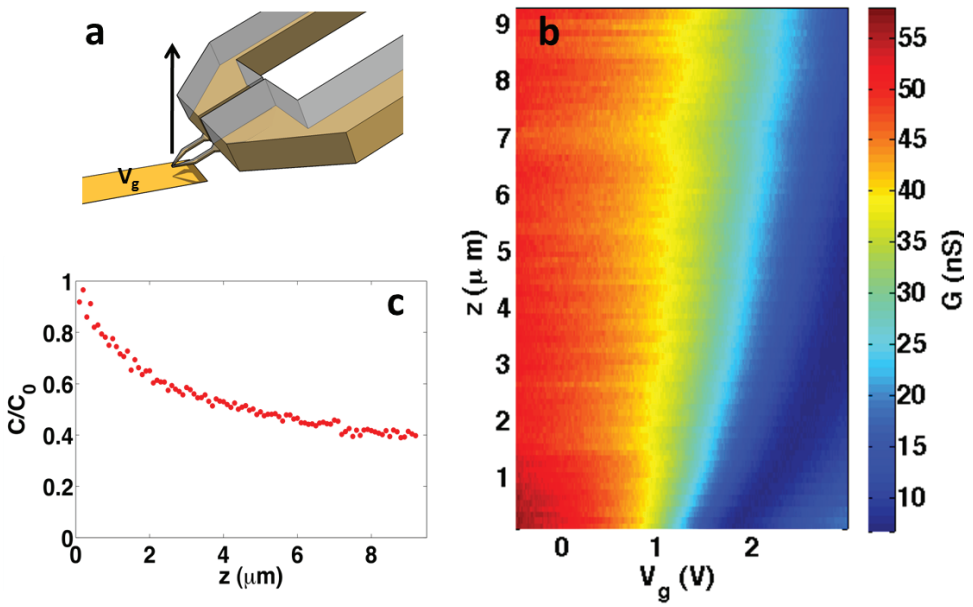

Figure 4.4: Measuring transistor properties with z-dependence. a) A substrate with an electrical gate is used to create a three terminal device. b) Conductance vs. V_g and z. I-V measurements are performed as the tweezers are moved away from the gate. When the distance is greater, the capacitance is reduced, making the gate less effective. The broadening of the transconductance vs. V_g with height can be used to compute the relative capacitance. c) relative capacitance computed by least-squares fitting of data in (b) at each z slice by the curve measured at the lowest z.

4.4 Optoelectronics and electromechanics combined

Combining the techniques described in the previous two sections by replacing the gate with a semi-transparent electrode, we show that we can electromechanically deform a CNT while tuning its electrical structure. With a thin layer of gold for a gate electrode, the CNT can be electrostatically gated while simultaneously performing PCM. In figure 4.5 we demonstrate an example of this style of measurement. In particular, we pick up a CNT and buckle it to produce a built-in static structure, as is most readily seen in the middle micrograph in fig. 4.5c. The transconductance can be measured and help identify the neutrality point near $V_g = 1V$ as seen in fig. 4.5b. Then a series of PC maps are recorded as a function of gate voltage. We show five representative maps spanning from $-5V$ to $7V$ symmetrically around the neutrality point. By gating, the tube is pulled towards the gate with an electrostatic force $F_g = \frac{1}{2}\frac{dC}{dz}V_g^2$. This results in the apparent straightening-out

of the buckled features in the CNT at large magnitudes of V_g. Simultaneously, as the CNT is gated through its neutrality point, the majority carriers go from holes at $V_g < 1V$ to electrons at $V_g > 1V$. Asides from necessarily imposing band bending, the most dramatic effect is the sign flip of the electrode photocurrent signal. The laser serves to heat one electrode, and the resulting current is due to the non-zero Seebeck coefficient of the CNT. To our knowledge, this is the first optical imaging of electromechanical deformations of a CNT.

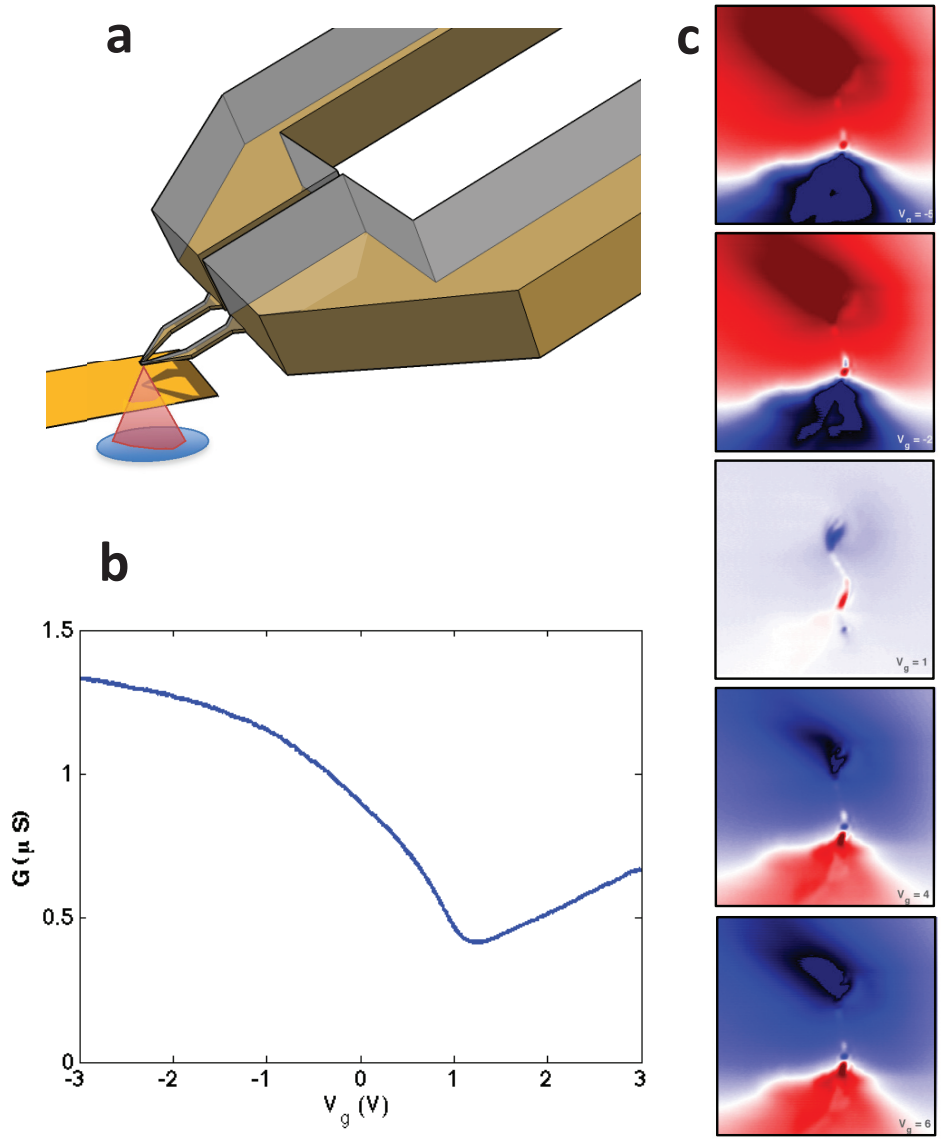

Figure 4.5: Simultaneous electro-mechanical and electro-optical manipulation of tweezer-spanning CNT. a) Using a semi-transparent gate electrode, the CNT is imaged with photocurrent mapping as the CNT is simultaneously gated and tensioned by the electric gate. b) The transconductance of a CNT, revealing a neutrality point near $1V$. c) Photocurrent micrographs of CNT in (b), spanning $-4V$ to $7V$ in $3V$ steps descending along the page. Two dramatic effects are visible: the photocurrent signals invert sign while crossing the neutrality point $V_{g0} = 1V$, and shape of the CNT varies with the magnitude of V_g where. The boundary conditions lock the CNT in an S-bend, as seen in the $V_g = 1V$ image and at large magnitude of V_g, the CNT is pulled towards the gate, apparently straightening out the CNT. The PC signal from the electrodes is photothermal [57], and the sign flips as the majority carrier changes.

4.5 Photocurrent tomography

Extending the observation that CNTs can have non-trivial conformations, we can utilize photocurrent imaging to reconstruct the 3-dimensional shape of the CNT, in order to extract useful information about its local environment. In order to reconstruct a CNTs position we use optical sectioning–iteratively recording PCM images while incrementally stepping the objective in z. Although the imaging is ultimately diffraction-limited, we can use centroid finding to localize the path of the CNT to within 10s of nm. This works because there is only one CNT present. Unlike confocal microscopy, we cannot reject out-of-focus light, but instead collect signal from all focal-planes. This results in an optical probe that is gaussian in profile and hyperbolic in the beam width, which we directly show in fig. 4.6b. A single z-slice (fig. 4.6a) actually provides 3D information based on the measurable defocusing, but with a full 3D map, we can simply create iso-surfaces around high intensity regions and generate 3D models as shown in fig. 4.6c. The particular device in fig. 4.6, reveals a case where the CNT is tensioned, but the tweezer electrodes are not coplanar.

Flexing CNTs requires very little force, so observing the shape change as the CNTs environment changes can serve as sensitive force probe. In a similar vein, CNTs are 1D semi-conductors, and are quite sensitive to their local charge environment. These environmental changes can be read-out quantitatively from the photocurrent signal itself. This paves the way for using CNTs as unique force and potential sensors in diverse environments. In the next section, we show initial work towards using this technique for bio-sensing.

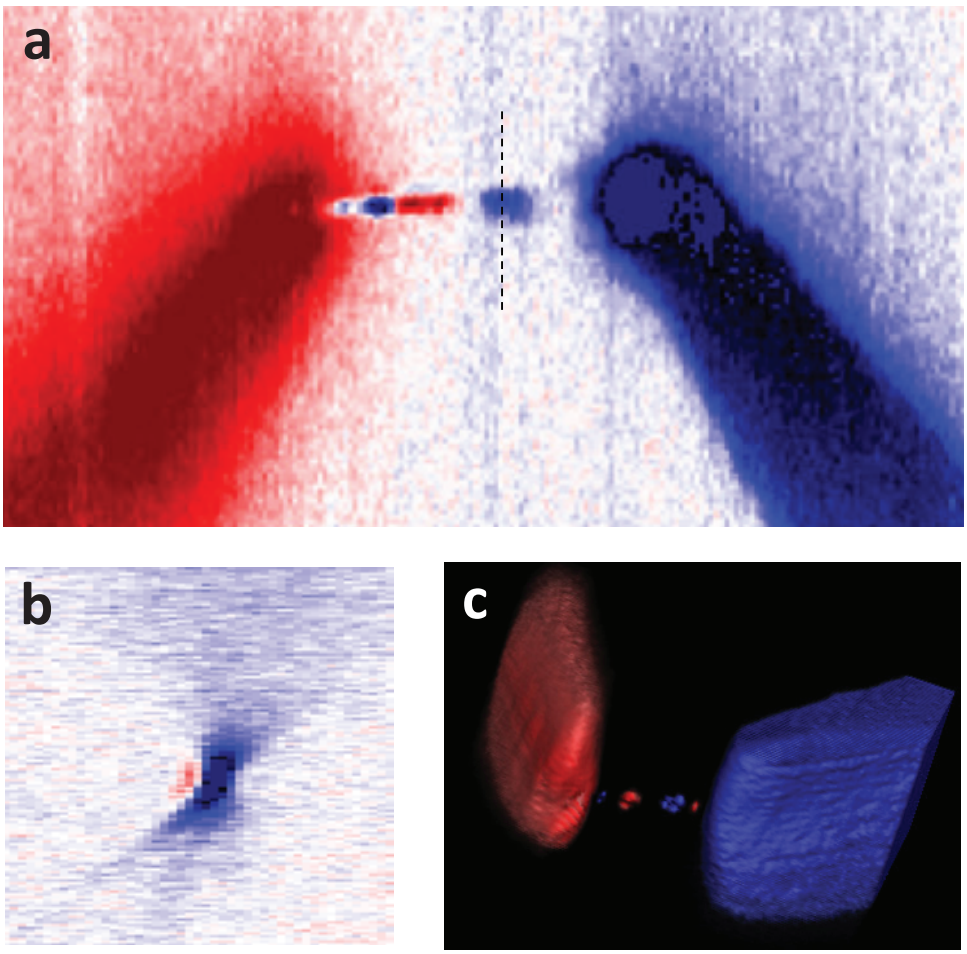

Figure 4.6: 3D photocurrent reconstructions. With tweezers and CNT held fixed on the microscope, photocurrent scans are performed while stepping the focus plane. a) Photocurrent micrograph at a fixed z. The left half of the CNT appears in better focus than the right half implying that the CNT is tilted. b) z-cut along the dotted line in (a). The hyperbolic optical probe shape is visible where the narrowest beam-waist corresponds to the in-focus position of the CNT. The apparent sign inversion near the focus spot is an artifact due to time-filtering along the fast-scan axis. c) 3D reconstruction from PC data shown at an oblique angle. All photocurrent signals having low magnitude are made transparent so only in-focus regions of the CNT are visible. Because of their finite width, electrodes appear artificially thick; the center-plane of the apparent volume locates the electrode position. As inferred from (a), the CNT is slanted, and this is a consequence of the red-electrode being bent down relative to the blue-electrode.

4.6 Towards tweezer-based biosensing

With the ability to measure and detect changes in CNTs shape and band-structure we made preliminary steps towards bio-sensing [58, 59] with our tweezer apparatus. Because much of the tweezer apparatus is exposed and metallic, we fastened tweezers onto the existing apparatus with adhesives and a piece of a glass microscope slide as seen in fig. 4.7a. The CNT source substrate can

then be submerged in water, and we pick the CNT up in solution. This eliminates the problem of the CNT breaking while crossing the air-water interface. We were able to successfully pick-up a CNT in DI water and image it using PCM; the resulting image is seen in fig. 4.7b. Having demonstrated that a CNT can be picked-up in solution, the final step will be to introduce a biological specimen in solution and interface the CNT with it.

At the time of this writing, we fitted out microscope with a stage heater and have been able to successfully keep mouse cortical neuron cells alive for approximately 30 minutes and image them optically (fig 4.7c). Further, the cells survive the presence of a CNT source substrate and interaction with the tweezers. To date, we have not successfully brought a CNT into contact with a live cell, however the initial results are encouraging. In a successful experiment, we would hope to both learn about the CNT-lipid bilayer interface, and be able to probe the electrochemical environment inside the cell.

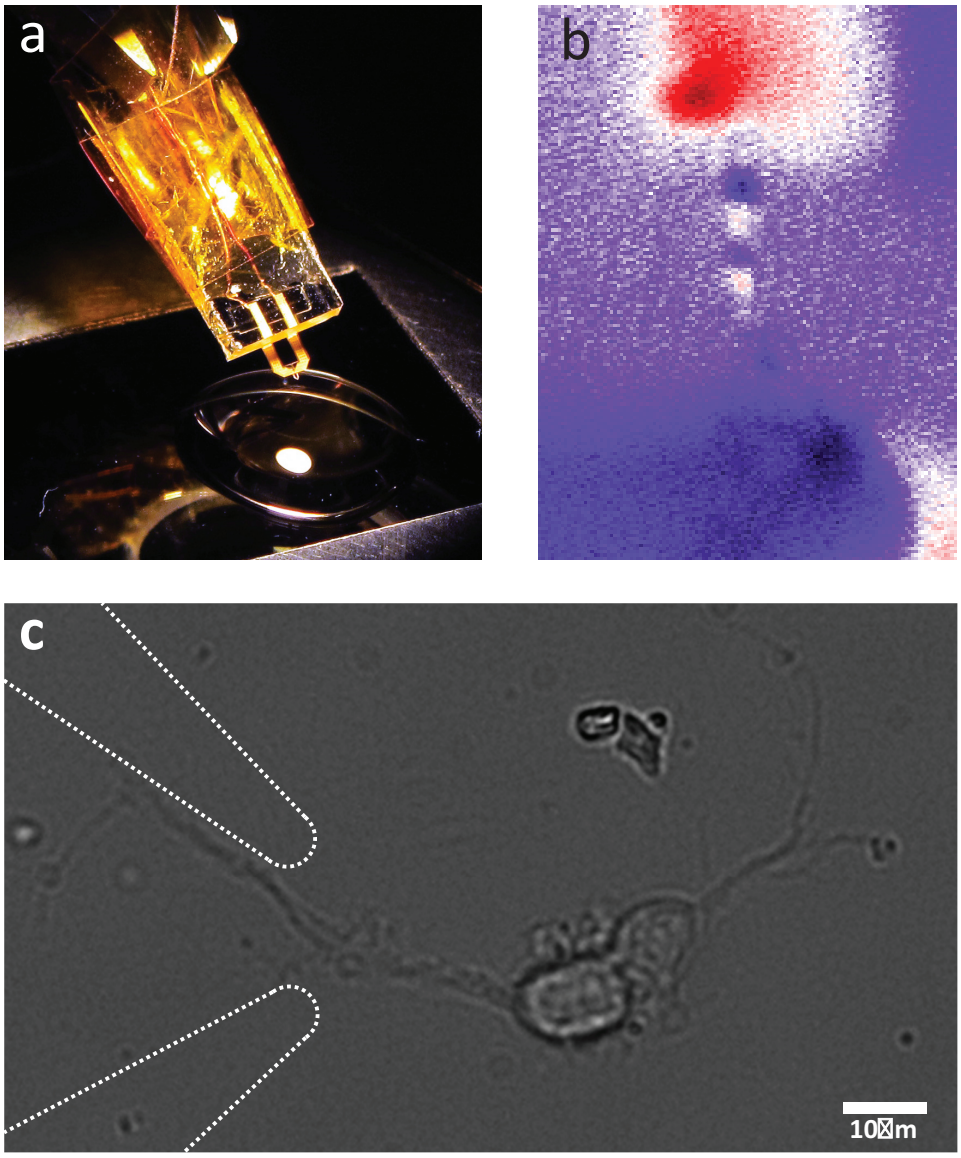

Figure 4.7: a) Image of CNT tweezers inserted into liquid. b) Photocurrent image of CNT picked-up in DI water. c) Image of tweezers spanning a live neuronal cell. There is no CNT in this image. The ability to pick-up CNTs in solution suggests that CNTs can be inserted into a live cell and imaged by photocurrent. All materials of the tweezer-CNT system are biocompatible.

4.7 Electromechanical Resonance

Having explored the possibility of using our CNT microtweezers in an ambient environment, we complete our survey by discussing our initial work studying vibrational properties of CNTs in vacuum. Recreating a device geometry similar to that used in fig. 4.4, we install our tweezers into a custom-built cryogenic probe-station and bring a CNT into proximity of an electrical gate. Rather

than using the gate to apply static forces, we now apply both static and oscillating forces to tension and vibrate the CNT, detecting its motion electrically. Historically these resonance measurements are done using an electric mixing technique [60] but our device geometry truly minimizes gate-drain leakage, enabling us to directly detect CNT motion. Specifically, the gate leakage is minimized by placing the CNT near the edge of the gate (fig. 4.8b). The height of the CNT over the gate affects its capacitance and thus modifies its conductance (which we explicitly measured in fig. 4.4). Thus as a CNT vibrates, an AC current is measured $I_{AC} = z_{ac}\frac{dG}{dz}V_{sd}$. Using lock-in detection, we can measure the out-of-phase quadrature, and thus completely remove the electronic background from our mechanical measurement. This allows us to take resonance spectra as a function of V_g with additional phase information. Now, taking advantage of the tweezer actuation mechanism, we can separate the tweezers and thus tension the CNT, causing the resonance modes to rise, shown in fig. 4.8c and 4.8d.

In this chapter we explored a variety of ways the tweezer architecture can be applied in novel measurements. For the remainder of this thesis, we will focus exclusively on our studies of CNT vibrational properties, first performing in-depth measurements of CNT thermal-physics using the device geometry shown in fig. 4.8, followed by coupling vibrating CNTs to high-Q optical microdisk resonators. Having dynamic control over many degrees of freedom with the tweezers opens up a number of possibilities, and as the subsequent chapters show, has been useful in understanding the truly unique physics observed in CNT resonators.

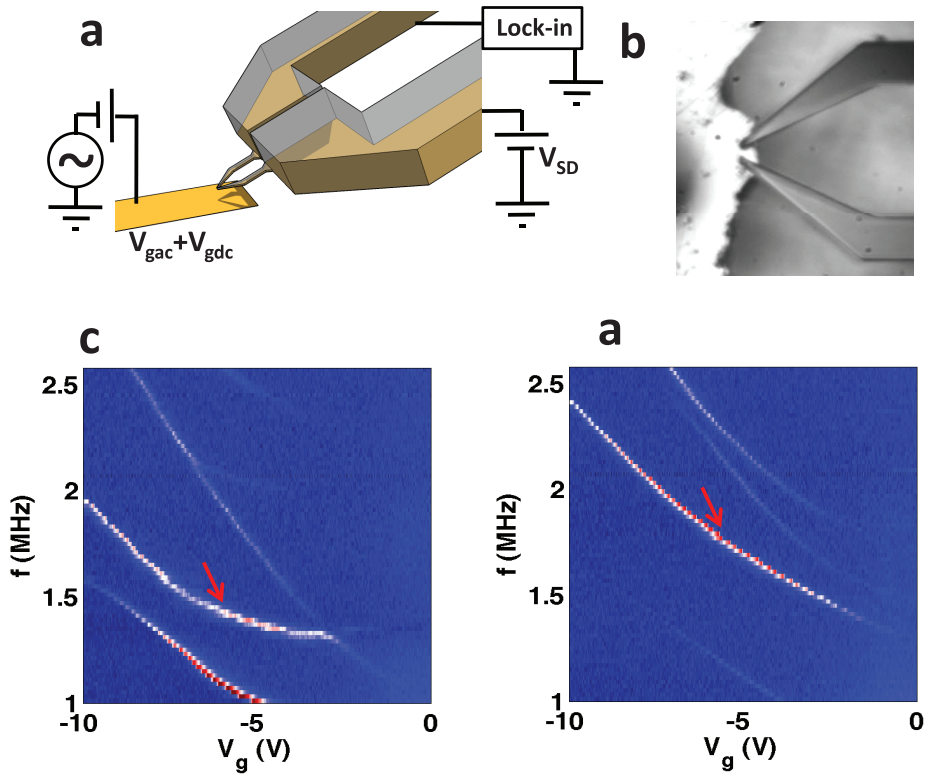

Figure 4.8: Electromechanical resonator with tweezer-spanning CNT. a) Schematic of electromechanial resonance measurement. Tweezers are held over electrical gate, AC voltage on the gate applies capacitive driving force on CNT, and motion is measured by lock-in detection of the CNT conductance: vertical CNT displacement modulates CNT conductance. b) optical micrograph of tweezers with CNT over the edge of gate electrode. This geometry minimizes gate leakage. c) Resonance spectra of CNT tuned by V_g. Direct-detection is employed and the out-of-phase quadrature is plotted. This represents the purely mechanical dissipative response. d) Specra of same CNT in c) after tweezer separation is increased. arrows in (c) and (d) label the same resonance mode to indicate frequency shift due to CNT tensioning.

Chapter 5

Measurements of fluctuation broadening

5.1 Introduction

Having discussed the many possible applications of our CNT microtweezers, we now focus in this chapter on our work studying CNT resonator mechanics. From the time the first field-effect CNT resonator was measured [60], there has been a number of fascinating and surprising observations, including an unexpectedly low quality factor. On top of this, many CNT resonator properties proved to be highly temperature dependent, including both frequency shifts and the quality factor [4, 61]. As we discussed in chapter 2, CNTs are truly unique as resonators for the scale: their bending stiffness tends to be several orders of magnitude less than any top-down fabricated nanoresonator, and this feature, we predicted [16], would naturally lead to the measured low quality factor. Recent results following this approach found a particular manifestation of fluctuation broadening; in this chapter we discuss our measurement methods and our finding that fluctuation broadening quite generally accounts for measured room temperature quality factors in CNT resonators. In addition to this, we show that fluctuation broadening can lead to spectral drift of a resonance mode or it can truly control the energy decay rate out of a resonance mode.

5.2 Measurement system

In order to study the resonance properties of CNTs with our tweezer platform and applying a variety of RF measurement techniques, we connect several V_{gAC} and I_{measAC} sources and sinks simultaneously, as diagrammed in fig. 5.1. Using a labview interface, DC voltages V_{gDC} and V_{SD} are set using a National Instruments DAQ interface, or a Yokogawa voltage source. V_{gDC} passes through the lowfrequency port of a bias-T while V_{SD} is directly connected to the source electrode. V_{gAC} is sourced either by a network analyzer (Agilent 8753ES) or a programmable function generator (Tektronix AFG3000) and passes through the RF port of the same bias-T. The drain current is measured by a home-built broadband transimpedance amplifier, the amplified signal is split by another bias-T, and the DC component is measured with the NI DAQ interface. The remaining I_{AC} is boosted with a voltage amplifier and then divided among different RF read-out devices: the network analyzer, lock-in amplifier (SR830), and digital oscilloscope (Lecroy waverunner LT374 or Picoscope 5244B). Although dividing signals reduces signal strengths, it is necessary, as reconfiguring the circuitry between measurements can damage the CNT, either due to movement of the tweezers or electrical discharge. The primary current-noise sources are the CNT and the transimpedance amplifier, meaning that the voltage amplifier and subsequent power splitters do not affect signal fidelity.

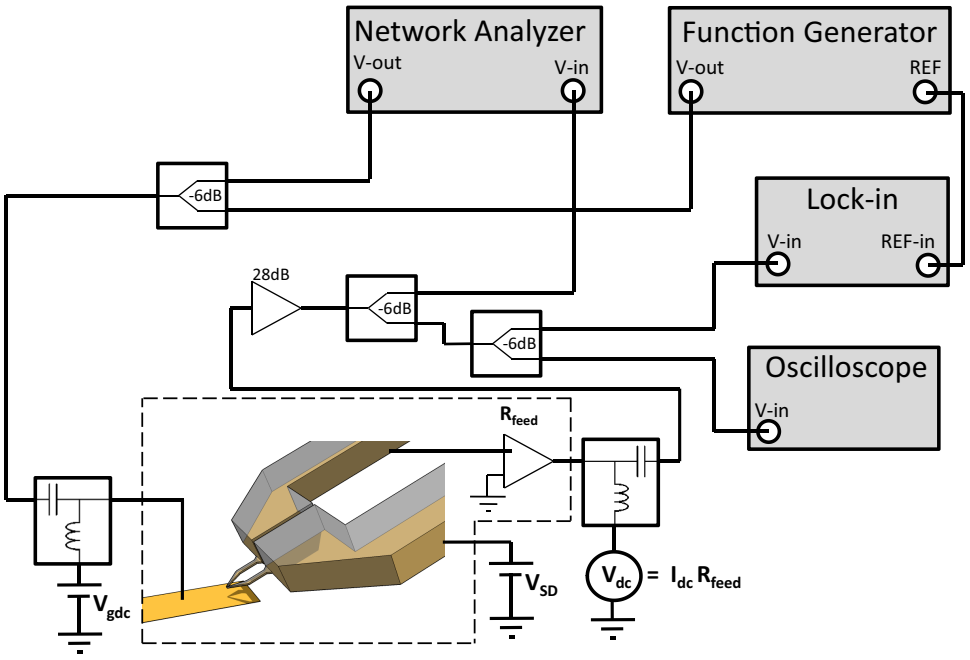

Figure 5.1: Tweezers resonance detection schematic. A dc V_{SD} is applied to the system on a source electrode, while both RF and dc V_g is applied to the gate. A home-built transimpedance amplifier collects the RF and dc I_{meas} and ports the signal out of the cryostat (indicated by dotted line). DC component is read in by a computer interfaced ADC, while the RF component is boosted and split amoung three measurement devices. Not all instruments are simultaneously opperated, but remain connected to preserve the experimental conditions between measurements.

5.3 Absolute displacement calibration

Relying on two important features of our measurement system–direct electrical detection of CNT motion and control over z-displacement–we are able to make absolute calibrated measurements of CNT displacements and thus weigh our CNTs and infer its absolute elastic properties. Our protocol involves measuring the conductance properties of a CNT as a function of height, inferring its initial height, computing the current-displacement sensitivity (dI_{meas}/dZ), and converting AC-current measurements into z-displacements.

In our particular example, we study an ambipolar [62] device with apparent Schottky barrier contacts as seen in fig. 5.1a. First, we measure the conductance of our CNT at a fixed height. We map the conductance over all relevant V_{sd} and V_g (fig 5.2a. is a linecut of fig. 5.2b) and find that this device has super-linear I-V characteristics, particularly at negative V_g. From the stand-point of

height calibrations, this indicates that the current-displacement sensitivity will non-trivially depend on both V_g and V_{sd}.

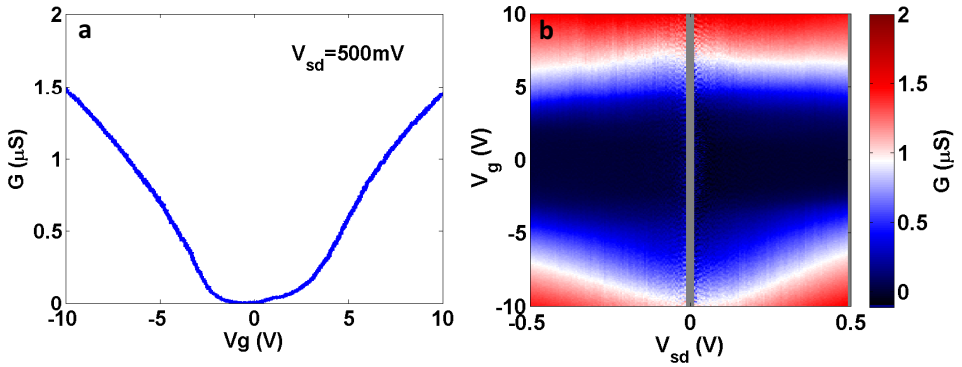

Figure 5.2: a) Conductance trace of ambipolar CNT. b) map of conductance vs. V_g and V_{sd}. This CNT shows Schottky barrier contact behaviors with noticable V_{sd} dependence. Data near $V_{sd} = 0$ is discarded because the SNR< 1 in that region.

We next measure the height dependence of the CNT response (analogous to analysis in Ch. 4). Starting at the original displacement, the CNT is moved away from the gate while G vs. V_g sweeps are measured. Figure 2a shows the data, plotting successive conductance traces from low-z in black to high-z in red. Because $G \approx G(CV_g)$, the relationship:

$$\frac{C(z)}{C(z_0)} = \frac{V_g\left(G_0, z_0\right)}{V_g\left(G_0, z\right)} \tag{5.1}$$

applies for either the $V_g > 0$ or $V_g < 0$ branch of $G(CV_g)$. Selecting G_0 in eqn. 5.1 at a high slope region of G provides a good measure of the relative capacitance, plotted in fig. 5.3b. This protocol can be repeated at several G_0 and averaged, or nonlinear least-squares fitting can be applied, as in Chapter 4. All methods produce similar results. It is noteworthy that the resulting measured functional form of the data in fig 5.3b does not directly map to the theoretical relationship of C to z of a wire over an infinite plane. This discrepency is attributed to the finite length of the CNT and screening by the tweezers. Depending on the tweezer height, these effects can significantly reduce the mutual capacitance between the CNT and the gate, but the extracted $d\ln C/dZ$ will be correct to within an order of unity for the tweezer geometry.

We now have a normalized capacitance vs. height, and aim to calculate the conductance-displacement sensitivity dG/dZ. Starting from the relationship:

$$\frac{dG}{dZ} = \frac{dG}{dV_g}\frac{dV_g}{dZ} \tag{5.2}$$

we can solve for the last term in terms of the capacitance equation:

$$\frac{d\ln C}{dZ} = -\frac{d\ln V_g}{dZ} = -\frac{1}{V_g}\frac{dV_g}{dZ}. \tag{5.3}$$

The conductance-height sensitivity is now, in terms of measured quantities:

$$\frac{dG}{dZ} = -\frac{dG}{dV_g}V_g\frac{d\ln C}{dZ}. \tag{5.4}$$

This calculation is performed on the data represented in fig. 5.2b and fig. 5.2b and plotted in fig. 5.3c. Specifically, a numerical derivative $\frac{\Delta G}{\Delta V_g}$ is calculated from fig. 5.2b, and the logarithmic derivative $1/C\Delta C/\Delta Z$ is calculated near $\Delta Z = 0$ from fig. 5.2b. Because this is inherently noisy, a piece-wise smoothing function is used to produce the final data shown in fig. 5.3c. We thus have a calibrated displacement sensitivity, which we will recast into experimental units $\frac{dI}{dZ} = V_{sd}\frac{dG}{dZ}$ and plot in fig. 5.3d. As can be seen in the data, the greatest measurement sensitivity is at large values of $|V_g \cdot V_{sd}|$. This particular formulation is useful, first, because it directly converts measured quantities into absolute displacements: $Z_{meas} = \left(\frac{dI}{dZ}\right)^{-1} I_{meas}$ and second because it gives a measure of the noise floor: $S_z = \left|\frac{dI}{dZ}\right|^{-1} S_I$ where S_z and S_I are the displacement and current power spectral densities of the system noise. This calibration will prove useful in both coherent, driven measurements as well as thermal measurements as will be discussed below.

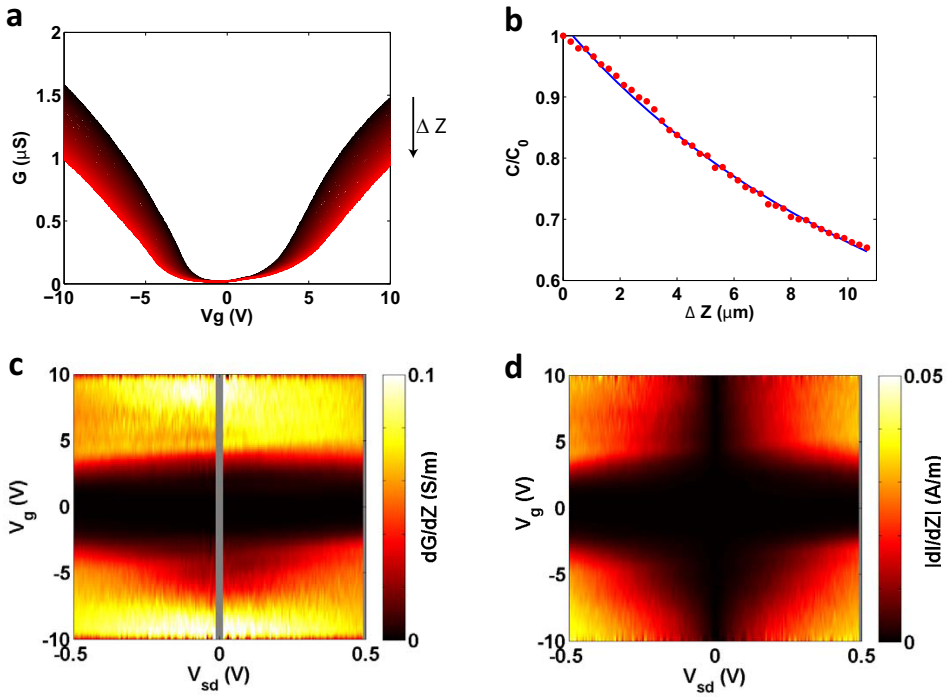

Figure 5.3: Conductance of CNT measured at constant bias $V_{sd} = 500mV$ as a function of height. From initial position, CNT is raised $\Delta Z \sim 10\mu m$ and corresponding conductance curves are plotted from black to red in increasing Z. b) extracted relative capacitance following protocol from Ch. 4. Data is in red, and fit line in blue. c) colormap of conductance displacement sensitivity as a function of V_g and V_{sd} at a fixed ΔZ. Data is smoothed along V_g axis in order to perform numerical derivative. d) Absolute signal displacement sensitivity. Z displaements are calculated by dividing measured current signals by this value for a given V_g and V_{sd}.

5.4 Direct detection of CNT resonance

As discussed in Ch. 4, we are able to perform direct-detection [63] measurements on our CNT resonators on account of the minimal stray capacitance in our device geometry and due our implementation of a low-noise broad-band transimpedance amplifier. In our first example of resonance detection, we will use the network analyzer to drive V_{gAC} and detect I_{measAC}. Picking a constant V_{gAC} and V_{SD}, the network analyzer measures spectra as V_{gDC} is swept. Here the tube experiences a capacitive force: $F_c \approx \frac{1}{2}\frac{dC}{dZ}\left(V_{gDC}^2 + 2V_{gDC}V_{gAC}\right)$. The measured AC current response, in phasor notation then should be:

$$\widetilde{I}_{AC}(\omega) = i\omega C\widetilde{V}_{gAC}(\omega) + \frac{dG}{dV_g}V_{sd}\widetilde{V}_{gAC}(\omega) + V_{sd}\frac{dG}{dZ}\left[\frac{dC}{dZ}V_{gDC}\widetilde{V}_{gAC}(\omega)\right]\widetilde{\chi}(\omega) \tag{5.5}$$

where the tilde denotes a complex value, and $\widetilde{\chi}(\omega)$ is the linear response function of the resonator– the quantity we hope to measure. The first term in eqn. 5.5 is a capacitive background, the second is the differential conductance of the CNT, and the third is the electro-mechanical driven response of the CNT. While the first two terms are purely electrical in nature, they serve as a useful means of calibrating phase-response of the system. Specifically, by operating at small $|V_{sd}|$, the 2^{nd} two terms drop out, resulting in a purely capacitive response. Due to the delay times associated with the length of coaxial cables in the circuit, the measured response has frequency-dependent phase delays, which can be measured and nulled out from the first term in eqn. 5.5. Following this protocol, the out-of-phase and in-phase components of the frequency response are plotted in fig. 5.4 (with the capacitive background subtracted off). The second term in eqn. 5.5 is purely in-phase, and amounts to a differential conductance measurement of the CNT electrical response. This is apparent in the background of fig. 5.4a, where current goes from negative to positive in increasing V_g. In fact, averaging across frequencies below $500kHz$ (where there is no mechanical resonance) and performing the integral $G = \int \frac{dG}{dV_g} dV_g$ reproduces the conductance response (fig 5.2a) with quantitative agreement. Finally, the mechanical response registers as Lorentzian peaks in the out-of-phase component, and sigmoidal curves in the in-phase response; as shown in fig 5.4b.

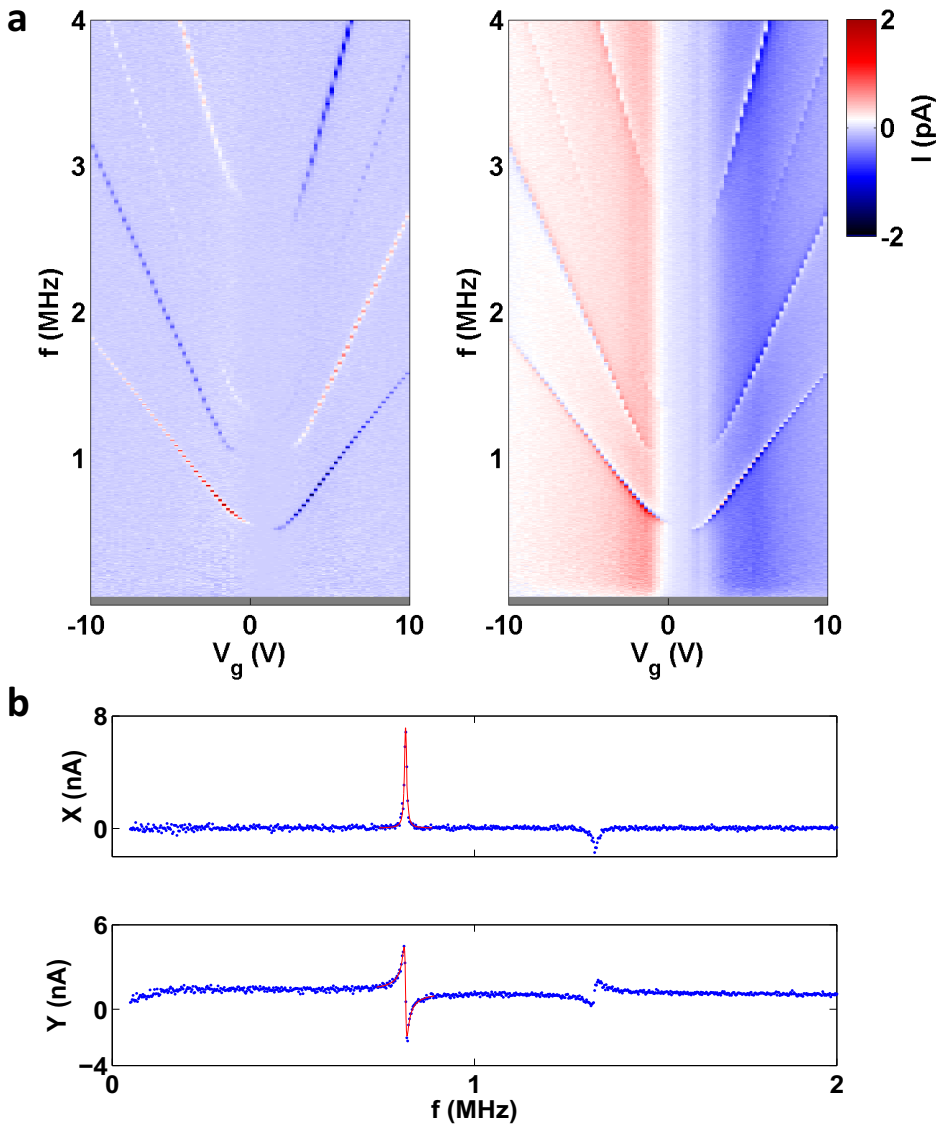

Figure 5.4: Direct detection of mechanical resonances. a) out-of-phase and in-phase quadratures as measured by lock-in detection. Phase-delays and capacitive background signals are removed by fitting response at low V_g. In-phase quadrature shows in-phase mechanical response as well as differential transconductance. Integrating over the differential transconductance numerically quantitatively reproduces the transconductance plot in fig. 5.2a, indicating good measurement fidelity. b) resonance spectra corresponding to line-cuts of data in (a) at $V_g = 2.5V$ Data is in blue dots, and fits are in red. There is minimal skewness, suggesting that the response is in the linear regime.

5.5 Ringdown measurement

While the quality factor Q can be measured from the width of resonance peaks $(\delta f_{FWHM}) = fQ^{-1}$ as discussed before, the relation between this and the energy dissipation $Q_E = 2\pi\frac{E_{cavity}}{P_{loss}}$ is only

implicit. For example, the measured line-width may stem from slow-varying spectral diffusion where the energy loss rate is actually smaller than predicted based on the spectral linewidth. In order to resolve this, we perform the first-ever single-shot ringdown measurements on a CNT resonator. This way, we can measure the timescale over which energy decays out of an excited resonance mode.

In our ringdown measurements, a fixed V_{sd} is held and the conductance through the tube is mapped into displacement, as was true for driven measurements. Rather than using a coherent source to drive a resonance mode, a function generator is programmed to send short voltage pulses to V_g to source an impulse force on the CNT. The resulting current response is read-in with a digital oscilloscope and stored. The pulse width Δt is selected to be short enough to actuate modes up to a frequency $\sim 1/\Delta t$ but not so short that the total impulse is negligible.

We performed ringdown measurements on the CNT discussed in fig. 5.4 and show the results in fig. 5.5. An example trace of a ringdown time-trace is shown in fig. 5.5b, where $t = 0$ is at the trailing edge of the voltage pulse. As can be seen, the CNT starts with a high-amplitude displacement, and oscillates as the amplitude of oscillation decays. An exponential fit of this decay yields a characteristic timescale τ, which is related to Q_E by the relationship $Q_E = \pi f \tau$. This relationship is true because each measurement is a *single-shot* ringdown measurement, and is thus insensitive to spectral drift.

Performing several ringdown measurements as a function of V_g, we can compare the two versions of Q as a function of f. We show power spectra of the various different ring-down measurements, and display them in a colormap in fig. 5.5b. This primarily serves as an indicator of the resonance frequencies excited as a function of V_g. Comparing fig. 5.5a and 5.4a, we can see that the tweezers drifted in the positive z-direction between measurements, as the resonance modes are tuned less at high $|V_g|$. Nonetheless, we can measure Q and compare Q *vs.* f, as shown in fig. 5.5c. While the frequency ranges spanned are different, there is good agreement between the two measurement techniques. We will discuss the quality factor and the relationship between driven and ring-down measurements more later in this chapter.

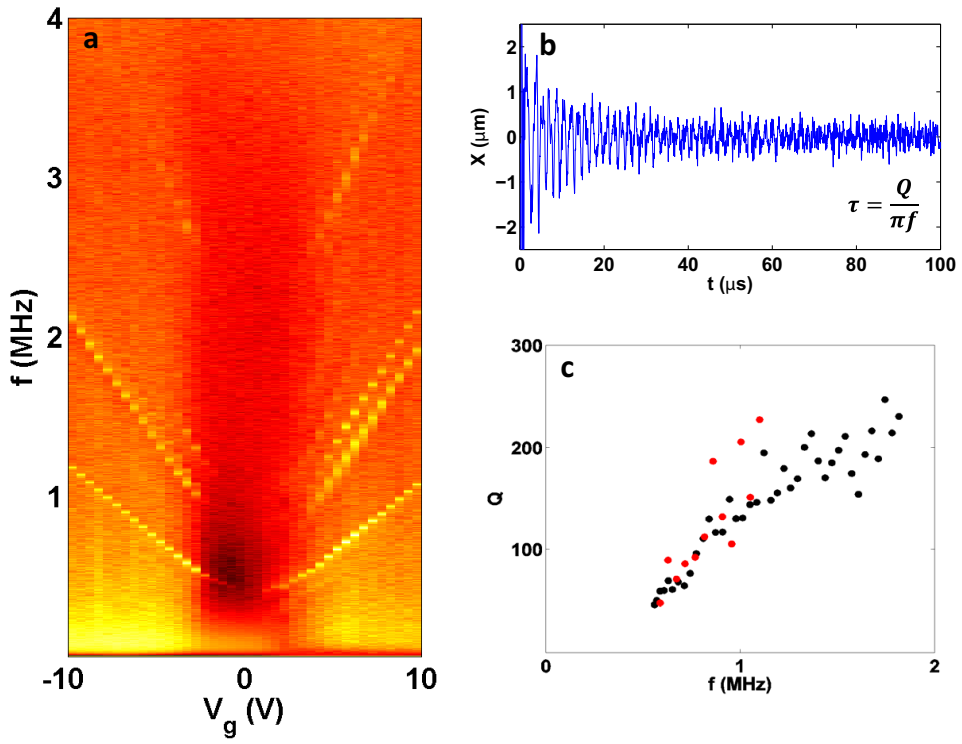

Figure 5.5: Ringdown measurements on the same CNT as in fig. 5.3. a) PSD resonance map extracted by finite-time FFT performed on ringdown measurement traces. This serves as a qualitative measure of which resonance modes are excited, and a quantitative measure of the center frequencies. b) An example ringdown trace with normalized displacements after CNT is plucked with a $5V$, $300ns$ gate voltage pulse. Fits are performed on the envelope of ringdowns to calculate decay time τ. From τ the quality factor is calculated and plotted in (c) in red. Data in black are extracted from fig. 5.3, showing good agreement over the frequency range compared.

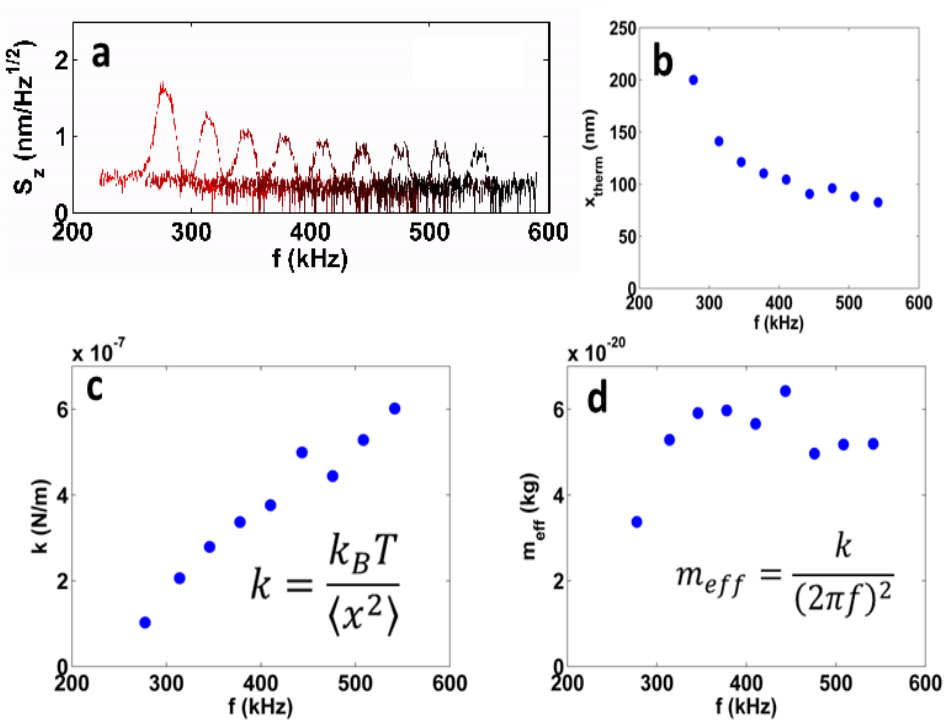

Figure 5.6: a) Normalized thermal PSD measurements for a single device tuned by gate voltage. The gate voltage goes from $1V$ to $9V$, from red to black. b) Thermal amplitudes from integrating under each reasonance in (a). c) Resonance mode spring constant as measured by application of equipartition theorem. d) Mass of tube measured using k from (c) and the center frequencies in (a).

5.6 Direct-detection of thermal motion of CNT

While thermal fluctuations are presumably an integral part of CNT mechanics, they have been historically difficult to measure, and to date, room-temperature electrical detection of thermal motion has not be reported. Taking advantage of our low-noise detection system, we are able to simply turn off all driving mechanism, and record the electrical response with a spectrum analyzer, or digital oscilloscope. In figure 5.6, we analyze the thermal power spectral density (PSD) of a CNT as its frequency is tuned by a gate-voltage. In fig. 5.6a, we plot 9 different PSDs measured of a single resonance mode, pulled by a gate with voltages from $1V$ to $9V$. As can be seen, the resonance amplitudes decrease with increasing frequency. By integrating under each PSD, we measure the squared thermal amplitude: $\langle x^2 \rangle = \int S_{xx}(f) df$ where $S_x x$ is the single-sided PSD for

the x-coordinate. For the case of a Lorentzian, this integral is equal to $\frac{\pi\delta f}{2}S_{xxpeak}$ where δf is the full-width half maximum and S_{xxpeak} is the PSD value at the peak of the Lorentzian. Therefore, the fitting parameters from least-squares fitting of the data directly provide the necessary integral while eliminating systematic bias due to the electronic background.

Carrying out the fit, we extract the thermal amplitudes, spring constants, and the mass of the CNT as plotted in fig 5.6b, 5.6c, and 5.6d respectively. The first primary observation is that the thermal amplitudes are extraordinarily large–an order of magnitude greater than the diameter of the CNT. This is an extreme rarity for any nanomechanical resonator larger than the molecular scale, and indeed this ultimately contributes to the unique physics of CNT resonators. These large amplitudes are a consequence of the equipartition theorem and demonstrate how soft CNT spring constants are (fig. 5.6c) where k is the Hookian spring constant for transverse deflections of the CNT. Finally, this analysis allows us to directly measure the mass of the CNT. Because the frequency (f) of a resonator is set by the spring constant (k) to mass (m) ratio, and the PSD provides both k and f, the mass is measurable from each spectrum. As can be seen in fig. 5.6d, the computed mass is approximately constant over the range of the experiment, and the computed value agrees well with the theoretical mass of a $1nm$ diameter CNT. Asides from its implications for the thermal physics of CNT resonators, knowing the CNT mass can aid in calibrating the capacitive force in driven or ringdown measurements.

5.7 Resonance mapping with strain

Having demonstrated the ability to measure CNT resonances using direct electrical detection during driven measurements, ringdown measurements and thermal measurements, we now seek to study how geometry can affect resonance properties. To date, nearly all CNT resonator measurements are performed on resonators with unknown, built-in strain, and this unknown variable has made systematic study of CNT thermal physics difficult. With our tweezer apparatus, we are able to strain the CNT while monitoring its resonance properties.

5.7.1 Strain calibration

Before discussing data, we first touch on an important note on calibration. In order to apply strain to CNTs, the tweezers are opened and closed by a computer-controlled piezo actuator. The operating principle for this is described in Ch. 4. In the process of opening and closing, the tweezers will naturally deflect in the z-direction, and their separation will increase or decrease an uncalibrated amount. Maintaining the vertical tweezer position is important to prevent the tweezers from crashing and to maintain the CNT-gate capacitance, while calibrating and monitoring the tweezer separation is important because piezo hysteresis prevents a direct mapping of piezo-voltage to tweezer position.

First, in order to account for the z-deflection, a capacitive feedback mechanism is used. Although the gate-drain capacitance is minimized in our measurement geometry, it is non-zero and serves as a measure of the tweezers height above the substrate. Every time the tweezers separation is modified, the computer interface is programmed to send an AC voltage to the gate with a function generator, and read the response with a lock-in amplifier, and feed the signal into a computerized PID controller.

Next, in order to measure the tweezer separation, we employ a computer-tracking algorithm to measure the relative separation of the tweezers with sub-pixel resolution. During the course of a measurement, a time-lapse video is recorded, and then post-processed to extract the separation. The algorithm tracks the position of edges on each tweezer cantilever using a maximum gradient edge tracking algorithm. The video frames are first gaussian blurred, and then the gradient-squared is numerically computed (shown in fig. 5.7b). The user then defines polygons that encompass part of an edge to be tracked (see the white boxes in fig. 5.7a), then the computer algorithm will find the maxima of several line-cuts across the edge. Finally, the algorithm uses linear fitting to find the best-fit line defined by these maxima. This approach measures tweezer separation with $\sim 30nm$ precision and it provides an accurate means of measuring CNT strain.

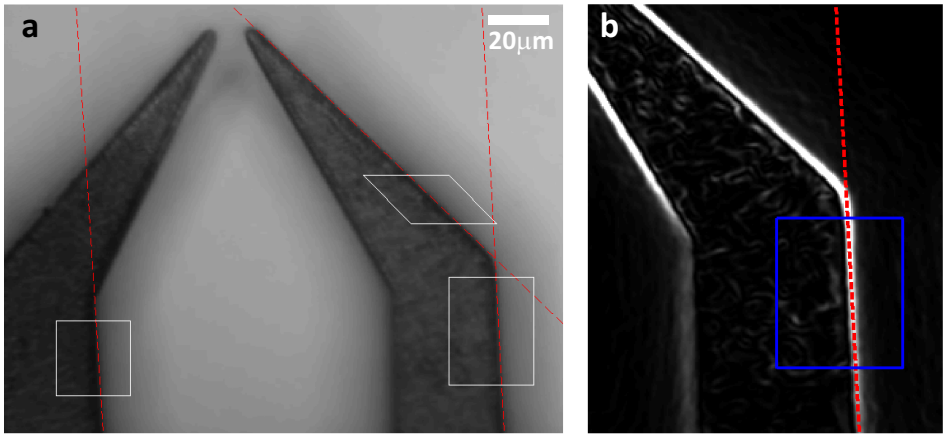

Figure 5.7: a) Optical micrograph of tweezers in operation. Edge tracking on three edges is used to accurately track the separation of tweezers. The two edges tracked on the right are used as a reference for the x and y drift of the tweezers, and the edge on the left is measured with respect to that reference. b) Gradient edge finding. A numerical gradient is computed from the micrograph and then squared. The user selects a region, shown as a blue box, and the software takes line cuts across the edge, find the maximum of linecuts with sub-pixel resolution, and performs least-squares fitting on the maxima to define the edge.

5.7.2 Three dimensional resonance mapping

With the technical ability to apply an accurately measured strain to a CNT at a fixed height above the gate electrode, we are able to systematically probe the CNT resonance response to capacitive gate voltage forces as well as strain. Given our low-noise electrical detection methods, we are able to record high-resolution resonance maps as a function of both V_g and ϵ over a one-day timescale; one such data-set is shown fig. 5.8. As can be seen, slices at constant ϵ are typical of fixed-geometry V_g-controlled resonance measurements, but applying strain can dramatically affect resonance modes. We will utilize this strain information to understand the emergent quality factor in CNT resonators,

Constant frequency contours, such as that in fig. 5.8b, serve as a good means of determining the effective slack of the CNT. The contours of a given resonance mode, at a constant frequency should map to contours of constant tensile force (F_T), as long as the resonance mode is tension-dominated at the particular frequency. F_T is set by the downward capacitive force $\frac{1}{2}\frac{dC}{dZ}V_g^2$ and the slack as enforced by force-balance. Specifically: $\epsilon_{clamp} = \epsilon_T - \frac{F_g^2}{8F_T^2}$, where ϵ_{clamp} is the separation of the tweezers relative to the length of the tube, and ϵ_T is the $V_g = 0$ strain for the given F_T. In

experimental units, the relationship becomes:

$$\epsilon_{clamp} = \epsilon_T - \frac{\frac{dC}{dZ}^2}{32F_T^2} V_g^4. \tag{5.6}$$

This explains the quartic contour in fig. 5.8b, and it can serve as an alternative means of measuring $\frac{dC}{dZ}$. Similar analysis can be performed on constant strain contours (e.g. fig 5.8c), using the slope $\frac{df}{dV_g}$ to measure $\frac{dC}{dZ}$.

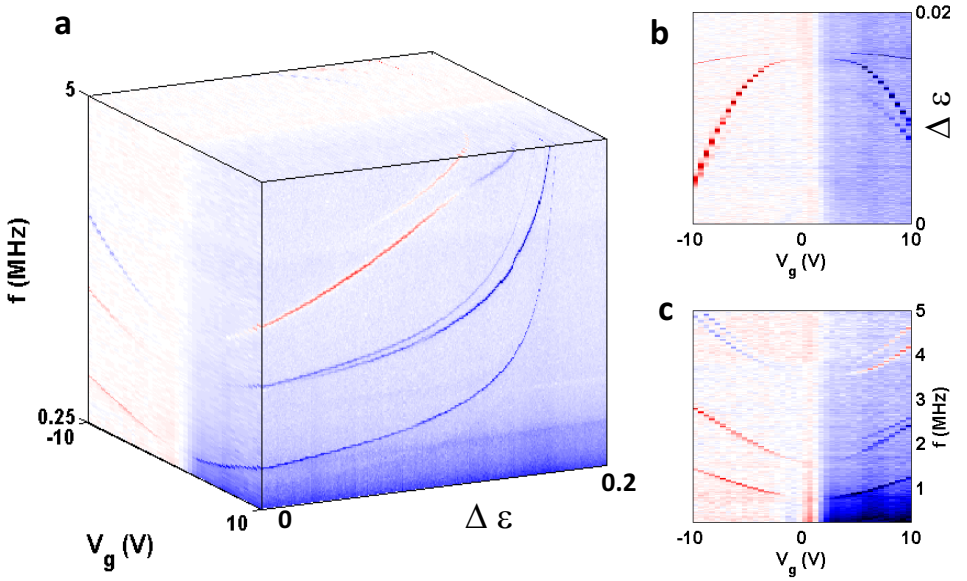

Figure 5.8: a) Complete resonance map of CNT vs. strain and gate-voltage. b) Constant frequency slice of data cube at $f = 2.5MHz$. c) Constant strain slice at $\Delta\epsilon = 0.01$.

5.7.3 Frequency-strain maps

While measuring the resonance spectrum in the high-tension limit provides information about the force environment, more detailed information is available by studying the CNT response to strain under minimal V_g. We plot such a map in fig. 5.9a. In the spectral map, the resonance modes start off at a relatively fixed, low-frequency, and remain nearly constant and then as the slack is removed the frequencies quickly increase. In the idealized case of a perfectly symmetrically clamped beam, such a frequency-strain map would experience a Euler-buckling transition, where the frequencies

drop to zero, which is clearly not true for this CNT. This behavior can arise from one of two scenarios. If the CNT is soft enough, it will behave as a semiflexible polymer, and experience entropic tension over a large range of strain. Alternatively, the CNT is attached to the tweezers with symmetry-breaking clamping conditions, where stretching the CNT smoothly pulls out the built-in bend. In the device studied in Fig. 5.9, the 2nd case is most likely true. In the subsequent analysis, we will show that the emergent Q can be understood independent of the f vs. ϵ origin.

Accessing the new dimension of strain with our tweezers, we seek to measure and understand the quality factor. In order to make an accurate measurement, we focus down on a single resonance mode and perform narrow frequency sweeps, using an adaptive algorithm to trace the resonance frequency during the measurement. The trace is shown in fig. 5.9b, where the dominant coloration has to do with the capacitive background signal. From these data, we extract the resonance linewidth, shown in fig. 5.9d, and from that extract the quality factor, shown in 5.9c. There is an interesting Q saturation behavior, which we explain next.

5.7.4 Predicting quality factor from frequency-strain map

Chapter 2 dealt extensively with explaining how thermal population of resonance modes in a CNT resonator leads to fluctuation broadening. It focused on both the tensioned and buckled cases of a symmetrically clamped CNT, neither of which fully applies to our experimental conditions, but the formalism describing how strain fluctuations lead to frequency fluctuations should still hold. In specific, the quality factor is determined by the relationship $Q = \frac{f}{\delta f}$ where $\delta f = \sqrt{8\ln(2)}\left|\frac{\partial f}{\partial \epsilon}\right|\sigma_\epsilon$. Our generalized version for Q is thus:

$$Q = \frac{f}{\sqrt{8\ln(2)}\left|\frac{\partial f}{\partial \epsilon}\right|\sigma_\epsilon} \tag{5.7}$$

remembering that σ_ϵ is theoretically calculated in eqn. 2.12. By virtue of our measurement geometry, we have directly measured $f(\epsilon)$ and thus can numerically compute $\left|\frac{\partial f}{\partial \epsilon}\right|$, indicating that all

quantities of eqn. 5.7 are directly measured, with the exception of σ_ϵ. So, rearranging eqn. 5.7, we get:

$$\sigma_\epsilon = \frac{\delta f}{\sqrt{8\ln(2)}\left|\frac{\partial f}{\partial \epsilon}\right|} \tag{5.8}$$

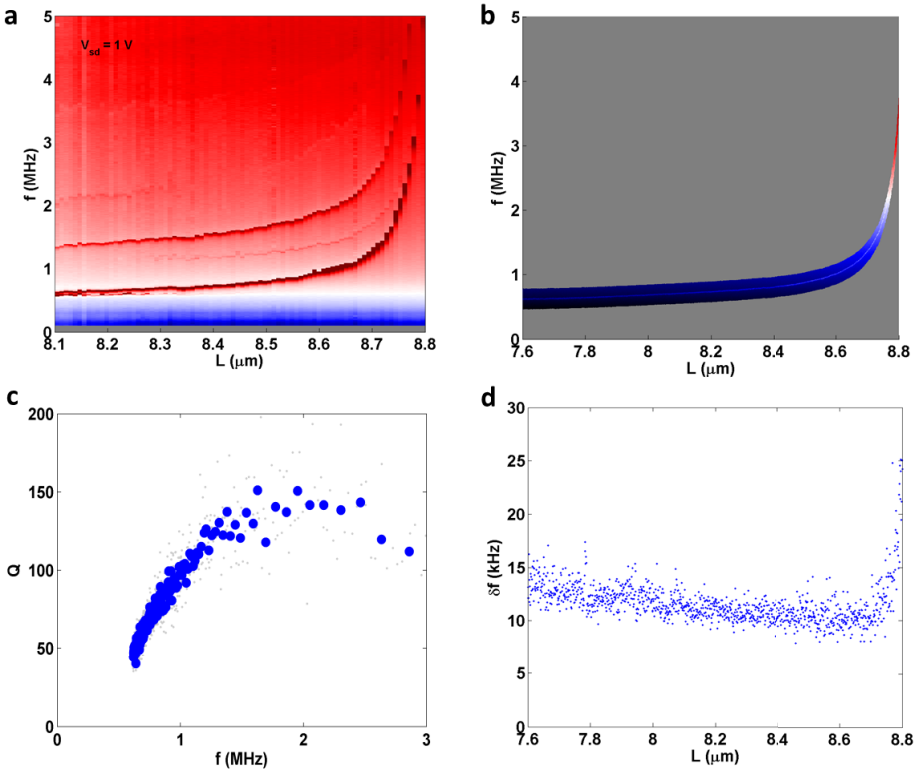

Figure 5.9: a) Spectral map of CNT being tensioned by tweezer separation. At large negative strain the resonances are bending dominated and f varies slowly, at small negative strains f varies quickly. b) Narrow measurement window tracked around lowest resonance to extract Q by measuring $\delta_{FWHM} f$. d)δf vs. strain. c) Q vs. f extracted from data in (b). Raw data is plotted in grey dots, and for clarity, data binned and averaged in groups of 5 is plotted in blue.

We perform this calculation on data from fig. 5.9 and plot it in fig. 5.10. As expected, the strain fluctuations diminish as the CNT is tensioned. We then numerically calculate σ_ϵ from eqn 1.12 using CNT diameter and mass loading as free parameters, as the length was measured well. The extracted parameters are $d_{tube} = 2.5nm$ and the CNT has a mass exceeding the pristine mass by 25%. The red line in fig. 5.10 corresponds to these values and reproduces the measured data well, particularly in the high-frequency limit.

Eqn. 5.8 also predicts the qualitative behavior seen in fig. 5.5c. In the tensioned limit, eqn. 5.6 shows that $\epsilon \sim V_g^4$, and it can be shown that $f \sim \frac{V_g}{\epsilon^{1/4}}$. From these two expressions we can determine the power-law for $\frac{\partial f}{\partial \epsilon} \sim -\frac{V_g}{\epsilon^{5/4}}$. Carrying out the algebra and substituting for V_g, we find that $\frac{\partial f}{\partial \epsilon} \sim \frac{f}{\epsilon}$. Finally, taking the relationship $\sigma_\epsilon \sim \epsilon^{3/2}$ we find $Q \sim f^{1/2}$. We qualitatively observe such sublinear behavior in fig. 5.5c, and the high-frequency limit appears $\sim f^{1/2}$ though a greater frequency range would prove valuable.

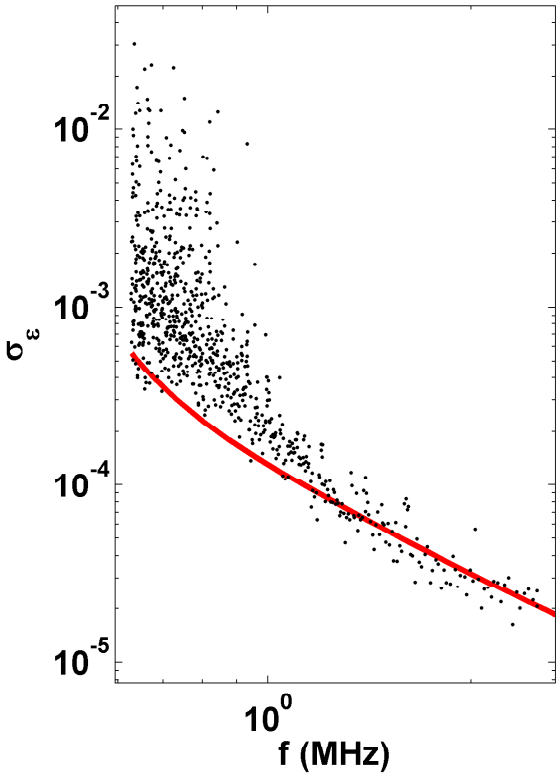

Figure 5.10: RMS strain noise as calculated from eqn. 5.8 plotted in black circles. A piece-wise fitting function is used on $f(\epsilon)$ to compute $\frac{\partial f}{\partial \epsilon}$. Red line is a theoretical calculation of σ_ϵ from eqn. 1.12 for a $2.5nm$ diameter, $8.8\mu m$ CNT with 25% mass loading; all within reasonable bounds for the CNTs being measured.

5.8 Separation of timescales: dissipation vs. spectral drift

We have shown that transverse thermal fluctuations on CNTs leads length fluctuations, and this necessarily causes spectral broadening. There remains an open question, however, as to whether

this broadening manifests itself as a slow varying tension inducing spectral drift, or whether this broadening constitutes true damping. The work in Chapter 2 studied the thermodynamics and not the kinetics of a thermally vibrating CNT, so it alone does not indicate which applies. As we saw in fig. 5.5, the latter seems true at least some of the time, however we show below two measurements that suggest that conditions arise where the energy decay rate of a resonance mode can decouple from its apparent linewidth. In the experiment shown in fig. 5.11, we directly compare the ring down time to the thermal correlation time. In this measurement, a particularly long CNT ($70\mu m$) is used, and the cryostat is cooled to 77 K. Then we iteratively perform ringdown measurements and record thermal time-traces as we increase the strain. The ringdown measurements are fit, as described before, and the auto-correlation of the thermal resonances are numerically computed, where $g(\tau) = \int x(t)x(t+\tau)dt / \int x(t)^2 dt$ is the auto-correlation function. From these fits a quality factor is calculated: $Q = \pi f \tau$.

The ringdown Qs (in red) have a sublinear frequency dependence, with the exception of a major dip near $1.3MHz$. This dip a likely due to a particular resonance condition where the primary resonance mode is strongly coupled with another, and thus energy decays out of the primary resonance mode. With the thermal Qs there is much more scatter, but the high-frequency limit shows them to be a factor of two less than the ringdown Qs.

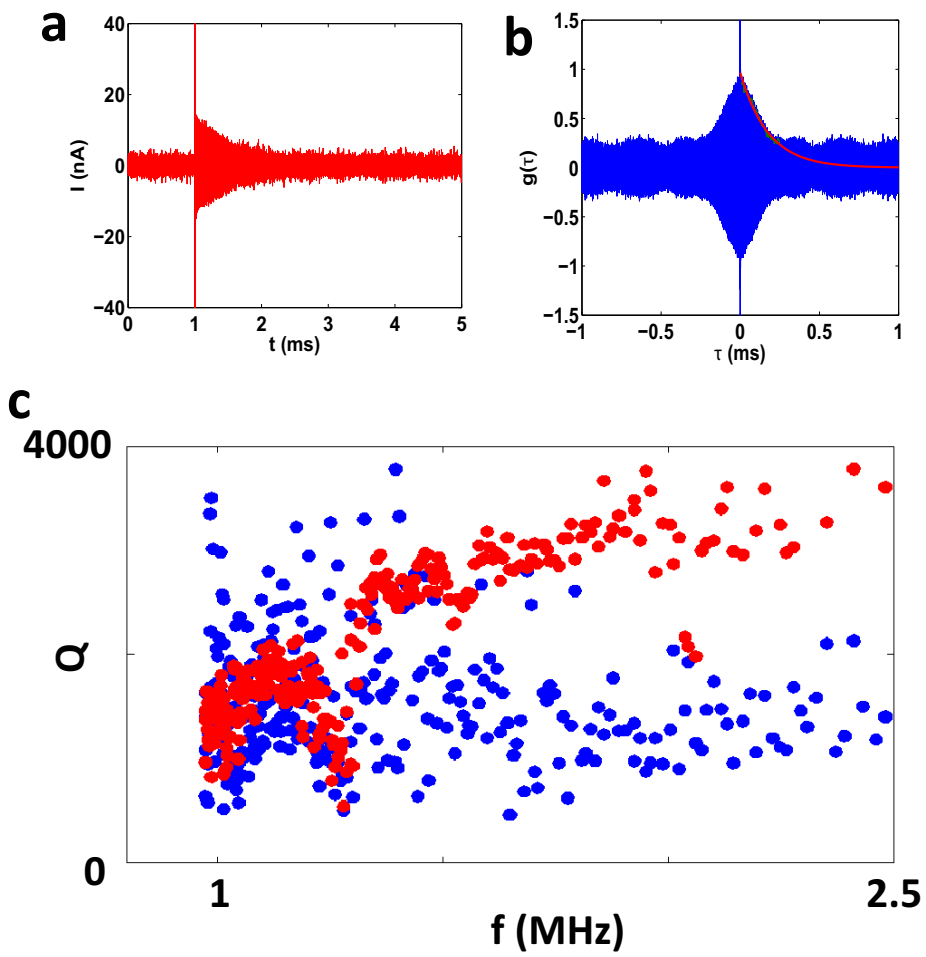

Figure 5.11: Separation of timescales. a) Ringdown trace from a $70\mu m$ long, $7nm$ diameter CNT. b) auto-correlation of thermal resonance time trace. A fit is performed on $g(\tau)$ in the vicinity of $\tau = 0$ to extract the correlation time. The relaxation time from (a) and correlation time from (b) are converted into $Q = \pi\tau f$ and plotted in (c). Red corresponds to ringdown data and blue to auto-correlation data.

Finally, we compare a thermal resonance map with ringdown measurements, and observe a separation of time-scales near an avoided crossing. Starting with a resonance map of the thermal fluctuations of a CNT as tuned by V_g (fig 5.12a), we measure Lorentzian linewidths of the particular mode highlighted in fig. 5.12a and extract the quality factor, plotted as blue in fig. 5.12b. As can be seen, there are some gaps in the resonance spectrum near $V_g = 1V$, and there are likewise gaps in the measured Q. Similarly, we perform ringdown measurements after the resonance thermal resonance map is obtained and extract Q as above. These data are plotted in fig. 5.12b in red with similar gaps

visible. Albeit sparse, the low frequency data seem to agree between the measurement techniques, however, in the the high-frequency data near $f = 1MHz$, they separate. This separation occurs directly in the vicinity of an avoided crossing highlighted in fig. 5.12a.

In this scenario, the avoided crossing apparently introduces phase noise, but does not serve as an appreciable dissipation source. As touched upon in Chapter 2, the splitting at certain avoided crossings is amplitude dependent, so amplitude noise in one resonance mode can induce phase noise in another.

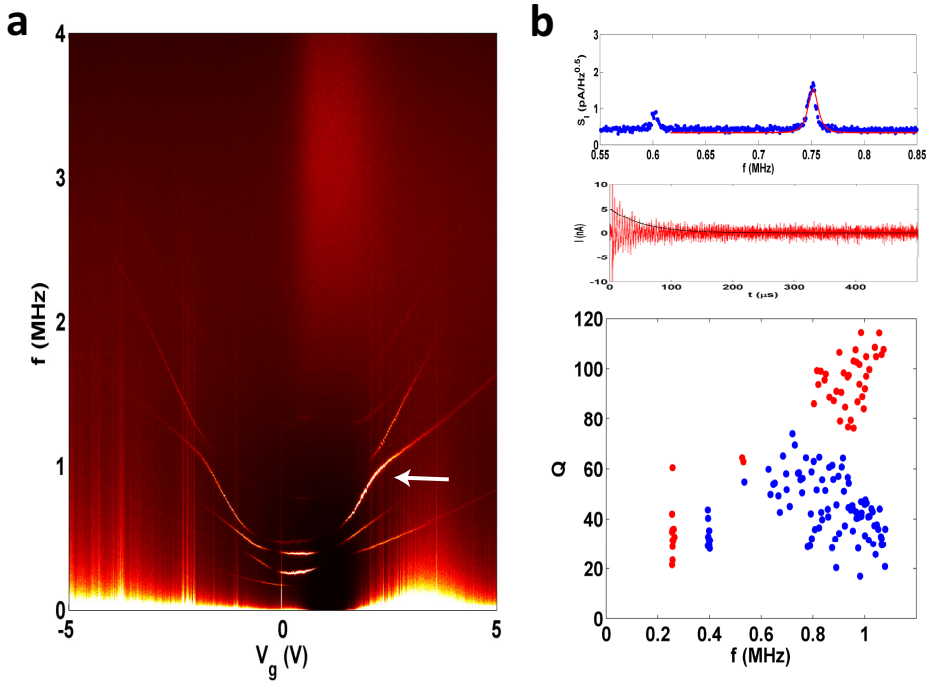

Figure 5.12: Separation of timescale at avoided crossing. a) Thermal PSD map of resonances as a function of V_g revealing many resonance modes and avoided crossing. b) top: thermal resonance spectrum with Lorentzian fit. middle: ringdown measurement with associated fit line. bottom: Quality factors measured by thermal linewidths (blue) and ringdown relaxation time (red). These data correspond to the resonance mode labeled with an arrow in (a)

5.9 Conclusions

In this chapter we surveyed the variety of methods and measurements we employed to study the effects of fluctuation broadening on the resonance properties of CNT resonators. We developed techniques around our microtweezer platform, to accurately strain and measure the vibrational

properties of doubly-clamped CNT resonators. In the process we demonstrated the first-ever room temperature thermal measurement of a single-CNT resonator, and we performed the first-ever ringdown measurements on CNT resonators. Using this tool set, we found that the work we discussed in chapter 2 can be generalized and applied to non-trivial geometries, so long as the frequency-strain dependence can be measured or inferred. Finally, we showed how fluctuation broadening can act as a damping mechanism when thermal amplitudes are large, and as a source of phase noise when the amplitudes are low.

The extraordinarily soft spring constant and low mass of CNTs is the feature that makes them scientifically fascinating and as we show, makes thems a testbed of truly nanoscopic physics. In the following chapter, we enter into the field of optomechanics, coupling CNTs to light in order to better study CNT properties and to explore their use in technologically novel applications.

Chapter 6

CNT-based Cavity Optomechanics

6.1 Introduction

The same properties that make CNTs unique in the realm of NEMS makes them an attractive candidate to be applied in the emergent field of cavity optomechanics [28,30]. Cavity optomechanics, at its most basic level, is the coupling of the light field in a resonant optical cavity to the displacement of a mechanical resonator. The consequences of this coupling, however, can be dramatic and thus has been the basis of intense research over the past decade. Cavity-optomechanical systems are beginning to show promise in topics spanning from quantum metrology, and quantum computation to technological applications such as on-chip optical modulators and sensors. Improvements in nanofabrication and laser technology catalyzed many of these new developments, as miniaturization of high-Q optical cavities dramatically enhances the light-matter interaction.

In particular, there has been marked interest in coupling CNTs with high-finesse cavities, because of CNTs unique mechanical and optical properties. The extreme softness to bending coupled with the low-mass means that CNTs will respond quickly and dramatically to small radiation pressure forces, while their non-trivial dielectric function [52, 55] suggests that their optomechanical coupling can be resonantly enhanced. Further, they are an ideal candidate for the nascent subfield of *dissipative* optomechanics [27, 64], which promises to offer enhanced optical cooling and detection of mechanical motion. Due to the inherently small size of CNTs, however, it is a technically

challenging feat to position a CNT in a cavity properly so as to maximize optomechanical coupling while not significantly degrading the optical-Q. Initial work has reported optical coupling of CNTs to low-Q Silicon microdisk resontators [65], as well as optomechanical coupling of CNT bundles into waveguide Fabry-Perot resonators [66], but to date, there are no reports of single CNT resonators coupling into optical cavities. In this chapter, we detail our work combining our micro-tweezer technology with optical microdisk resonators in collaboration with Prof. Michal Lipsons research group in order to readily couple single CNTs to high-finesse microdisk cavities.

Experimentally, we use the CNT to study the microdisk field, we use the microdisk to probe the CNT optical properties, and finally we demonstrate the first observed optomechanical coupling of a single CNT in an optical cavity.

6.2 Optical microdisk resonators

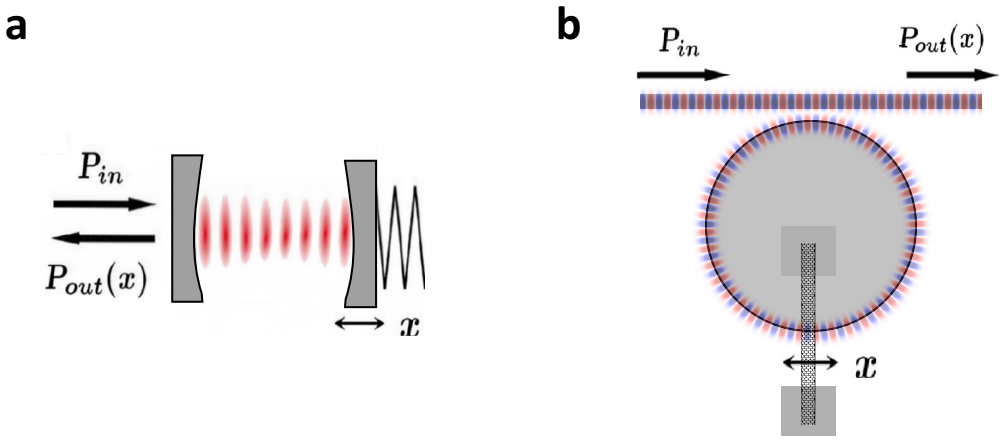

Figure 6.1: a) The canonical optomechanical system: a Fabry-Perot cavity, with a spring-mounted mirror. Both the cavity and the vibrating mirror-spring system have independent frequencies and quality factor; yet radiation pressure imparts force on the mirror, and the mirror position modifies the optical cavity frequency. b) the analogous system that we study. an optical microdisk resonator is pumped by an evanescently coupled tapered fiber. On the other end, a CNT serves as the resonant mechanical element. The CNT can modify the effective index of the cavity or it can act as an additional dampping mechanism.

Optical microdisk resonators are, in the simplest terms, light-confining circular disks formed out of a dielectric medium. Based on the principle of total internal reflection (TIR), these resonators

can confine light that travels along their edge, much as a waveguide can confine and guide light along its axis. Unlike a simple waveguide, the closed geometry of a microdisk forces light traveling along its edge to wrap around and interfere with itself, creating conditions for steady-state optical resonance modes called whispering gallery modes (WGM). Based on the symmetry of microdisks, there are always two possible counter-propagating modes for a given mode number. There are many WGMs supported in a single cavity, with a series of frequencies $\omega_m \approx m\frac{c}{nd}$ where c is the speed of light, n is the effective refractive index and d is effective cavity diameter. The difference between respective modes is commonly referred to as the free spectral range $\Delta\omega_{FSR} = \frac{c}{nd}$, which is inversely related to the round-trip time ($2\pi\Delta\omega_{FSR} = T_{RT}^{-1}$). All optical cavities have a photon loss rate γ which is frequently expressed in two dimensionless quantities: the finesse $\mathcal{F} \equiv \frac{\Delta\omega_{FSR}}{\gamma}$ characterizes how many times a photon circulates around the cavity before decaying, and the quality factor $Q \equiv \frac{\omega}{\gamma}$ characterize how may periods of oscillation a photon undergoes before decaying (analogous to the mechanical Q).

In order to populate these resonance modes, light is typically coupled-in evanescently from a nearby optical waveguide (see fig. 6.1b). The strength of the coupling is set by the separation between the waveguide and the cavity, much as the coupling between a free propagating wave and a Fabry-Perot cavity are set by the reflectance of the input mirror. In the waveguide-coupled microdisk cavity, the fate of an input photon depends on the coupling: the photon can pass through the waveguide unimpeded under low-coupling, it can scatter into the cavity, circulate and be absorbed or lost to the surrounding environment under moderate coupling, or it can scatter into the cavity, circulate and re-scatter back into the waveguide under strong-coupling.

Although there is a full quantum formalism based on input-output theory for open quantum systems that correctly describes this system, we will focus on summarizing the above discussion in classical terms as all of our experiments reside well out of the quantum regime. In steady state, the system is characterized by the input laser frequency ω_L, the input power P_{in}, the energy stored

in the cavity E_{cav} and the transmitted power P_{out}. The relationship among these quantities is set by the cavity resonance frequency ω_{cav}, the coupling rate γ_{ex}, and the intrinsic loss rate γ_0. The energy stored in the cavity becomes:

$$E_{cav} = \frac{\gamma_{ex}}{\Delta^2 + (\gamma/2)^2} P_{in} \tag{6.1}$$

where the detuning is $\Delta = \omega_L - \omega_{cav}$ and the total loss-rate is $\gamma = \gamma_0 + \gamma_{ex}$. The output power is:

$$P_{out} = P_{in} - E_{cav}\gamma_0. \tag{6.2}$$

Focusing on-resonance ($\Delta = 0$) we can see the importance of the coupling rate. If the coupling rate is small compared with the damping rate ($\gamma_{ex} \ll \gamma_0$) in the so-called under-coupled condition, then $E_{cav} \propto \gamma_{ex}/\gamma_0^2$. The rate at which power flows into the cavity is proportional to γ_{ex}/γ_0 and all of this power is dissipated in the cavity. A potentially counter-intuitive reality about this condition is that increasing γ_0 actually *decreases* the total power dissipated by the cavity. In the critical coupling condition where $\gamma_{ex} = \gamma_0$ all power enters the cavity and gets entirely dissipated ($P_{out} = 0$). Finally, in the over-coupled condition ($\gamma_{ex} \gg \gamma_0$), the power dissipated in the cavity is proportional to γ_0/γ_{ex}. Here, increasing coupling leads to less power dissipation as photons are more able to escape the cavity before dissipating inside the cavity.

6.3 Cavity optomechanics

Cavity optomechanics arises when some component of a cavity system is no longer fixed in space but can deflect and modify the cavity, while the circulating light in the cavity can apply forces to that same component. In the canonical example of a Fabry-Perot cavity with one mirror mounted on a spring, a change of mirror position modifies ω_{cav} which changes the equilibrium E_{cav} in eqn. 6.1 and thus changes the $F_{opt} \propto E_{cav}$. This is called the optical spring effect, because the net influence of the light field is to modify the spring constant of the mechanical spring. More generally speaking, the mechanical element need-not modify the cavity frequency but may instead modify the loss rate,

and furthermore, the coupling between the optical and mechanical system can be a dynamical process.

The full system is characterized by two coupled differential equations:

$$\dot{a} = i\Delta a - \frac{\gamma}{2}a + i\sqrt{\gamma_{ex}}s \tag{6.3}$$

and

$$\ddot{x} + \frac{\gamma_m}{2}\dot{x} + \Omega_m^2 x = \frac{F_{opt}}{m_{eff}} + \frac{F_L}{m_{eff}} \tag{6.4}$$

where a is a normalized complex electric field amplitude, $s \cdot \sqrt{\omega_L}$ is a normalized complex input electric field amplitude, F_{opt} is the optical force experienced by the mechanical element and F_L is the Langevin force. The normalization conditions are $\epsilon_0 V_{cav}|a|^2 = E_{cav}$ and $\epsilon_0 V_{cav}|s|^2 = P_{in}$. The possible couplings between eqns. 6.3 and 6.4 are diverse. Depending on the physical system, any of the nominally constant coefficients in eqns. 6.3 and 6.4 may become functions of either of the two dynamical variables. When the cavity lifetime is short compared to the mechanical resonance frequency ($\gamma \ll \Omega_m$) the cavity response is quasi-static leading to the optical spring effect. When the cavity lifetime approaches and exceeds the mechanical resonance frequency ($\gamma \gtrsim \Omega_m$) non-trivial dynamics emerge, leading for example, to parametric amplification or optical cooling of the mechanical mode.

6.4 Measurement set-up

Our optical measurements focused on interacting a tweezer-held CNT with the evanescent field of a fiber-coupled Si_3N_4 microdisk optical resonator. For this, microdisk cavity chips are mounted on the sample stage alongside the CNT source substrate in the cryostat that was detailed in Ch 4. On the auxiliary attocube piezo cube, a tapered optical fiber is mounted with planar fork. This allows operational control over the fiber-cavity coupling. As diagrammed in fig. 6.2a, a tunable, fiber-coupled, telecom laser serves as a coherent light source. The light passes through an attenuator and

polarization controller, through the tapered fiber, interacts with the cavity, and finally is collected in either a Germanium or InGaAs photodiode. The tweezer set-up remains identical to the work discussed in the previous chapter, with the only modification being that the cavity chip is electrically contacted from behind to serve as a global back-gate. The optical fiber evanescently couples into a whispering gallery mode (WGM) resonance, schematically rendered in fig. 6.2b, which consists of circulating light along the perimeter of the cavity. The WGM has its own evanescent field that can couple with external objects such as a CNT.

The measured signature for a cavity resonance is generally a Lorentzian dip in the transmission spectrum as recorded by the photodiode (P_{out} from eqn. 6.2). As discussed above and shown in fig. 6.2c, this is due to light being absorbed or scattered out of the cavity. The depth of the trough is set by the relative impedance matching between the fiber-cavity coupling and the intrinsic cavity loss rate and the width of the resonance is set by the total cavity loss rate.

6.4.1 Tapered fiber fabrication

We use tapered optical fibers to couple lasers in to the micro-optical cavities. A tapered optical fiber is an uncladded thin optical fiber that has a similar dimension to an integrated waveguide. The light passing through the thin region of a tapered optical fiber has a broad evanescent field which can interact with micro-optical devices. The advantage of using these fibers is the ability to tune optical coupling strength and easily access many on a single chip.

We use a home-built fiber pulling station to create tapered optical fibers. The pulling is achieved by simultaneously heating and pulling a small region of an uncladded fiber. We strip the fiber cladding (Corning SMF28e) in a small region of an intact fiber ($\sim$ 2 cm) and clean the the area with IPA. The fiber is then held taught between two commercial fiber clamps, which sit on two motorized stages so they could move in opposite directions. The heating is provided by a small butane flame delivered through a needle mounted on a third motorized stage. We mix butane and oxygen with two flow controllers so that the flame could reach $\sim$ 1800C where the fiber glass

becomes soft. The flame is repetitively scanned along the fiber as the clamps are slowly pulled apart to create an adiabatic transition of the optical fiber. We pass a 1550 nm laser through the fiber as we heat and pull the fiber. The net fiber transmission is continuously monitored with a photodiode.

The fiber changes from single mode to multi-mode and back to single mode as it is pulled. This creates an oscillating transmission at the output as the fiber goes through different modes. Once the fiber reaches the final single-mode diameter, which is $\sim 1\mu m$ for 1550 nm, the transmission becomes independent of the taper length. We monitor the pattern in the transmission by monitoring the derivative of the transmission. Once we detect the derivative to fall below a threshold value, the pulling is stopped and the torch retreats.

The flame size we use is approximately 1 mm in diameter and the scanning length is $\sim$ 10 mm. This results in tapered fiber $\sim$ 20 mm long and losses around 1 dB.

Finally the tapered fiber is further stretched by 50 μm at room temperature to create extra tension in the fiber in order to minimize fiber vibrations. The fiber is then glued to the holder 'fork' and the ends of the fiber are connectorized to attach into the cryostat.

6.4.2 Optical cavity fabrication

We fabricated optical cavities using standard single-side polished silicon wafers with a thermal oxide layer ($\sim 3.5\mu$ m). A stoichiometric silicon nitride layer ($\sim 320nm$) is deposited using low pressure chemical vapour deposition (LPCVD)technique. Cavities of varying diameters ($25\mu m - 100\mu m$) are patterned using e-beam lithography. Next to each cavity, a fiber 'parking-lot' is also patterned (see fig. 2a) as a means of mechanically stabilizing the tapered fiber. The pattern is transferred on to the wafer using reactive ion etching (RIE) with CF_4. Using CF_4 as oppose to CHF_3/O_2 lowers possible fluorocarbon polymer formations at the cost of resist selectivity and side-wall angles. The patterned wafer is cleaned in a freshly mixed piranha (H_2O_2:H_2SO_4) solution for 20 minutes and in a standard MOS clean process (10 minutes dilute NH_4OH/H_2O_2 and 10 minutes dilute HCL/H_2O_2).

The wafer is then further cladded with ∼50 nm of high temperature oxide (HTO). The HTO layer protects the uncladded cavity from contamination in further processing steps. The wafer is then annealed at 1200C for 2 hours to reduce hydrogen dangling bond in the nitride layer which induces absorption of light.

At this stage, the cavity wafers are diced into narrow dies ($\sim 1.5mm$) which reduces the constraints for planarizing with respect to the tapered fiber. The optical cavities are released by etching the oxide in diluted hydrofluoric acid (49% HF:H_2O 1:6) for 30 mins to remove approximately $3\mu m$ of oxide. The releasing ensures a symmetric optical mode profile which promotes high optical quality factor and more evanescent field on the top of the cavities. Subsequent processing was sometimes used to enhance optical quality factors. Specifically, hot piranha cleaning, high temperature hydrogen annealing, and HF dipping were used in various permutations. Piranha serves to remove organics, hydrogen annealing to remove absorptive 2-level systems from the bulk nitride, and HF dipping to strip the native oxide layer.

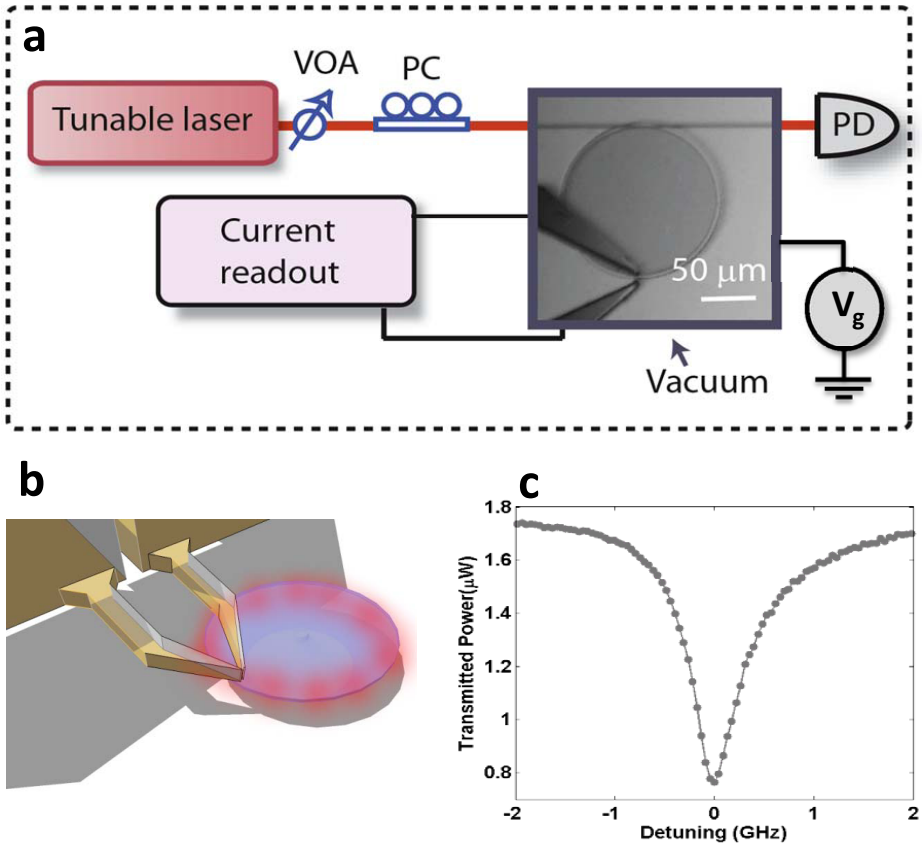

Figure 6.2: a) Schematic of optomechanical cavity apparatus. The CNT-tweezers are opperated in the vicinity of a Si_3N_4 optical microdisk resonator (visibile in the inset optical micrograph). Light is evanescently coupled into the microdisk with a tapered optical fiber, seen tagent to the microdisk in the optical micrograph. The fiber is fed by a telecom (1550-1650nm) fiber-coupled laser with a variable optical attenuator (VOA) and polarization controller (PC). The output laser light is collected by a a photodiode (PD) and used to measure optical resonance. Electrical contact is made to the back-side of the microdisk chip in order to apply a gate voltage (V_g) for apply electrostatic forces to the CNT. b) Schematic of device geometry: light occupying a whispering-gallery-mode (WGM) of the cavity interacting with a tweezer-held CNT. c) Example of a measured PD signal when tunning the laser through a cavity resonance. The cavity power drops when in resonance as light is scatter or absorbed in the cavity.

6.5 Measuring cavity response to CNT

Using a tweezer-spanning CNT, we measure the response of an undercoupled high-finesse cavity ($\mathcal{F} \sim 2,000$) as a function of CNT position. Specifically, we position the tweezer over the edge of a $30\mu m$ diameter cavity (fig. 6.3a) and sweep across a cavity resonance as the tweezers are incrementally lowered into contact with the cavity. We plot the bare cavity resonance as well as the CNT-contacted cavity resonance in fig 6.3. As can be seen, the cavity resonance broadens

and the maximum extinction (trough depth) decreases with the CNT on the cavity surface. These observations are consistent with the CNT modifying γ_0 of the cavity and the cavity being under-coupled. From the cavity linewidths, we measure a value of $\gamma_{cnt} = \gamma_{final} - \gamma_{initial} = 500MHz$ and can determine that the CNT either absorbing or scattering $250nW$ of power from the cavity, which is $1/7^{th}$ of the launched laser power. The cavity enhancement is clearly evident here.

From the z-series of optical spectra, we plot data in a surface plot angled in such a way as to highlight the extinction vs. displacement in fig. 6.3c. As is evident, the extinction changed exponentially until the CNT made contact with the cavity. In fact, the $0nm$ label was experimentally inferred from the apparent flat region in the extinction vs. height. An exponential fit to the positive-z region of the extinction reveals a characteristic length of 120 nm. This serves two purposes. First it demonstrates the ability to use a CNT to map the evanescent field of the optical cavity, and second, it allows us to extract a theoretical maximum dissipative $g_{OM} = d\gamma/dz$. In this system, $g_{OM} = 4MHz/nm$. Finally, in more experimental terms, we can recast this as a maximum position sensitivity of $d\ln(P_{out})/dz = 0.002nm^{-1}$.

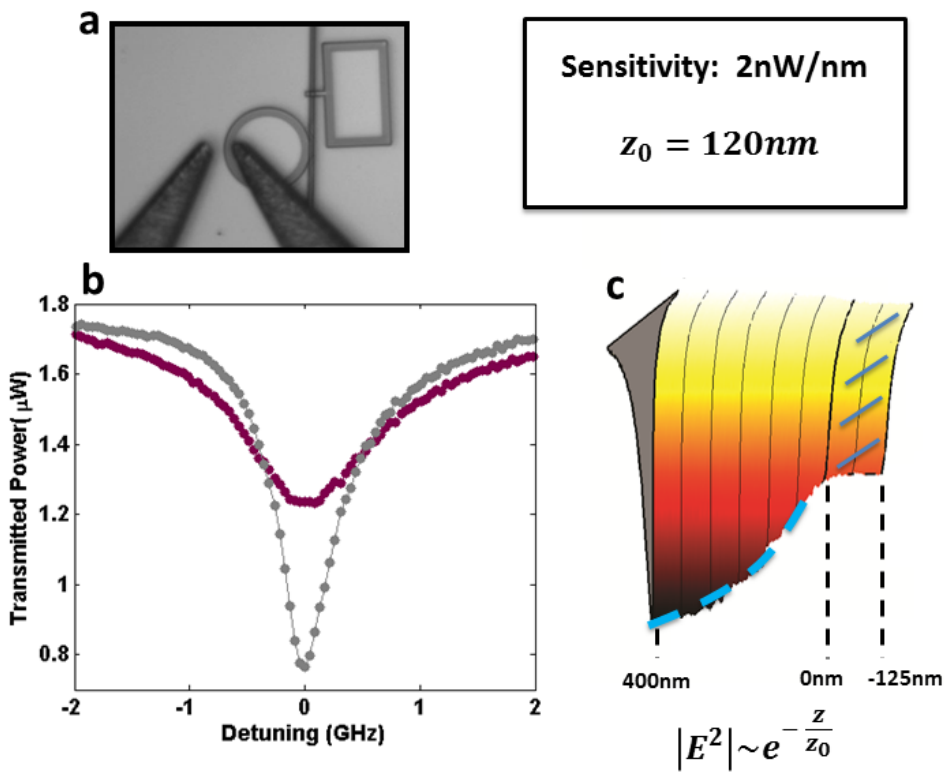

Figure 6.3: a) Optical micrograph of high-finnesse cavity (diameter is $30\mu m$). There is a $2\mu m$ wide nitride tab near the cavity which is used to stabilize the tapered fiber. b) optical trassmission spectrum of bare cavity resonance (grey) and cavity resonance with CNT touching cavity (purple). c) Surface plot made of optical spectrum as a function of separation between CNT and cavity. Experimentally, only relative displacements are known, but the CNT contacted the cavity, so the absolute separation is inferred from the apparent saturation in damping. An exponential fit to the resonance height effectively maps the evaescent field of the optical mode, and provides a maximum coupling rate.

6.6 Photocurrent mapping of cavity field

Drawing from the observation in the previous section that the CNT can map the evanescent field of an optical cavity by modifying its transmission, we demonstrate here the use of the nanotube in mapping the cavity field via photocurrent. For this measurement, we work with a high finesse cavity $\mathcal{F} \sim 3,000$. Beyond having a higher finesse than the previously discussed cavity, this cavity has a marked degeneracy splitting as seen in the top panel in fig. 6.4a. The splitting originates from fabrication inhomogeneities that break the rotational symmetry of the cavity. This leads to standing wave eigenmodes where the frequency splitting corresponds to the effective path length

difference between the resonance modes.

With this understanding, we position the CNT in the evanescent field of the cavity and measure optical transmission spectra while simultaneously collecting photocurrent as shown in fig 6.4a. With the CNT arbitrarily placed relative to the cavity, there are photocurrent peaks with differing signal strengths corresponding to each optical resonance. Then, by scanning the CNT position along the y-axis (inset fig. 6.2a), we simultaneously collect transmission and photocurrent spectra. These data are plotted in color-maps in fig. 6.4b and 6.4d. The photocurrent signal in fig. 6.4b reveals clear, periodic structure for each optical resonance, while the optical transmission seems unperturbed. We analyze these data by fitting Lorentzians to both resonances in both sets of data as a function of CNT position. While the Lorentzian width remains constant within experimental bounds, the amplitudes vary significantly for the photocurrent, and marginally for the transmission spectra. The Lorentzian peak heights from fig 6.4b and 6.4d are plotted in fig. 6.4c and 6.4e respectively. In these plots, the blue dots correspond to the higher frequency mode. The fits in fig 6.4c. show photocurrent peaks of $\sim 200pA$ high and a periodicity of $400nm$. The periodicity is consistent with a standing wave formed by $1,600nm$ light slowed down by a refractive index of $n = 1.98$. On the contrary, the optical transmission signal appears very constant with minimal apparent correlation to the photocurrent signal.

Taking the standard deviation of the data in fig. 6.4e as an upper bound on the extinction, we can compute a lower bound on the photon collection efficiency of the CNT field detector. With a width of $\sigma_P \sim 10nW$, and the significant under-coupling in the system, we can directly predict that the power dissipated by the CNT is also $\sim 10nW$. This corresponds to a dissipated photon flux of $8 \times 10^{10} s^{-1}$. With a current of $200pA$, this gives a minimum conversion efficiency of $0.02 e^-/photon$.

These data show that a scanning CNT photocurrent sensor can serve to map optical fields with high spatial resolution. In contrast to optical transmission mapping, this technique is not subtractive, so does not require high dynamic range to extract meaningful small signals.

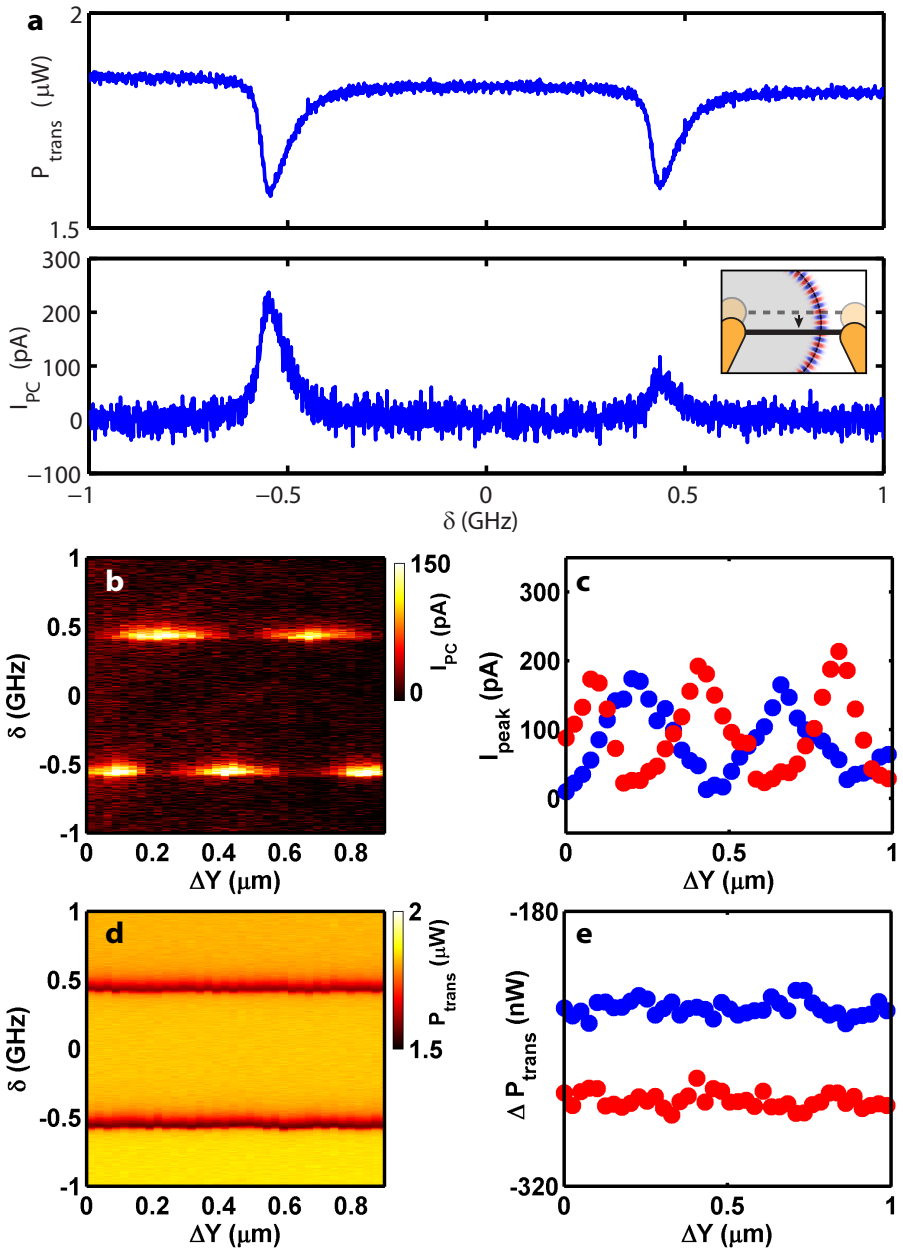

Figure 6.4: Mapping cavity field with photocurrent. a) Transmitted power (P_{trans}) and photocurrent signal (I_{PC}) vs. laser frequency. Inhomegenaties in the cavity fabrication lead to backscattering which sets up two non-degenerate standing wave modes. $\delta = 0$ is chosen to be between these cavity modes. Inset: diagram of experiment performed. CNT is moved across the standing wave nodes while measuring I_{PC} and P_{trans}. The CNT is held in the far field of the cavity, and minimally purturbs the intrinsic damping of the cavity. In (b) and (d), the I_{PC} and P_{trans} spectra are plotted as a function of the tweezer position. (c) and (e) show peak heights the measured modes from Lorentzian fits of the signals in (b) and (d) respectively. Red corresponds to the lower frequency mode and blue the higher frequency mode.

6.7 Measuring CNT optical polarizibility

One of the attractive applications of optical ring resonators is their ability to sensitively detect small objects. J. Zhu *et.al.* [67] first demonstrated that nanoparticles adhered to micro-toroid optical cavities could be properly sized based on their polarizability irrespective of where the nanoparticle contacted the resonator. In these measurements, cavities started with degenerate modes, and the particle induced a splitting, as well as imposed additional damping. The polarizability can be directly measured from the ratio of the frequency splitting δ_{split} to the additional damping $\gamma_{scatter}$:

$$\alpha = -\frac{3\epsilon_0\lambda^3}{2\pi}\frac{\gamma_{scatter}}{\delta_{split}} \tag{6.5}$$

which is independent of location. This analysis, however presumes purely dispersive interactions; Rayleigh scattering will scatter light into the environment or back into the cavity and the relative rates are set by the polarizability. More generally, however, an object may have its own intrinsic absorption rate, which will serve to further broaden a resonance without leading to frequency shifts, throwing off the conclusion from eqn. 6.5.

With our CNT-tweezer system, we have the opportunity to overcome this challenge by measuring the polarizibility of the CNT directly. Starting with the same CNT shown in the previous section, we bring the tube into contact with the cavity. This maximizes the optical coupling of the CNT to the cavity. While CNT was in contact with the cavity, drift or mechanical backlash led the cavity to move in the y-direction relative to the tweezers. Then, lifting the tweezers in the z-direction therefore causes the CNT to peel off the cavity in a diagonal fashion, as diagrammed in fig. 6.5a. This leads the CNT to cross standing-wave nodes as it separates away from the substrate. The optical transmission spectra as a function of height are shown in fig. 6.5b where the spectra are vertically spaced for clarity. As is apparent in fig. 6.5b, the resonance peaks' height, width, and frequency are cyclically modulated as the tube passes through the standing waves. We fit the resonances much as was done in the previous section, and extract the damping $\gamma_{scatter}$ and the

center frequencies δ shown in fig. 6.5c and 6.5d respectively. As the tube is peeled up in z, the damping of each respective mode is sinusoidally modulated. The peak damping rate decays with increasing height, while it plateaus between peaks at the intrinsic damping of $200MHz$. In fig. 6.5d, the resonance modes are red-shifted when the damping is high and reach a maximum when the damping is low.

$\gamma_{scatter}$ and δ are in fact linearly related, and a fit would give a polarizability of $1.8 \times 10^{-28} Fm^2$ which is orders of magnitude too high, as the effective cross-section would greatly exceed the CNT diameter. If instead we apply knowledge of the cavity field, we can extract α directly from the relationship: $g = -\frac{1}{4\pi\epsilon_0}\frac{\alpha f(r)^2 \omega_{cav}}{4\pi V_{cav}}$ provided we can determine the resonance mode profile $f(r)$ and cavity mode volume V_{cav} from our known geometry. From computational analysis, we find $f(r)^2 \sim 0.2$ averaged along the radial direction and $V_{cav} \sim 2 \times 10^{-17} m^3$. From here, the observed $200MHz$ frequency shift leads to a polarizability of $\alpha = \times 10^{-32} Fm^2$. This can be recast as a scattering cross-section $\sigma = 8\pi^3/3\epsilon_0^2\alpha^2/\lambda^4$. For our tube this gives $\sigma/L = 3 \times 10^{-11}\ m$ where L is the length of the tube interacting with the cavity, which is in order-of-magnitude agreement with on resonance optical cross sections previously reported [55]. The measured amplitude is consistent with a CNT with $d \sim 10nm$.

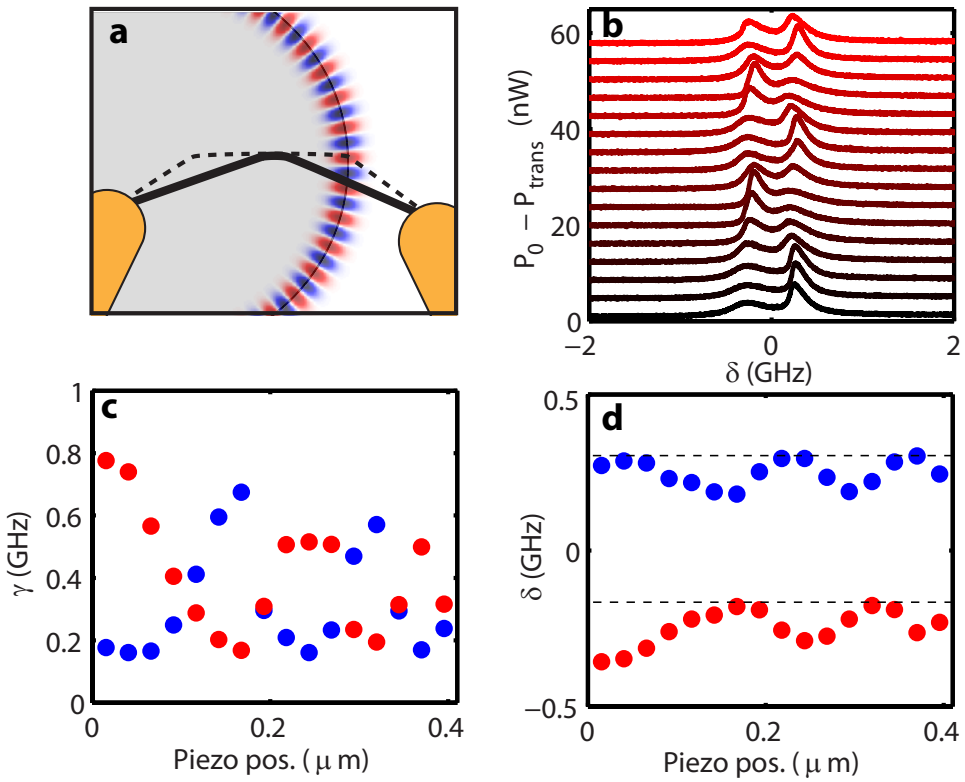

Figure 6.5: CNT polarizability measurement. With the same tube as in fig. 6.4, CNT is brought into contact with the cavity. Due to drift or mechanical backlash, the cavity moves in the y-direction relative to the tweezers before the tweezers are moved in the z-direction. a) Top-view diagram of CNT position as tweezers are lifted. The dotted line shows CNT position at low-z and the black line at high-z. b) Optical response as tweezers are lifted $400nm$. For clarity, the spectra are plotted in $P_0 - P_{trans}$ where P_0 is the maximum transmitted power ($11nW$), and each spectrum is displaced $3.8nW$ from its predecessor. Black corresponds to the lowest-z and red to the highest-z. c) cavity decay rate and d) resonance frequency as measured from Lorentzian fits to resonance peaks in (b). Data in red correspond to the lower frequency mode and blue to the higher frequency mode in both (c) and (d).

6.8 CNT optomechanics

6.8.1 Electrical driven, optically detected CNT resonator

We now move to final main topic of this chapter. In the previous sections, the CNT was used and manipulated quasi-statically in order to probe the CNT-cavity interaction. Now we return to using the CNT as a mechanical resonator, and begin to study the dynamical coupling between the resonator and cavity. First we test the use of the optical cavity as a position detector of the vibrating CNT. The laser is tuned to a high-finesse cavity mode and the CNT is moved into the

cavity field to determine if there is sufficient optomechanical coupling. Then, the gate electrode is modulated with a network analyzer to actuate the CNT capacitively. Instead of monitoring the AC conductance of the tube, the photodiode signal is read by the network analyzer. With the CNT vibrating, the tweezers are slowly lowered until mechanical resonances are observable in the network analyzer signal. The tweezers are then held in place and spectra are recorded as a function of gate voltage.

An example resonance map is shown in fig. 6.6. While the general feature of resonance modes tuning with gate voltage is similar to electrically-detected resonance maps, there is no noticeable background signal, particularly above $1MHz$. As such, higher frequency modes register nearly as clearly as low-frequency modes. Additionally, there is an apparent sign flip across a number of resonances as a function of gate voltage. This likely arises from one of two reasons: (a) the g_{om} may flip sign as the equilibrium shape of the CNT cantilever is tuned or (b) as the equilibrium shape changes, a node of the particular resonance mode crosses the WGM leading to an apparent mechanical phase flip. While we can not be certain, (b) appears to be the most likely explanation. This highlights a significant difference between our electrical and optical detection schema. With our optical detection scheme, the measurement is over a single $\sim 1\mu m$ wide region, while with the electrical detection scheme the average displacement is measured over the entire length of the tube. The narrow interaction region should aid in mapping resonance eigen-mode shape by scanning the CNT transversely.

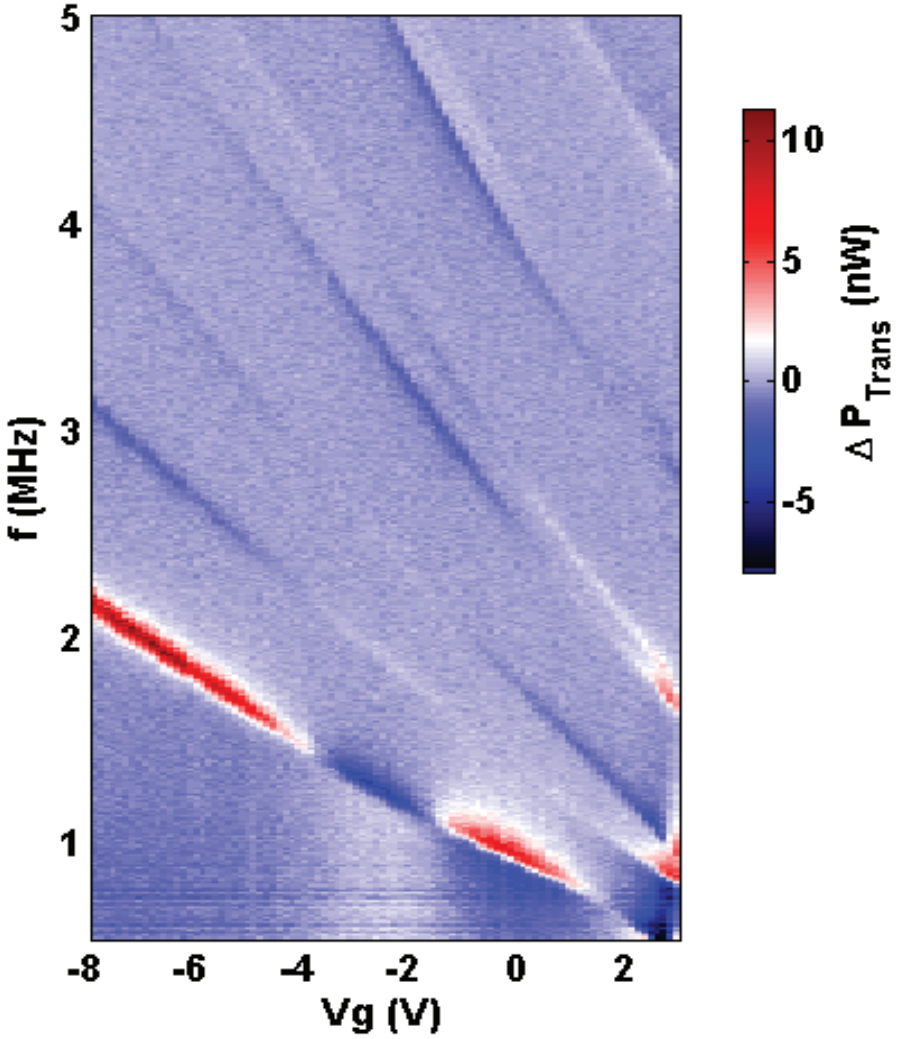

Figure 6.6: Optical detection of CNT resonance. CNT is held in the light field of the cavity, laser frequency is slightly detuned from resonance, AC gate voltage is driven with a network analyzer and optical transmission is measured with a fast photodiode. The apparent optomechanic coupling flips sign near $V_g = -2V$ and $V_g = -4V$ which may stem from spectral drift. Unlike electrical detection, there is no apparent background.

6.8.2 Improved resolution for measuring thermal resonances

Now, by turning off the drive, and tuning the CNT-cavity system to maximize g_{OM}, we measure the thermal spectrum of the CNT. Analogous to the way electrically-detected CNTs were calibrated, we first perform a z-scan to extract a value for g_{OM}. From here, the power spectrum from the photodiode is measured, and converted into the displacement power spectrum as plotted in fig.

6.7a. As can be seen, there are a total of 5 resonance modes readily measured (from $\sim 30s$ total integrate time), and the noise floor is $30pm/\sqrt{Hz}$ and below. Compared to electrical measurements available at the time (fig. 6.7b), this gave an order of magnitude improvement on the noise floor and on the total bandwidth. In fact, the noise floor in fig. 6.7a is artificially high, due to poor noise characteristics on the network analyzer we used to acquire the thermal spectrum.

The comparison of fig. 6.7a and 6.7b clearly shows that optical detection provides superior resolution. It is worth noting, however that the greater resolution is a consequence of the exponential nature of the evanescent field; which thus necessitates significantly tighter restrictions on both drift and positional accuracy. In this sense electrical detection and optical detection serve complementary roles, as electrical detection has logarithmic height dependence. We used capacitive feedback to help stabilize the tweezers within $200nm$ of the cavity, however particularly soft tubes have a tendency to stick down, either through thermal fluctuations or snap-in due to optical gradient forces.

The ability to readily monitor thermal fluctuations of the CNT, aside from the direct scientific benefit, is also an excellent feature in performing optical cooling or parametric amplification measurements; this way the effective resonance mode temperature can be measured directly. Finally, we note that this is an attractive technological achievement, we show that a single CNT coupled to a microdisk resonator can act as highly tunable resonant cavity modulator.

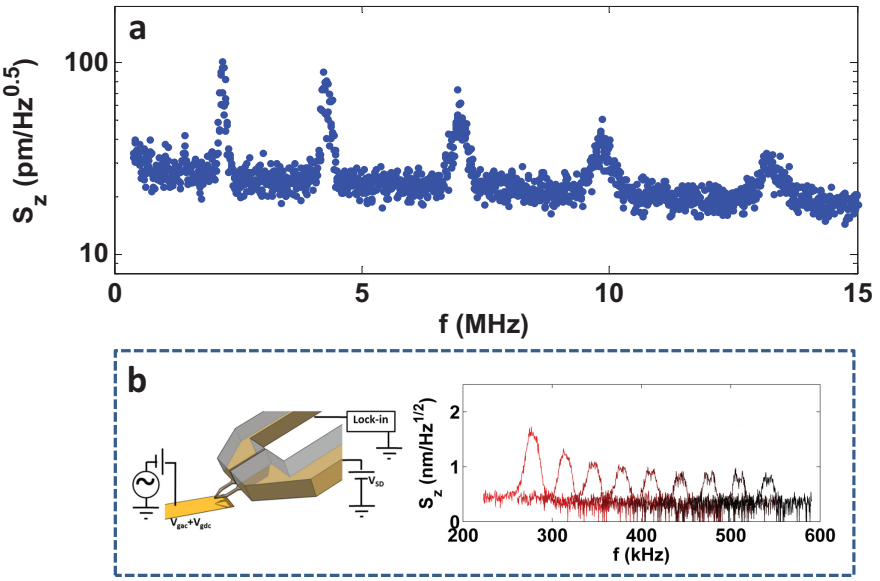

Figure 6.7: Optical detection of CNT thermal resonance. As in fig. 6.6, CNT is held in optical field and laser is detuned from resonance. Without electrical drive fast photodiode signal is measured with a spectrum analyzer. a) Resulting spectrum with apparent $30pm/\sqrt{Hz}$ noise floor. 5 optical resonances are measured, and as compared to electrical measures in comparable conditions b) The sensitivity of optical detection is supperior in bandwidth and noise-floor.

6.8.3 Dissipative optomechanics with CNT mechanical resonator

In our final section, we show our most recent results demonstrating the beginning stages of optomechanical manipulation of tweezer-coupled CNTs. Using the same tube measured in fig. 6.6, we pretension the CNT with a static gate voltage of $V_g = -8V$, and bring the CNT close to the cavity. Rather than sweep V_g at a fixed laser detuning, we turn up the laser power ($20\mu W$), drive the CNT resonance modes electrically, detect the response optically, and tune the laser frequency through the resonance. The response is plotted in fig. 6.8b. As the cavity resonance is approached, the cavity population increase, which therefore increases the optical detection sensitivity. As it approaches resonance there is an apparent sign flip. This is consistent with the optical spectra shown in fig. 6.8a, where near-resonance, the CNT decreases the cavity population, while far off-resonance, the CNT increases the cavity population.

When the laser is centered on-resonance, there is an observable frequency shift which is due to the optomechanical spring-effect: cavity radiation pressure imparts force on the CNT in phase

with its motion. As the laser frequency then passes off-resonance to the other side, the progression reverses until there is minimal light coupled into the cavity.

This is an exciting beginning for CNT optomechanics. While the spring-effect is effectively a quasi-static cavity modulation effect, the results are promising, and suggest that we can push the system into a stronger coupling regime and thus explore parametric amplification and optical cooling. In order to understand our current measurements and to assess the necessary changes to achieve dynamical coupling, we can model the CNT-cavity system from a particular manifestation of eqns. 6.3 and 6.4. Specifically we set the decay rate $\gamma = \gamma(x)$, and choose parameters consistent with our system, i.e. CNT mass, stiffness, and optical cavity energy and detuning. We show in fig 6.8c. the simulated CNT mechanical response as the optical cavity is tuned through resonance. There is good qualitative agreement, and further simulations demonstrate that a doubling of finesse will lead to optomechanical self-oscillations.

These results are indeed promising, and this line of work will hopefully serve as a launching point for technologically and scientifically rich studies involving carbon optomechanics.

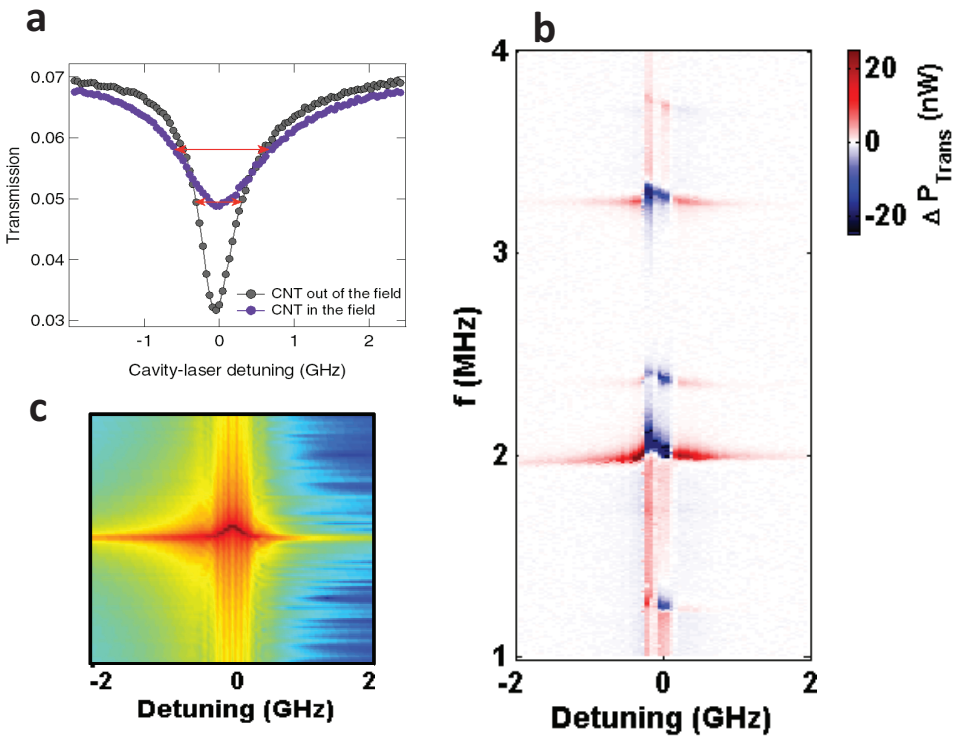

Figure 6.8: a) CNT optomechanics. Intrinsic optical cavity resonance (gray) and cavity resonance with CNT in contact (purple). In this case, the cavity is over-coupled to the optical fiber allowing for on-resonance photons to exit the cavity more easily with higher damping and thus leading to *less* total loss in the cavity withe greater damping. b) detected mechanical resonance of CNT as a function of laser detuning. There is a sign inversion on resonance for the same reason that the two curves in (a) cross. On resonance, there is a visible optical spring effect, where the resonance mode shifts up in frequency. c) simulated mechanicanical response for CNT-optical cavity system, with similar parameters to the measurement conditions in (b).

6.9 Conclusions

We demonstrated optomechanical coupling of a small-diameter carbon nanotube to a high-finesse optical microdisk resonator, and showed that the combination can reveal useful information about the individual components: CNT optical cross-section and optical cavity mode-shape. Further we demonstrated for the first time, the optical spring effect on a CNT resonator, meaning that with improvements of the optical cavity system, we will begin to observe optomechanical back-action. Looking forward, there are many fruitful avenues to pursue such as tuning the cavity to resonant excitonic states in the CNT, and back-action cooling of CNT resonance modes. Finally, with our enhance displacement detection capabilities, we may be able to study thermal and quantum

mechanical behaviors in CNT resonators with unprecedented resolution.

Chapter 7

Conclusions

We demonstrated both theoretically and experimentally how thermal fluctuations in freestanding carbon nanotubes can dramatically affect their resonance properties. This explains the longstanding observation that CNT resonators exhibit remarkably low observed quality factors at room temperature.

We performed time-dependent finite-element simulations of thermally fluctuating CNTs and showed that fluctuation broadening dominates the behavior of CNT resonators over a broad range of temperatures, and appears to be the main cause of temperature-dependent quality factors measured in both tensioned and untensioned resonators. Our theoretical understanding of these results draws on the ideas of polymer physics and underscores how thermal fluctuations can strongly modify the vibrational spectrum and decay widths in a general class of reduced dimensional nanoscale objects. While there has been limited experimental data characterizing Q over a broad temperature range in CNT resonators, experimental data remain at or below our theoretical upper bound [3, 4, 45]. We predicted a specific dependence of Q on ϵ_0 and T which can be tested by experiments that can independently control these parameters in individual CNT resonators [16].

This theoretical work demonstrated that varying ϵ_0 at a fixed T would be an informative way of studying fluctuation broadening in CNT resonators. This therefore motivated our design of a home-built micro-tweezer system that can make electrical contact to a freestanding, optically accessible CNT, with the ability to strain the CNT and move it in 3-dimensions. Employing electrical-

endpoint detection, we developed a reliable way of picking up CNTs, using electrical end-point detection to overcome the challenges presented by micromanipulation in SEMs. In this system, the tweezers are microfabricated as a passive element actuated by an external piezo, making this technique both cost-effective and easily transferable.

This system paved the way for diverse applications and measurements of CNTs outside the context of resonator measurements. In particular, we mounted the tweezers over an inverted microscope, and using optical imaging techniques, directly imaged CNTs in order to observe their optoelectronic and electromechanical behavior. We also laid the groundwork for using photocurrent-based optical tomography in order to reconstruct the position of a CNT with the motivation of using the CNT as a combined electrical and force detector in diverse environments.

Returning to our ultimate motivation, we used our microtweezer system in order to accurately strain and detect the vibrational properties of doubly-clamped CNT resonators. In the process we demonstrated the first-ever room temperature thermal measurement of a single-CNT resonator, and we performed the first-ever ringdown measurements on CNT resonators. Using this tool set, we found that fluctuation broadening accurately accounts for experimental observations. We then showed how, depending on the situation, fluctuation broadening can either function as a true energy dissipation mechanism or simply as a source of phase noise.

Finally, we explored the interactions of CNTs with optically resonant cavities. Coupling tweezer-held CNTs to the evanescent field of optical microdisk resonators, we showed how CNTs can be used to map the field of optical cavity modes, how optical cavities can operate as sensitive detectors of CNT motion, and how the mutual optomechanical coupling between cavity and CNT resonator can modify the CNT mechanical resonance properties. This work constituted the first observed optomechanical spring effect on a CNT resonantor and lays the groundwork for low-power on-chip electro-optical and all-optical modulators.

Appendix A

Micro-evaporator

The method used for picking up CNTs throughout this thesis primarily relied on van der Waals forces to hold the CNT in contact with the tweezers. This proves sufficient for the analysis discussed, however future applications could benefit from applying greater strain without slipping. We thus developed a micro-evaporator mounted directly within our cryostat. This allows us to pick up a CNT, measure it's properties, evaporate to form stronger contacts, and perform desired measurements without ever having to break vacuum.

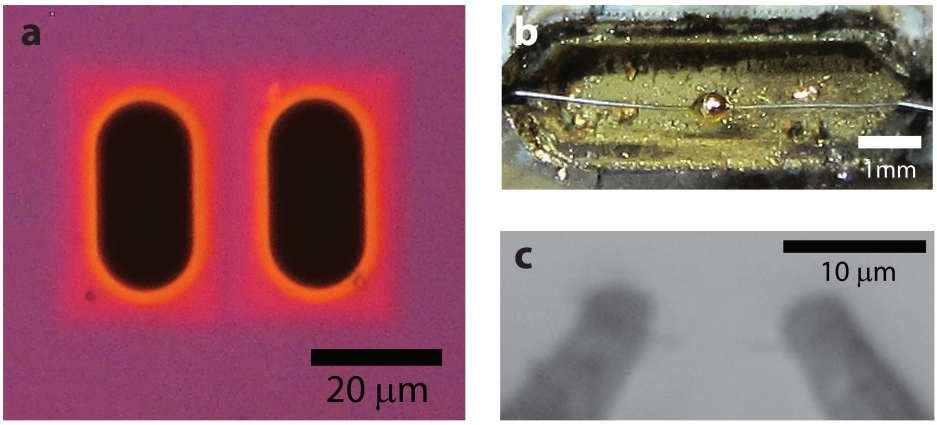

Figure A.1: Microevaporator system. a) Dual aperture windows for making stronger from CNT to tweezers. b) Thermal evaporation gold source. Volume of gold has been melted and located at the center of a .003" diameter Tungsten wire. c) A contiguous CNT that has been coated on both ends. The tube sits $\sim 5\mu m$ from the tip of the tweezers.

The evaporator design is a compact thermal evaporator where a tungsten wire serves as an ohmic heat source. The main body of the evaporator, seen partially in fig. A.1b, is a constructed out of fused-silica that has been patterned and etched with a CO_2 laser source. The evaporation metal source (gold in our case) is manually wrapped around the tungsten wire, and is subsequently melted during the first evaporation. This results in a bead centered on the tungsten wire as seen in fig. A.1b. In order to selectively metalize the tweezer contacts, and not contaminate CNT, there is a dual aperture shadow mask mounted above the metal source. The aperture shadow mask is constructed out of a nitride coated double-side polished silicon wafer using standard lithographic techniques.

By maneuvering the tweezers over the apertures, bringing the CNT into close proximity to the bridge between the apertures, and driving current through the tungsten wire, we are able to selectively deposit gold onto both the tweezers and select regions of the suspended CNT. The resulting structure, seen in fig. A.1c, is a contiguous CNT spanning the tweezers, where the edges of the CNT near the tweezers are made visible by a layer of gold, while the center region remains clear of gold.

While we were unable to fully test the robustness of these contacts at the writing of this thesis, the ability to evaporate sharp localized contacts onto CNTs *in situ* is an exciting prospect. This functionality significantly improves our ability to strain CNTs with our microtweezers and lays the groundwork for the attractive possibility of forming highly-local, scannable metal-CNT junctions.

BIBLIOGRAPHY

[1] H. W. C. Postma, I. Kozinsky, A. Husain, and M. L. Roukes. Dynamic range of nanotube- and nanowire-based electromechanical systems. *Applied Physics Letters*, 86(22), 2005.

[2] S. S. Verbridge, J. M. Parpia, R. B. Reichenbach, L. M. Bellan, and H. G. Craighead. High quality factor resonance at room temperature with nanostrings under high tensile stress. *Journal of Applied Physics*, 99(12), 2006.

[3] A. Eichler, J. Moser, J. Chaste, M. Zdrojek, I. Wilson-Rae, and A. Bachtold. Nonlinear damping in mechanical resonators made from carbon nanotubes and graphene. *Nature Nanotechnology*, 6(6):339–342, 2011.

[4] V. A. Sazonova. *A tunable carbon nanotube resonator*. PhD thesis, Cornell University, 2006.

[5] J. Chaste, A. Eichler, J. Moser, G. Ceballos, R. Rurali, and A. Bachtold. A nanomechanical mass sensor with yoctogram resolution. *Nature Nanotechnology*, 7(5):300–303, 2012.

[6] K. Jensen, J. Weldon, H. Garcia, and A. Zettl. Nanotube radio. *Nano Letters*, 7(11):3508–3511, 2007.

[7] G. A. Steele, A. K. Huttel, B. Witkamp, M. Poot, H. B. Meerwaldt, L. P. Kouwenhoven, and H. S. J. van der Zant. Strong coupling between single-electron tunneling and nanomechanical motion. *Science*, 325(5944):1103–1107, 2009.

[8] K. Jensen, K. Kim, and A. Zettl. An atomic-resolution nanomechanical mass sensor. *Nature Nanotechnology*, 3(9):533–537, 2008.

[9] B. Lassagne, D. Garcia-Sanchez, A. Aguasca, and A. Bachtold. Ultrasensitive mass sensing with a nanotube electromechanical resonator. *Nano Letters*, 8(11):3735–3738, 2008.

[10] J. Lischner and T. A. Arias. Material limitations of carbon-nanotube inertial balances: Possibility of intrinsic yoctogram mass resolution at room temperature. *Physical Review B*, 81(23), 2010.

[11] HY. Chiu, P. Hung, H. W. Ch Postma, and M. Bockrath. Atomic-scale mass sensing using carbon nanotube resonators. *Nano Letters*, 8(12):4342–4346, 2008.

[12] SJ Tans, ARM Verschueren, and C Dekker. Room-temperature transistor based on a single carbon nanotube. *Nature*, 393(6680):49–52, 1998.

[13] R. Martel, T. Schmidt, H. R. Shea, T. Hertel, and P. Avouris. Single- and multi-wall carbon nanotube field-effect transistors. *Applied Physics Letters*, 73(17):2447–2449, 1998.

[14] P. Avouris, Z. Chen, and V. Perebeinos. Carbon-based electronics. *Nature Nanotechnology*, 2(10):605–615, 2007.

[15] S. Ilani, L. A. K. Donev, M. Kindermann, and P. L. McEuen. Measurement of the quantum capacitance of interacting electrons in carbon nanotubes. *Nature Physics*, 2(10):687–691, 2006.

[16] A. W. Barnard, V. Sazonova, A. M. van der Zande, and P. L. McEuen. Fluctuation broadening in carbon nanotube resonators. *Proceedings of the National Academy of Sciences of the United States of America*, 109(47):19093–19096, 2012.

[17] A. N. Cleland and M. L. Roukes. Noise processes in nanomechanical resonators. *Journal of Applied Physics*, 92(5):2758–2769, 2002.

[18] Y. K. Kwon, S. Berber, and D. Tomanek. Thermal contraction of carbon fullerenes and nanotubes. *Physical Review Letters*, 92(1), 2004.

[19] E. H. Feng and R. E. Jones. Equilibrium thermal vibrations of carbon nanotubes. *Physical Review B*, 81(12), 2010.

[20] H. Jiang, M. F. Yu, B. Liu, and Y. Huang. Intrinsic energy loss mechanisms in a cantilevered carbon nanotube beam oscillator. *Physical Review Letters*, 93(18), 2004.

[21] P. A. Greaney, G. Lani, G. Cicero, and J. C. Grossman. Anomalous dissipation in single-walled carbon nanotube resonators. *Nano Letters*, 9(11):3699–3703, 2009.

[22] H. J. Dai, J. H. Hafner, A. G. Rinzler, D. T. Colbert, and R. E. Smalley. Nanotubes as nanoprobes in scanning probe microscopy. *Nature*, 384(6605):147–150, 1996.

[23] P. Kim and C. M. Lieber. Nanotube nanotweezers. *Science*, 286(5447):2148–2150, 1999.

[24] J. H. Hafner, C. L. Cheung, and C. M. Lieber. Growth of nanotubes for probe microscopy tips. *Nature*, 398(6730):761–762, 1999.

[25] C. M. Lieber. Carbon nanotube probes: Towards molecular resolution, functional imaging. *Journal of Neurochemistry*, 72:S44–S44, 1999.

[26] S. Iijima. Helical microtubules of graphitic carbon. *Nature*, 354, 1991.

[27] A. Xuereb, R. Schnabel, and K. Hammerer. Dissipative optomechanics in a michelson-sagnac interferometer. *Physical Review Letters*, 107(21), 2011.

[28] T. J. Kippenberg and K. J. Vahala. Cavity optomechanics: Back-action at the mesoscale. *Science*, 321(5893):1172–1176, 2008.

[29] A. A. Clerk, M. H. Devoret, S. M. Girvin, Florian Marquardt, and R. J. Schoelkopf. Introduction to quantum noise, measurement, and amplification. *Reviews of Modern Physics*, 82(2):1155–1208, 2010.

[30] M. Aspelmeyer, T. J. Kippenberg, and F. Marquardt. *Cavity Optomechanics Nano- and Micromechanical Resonators Interacting with Light*. Quantum Science and Technology. Springer, 2014.

[31] M. G. Raymer and C. J. McKinstrie. Quantum input-output theory for optical cavities with arbitrary coupling strength: Application to two-photon wave-packet shaping. *Physical Review A*, 88(4), 2013.

[32] S. M. Spillane, T. J. Kippenberg, K. J. Vahala, K. W. Goh, E. Wilcut, and H. J. Kimble. Ultrahigh-Q toroidal microresonators for cavity quantum electrodynamics. *Physical Review A*, 71(1), 2005.

[33] G. Anetsberger, O. Arcizet, Q. P. Unterreithmeier, R. Riviere, A. Schliesser, E. M. Weig, J. P. Kotthaus, and T. J. Kippenberg. Near-field cavity optomechanics with nanomechanical oscillators. *Nature Physics*, 5(12):909–914, 2009.

[34] P. B. Deotare, M. W. McCutcheon, I. W. Frank, M. Khan, and M. Loncar. High quality factor photonic crystal nanobeam cavities. *Applied Physics Letters*, 94(12), 2009.

[35] N. Fakhri, D. A. Tsyboulski, L. Cognet, R. B. Weisman, and M. Pasquali. Diameter-dependent bending dynamics of single-walled carbon nanotubes in liquids. *Proceedings of the National Academy of Sciences of the United States of America*, 106(34):14219–14223, 2009.

[36] V. Sazonova, Y. Yaish, H. Ustunel, D. Roundy, T. A. Arias, and P. L. McEuen. A tunable carbon nanotube electromechanical oscillator. *Nature*, 431(7006):284–287, 2004.

[37] S. P. Hepplestone and G. P. Srivastava. Phonon-phonon interactions in single-wall carbon nanotubes. *Physical Review B*, 74(16), 2006.

[38] P. A. Wiggins and P. C. Nelson. Generalized theory of semiflexible polymers. *Physical Review E*, 73(3), 2006.

[39] K. N. Kudin, G. E. Scuseria, and B. I. Yakobson. C2f, bn, and c nanoshell elasticity from ab initio computations. *Physical Review B*, 64(23), 2001.

[40] W.H. Press, S.A. Teukolsky, W. T. Vetterling, and B.P. Flannery. *Numerical recipes in C*. Cambridge University Press, 2nd edition, 1992.

[41] A. H. Nayfeh, D. T. Mook, and S. Sridhar. Nonlinear analysis of forced response of structural elements. *Journal of the Acoustical Society of America*, 55(2):281–291, 1974.

[42] W. G. Conley, A. Raman, C. M. Krousgrill, and S. Mohammadi. Nonlinear and nonplanar dynamics of suspended nanotube and nanowire resonators. *Nano Letters*, 8(6):1590–1595, 2008.

[43] M. I. Dykman and M. A. Krivogla. Classical theory of nonlinear oscillators interacting with a medium. *Physica Status Solidi B-Basic Research*, 48(2):497, 1971.

[44] H. J. R. Westra, M. Poot, H. S. J. van der Zant, and W. J. Venstra. Nonlinear modal interactions in clamped-clamped mechanical resonators. *Physical Review Letters*, 105(11), 2010.

[45] A. K. Huttel, G. A. Steele, B. Witkamp, M. Poot, L. P. Kouwenhoven, and H. S. J. van der Zant. Carbon nanotubes as ultrahigh quality factor mechanical resonators. *Nano Letters*, 9(7):2547–2552, 2009.

[46] X. Wei, Q. Chen, S. Xu, L. Peng, and J. Zuo. Beam to string transition of vibrating carbon nanotubes under axial tension. *Advanced Functional Materials*, 19(11):1753–1758, 2009.

[47] M. Hopcroft, T. Kramer, G. Kim, K. Takashima, Y. Higo, D. Moore, and J. Brugger. Micromechanical testing of SU-8 cantilevers. *Fatigue & Fracture of Engineering Materials & Structures*, 28(8):735–742, 2005.

[48] E. H. Conradie and D. F. Moore. SU-8 thick photoresist processing as a functional material for MEMS applications. *Journal of Micromechanics and Microengineering*, 12(4):368–374, 2002.

[49] H. F. Winters and J. W. Coburn. Surface science aspects of etching reactions. *Surface Science Reports*, 14(4-6):161–269, 1992.

[50] J. W. Liu, M. W. Shao, X. Y. Chen, W. C. Yu, X. M. Liu, and Y. T. Qian. Large-scale synthesis of carbon nanotubes by an ethanol thermal reduction process. *Journal of the American Chemical Society*, 125(27):8088–8089, 2003.

[51] R. W. Havener, A. W. Tsen, H. C. Choi, and J. Park. Laser-based imaging of individual carbon nanostructures. *NPG Asia Materials*, 3:91–99, 2011.

[52] P. Avouris, M. Freitag, and V. Perebeinos. Carbon-nanotube photonics and optoelectronics. *Nature Photonics*, 2(6):341–350, 2008.

[53] M. Freitag, Y. Martin, J. A. Misewich, R. Martel, and P. Avouris. Photoconductivity of single carbon nanotubes. *Nano Letters*, 3(8):1067–1071, 2003.

[54] N. M. Gabor, Z. Zhong, K. Bosnick, J. Park, and P. L. McEuen. Extremely efficient multiple electron-hole pair generation in carbon nanotube photodiodes. *Science*, 325(5946):1367–1371, 2009.

[55] D. Y. Joh, L. H. Herman, SY. Ju, J. Kinder, M. A. Segal, J. N. Johnson, G. K. L. Chan, and J. Park. On-Chip Rayleigh Imaging and Spectroscopy of Carbon Nanotubes. *Nano Letters*, 11(1):1–7, 2011.

[56] M. Y. Sfeir, F. Wang, L. M. Huang, C. C. Chuang, J. Hone, S. P. O'Brien, T. F. Heinz, and L. E. Brus. Probing electronic transitions in individual carbon nanotubes by Rayleigh scattering. *Science*, 306(5701):1540–1543, 2004.

[57] A. W. Tsen, L. A. K. Donev, H. Kurt, L. H. Herman, and J. Park. Imaging the electrical conductance of individual carbon nanotubes with photothermal current microscopy. *Nature Nanotechnology*, 4(2):108–113, 2009.

[58] K. Besteman, J. O. Lee, F. G. M. Wiertz, H. A. Heering, and C. Dekker. Enzyme-coated carbon nanotubes as single-molecule biosensors. *Nano Letters*, 3(6):727–730, 2003.

[59] G. Gruner. Carbon nanotube transistors for biosensing applications. *Analytical and Bioanalytical Chemistry*, 384(2):322–335, 2006.

[60] V. Sazonova, Y. Yaish, H. Ustunel, D. Roundy, T. A. Arias, and P. L. McEuen. A tunable carbon nanotube electromechanical oscillator. *Nature*, 431(7006):284–287, 2004.

[61] A. K. Huttel, G. A. Steele, B. Witkamp, M. Poot, L. P. Kouwenhoven, and H. S. J. van der Zant. Carbon nanotubes as ultrahigh quality factor mechanical resonators. *Nano Letters*, 9(7):2547–2552, 2009.

[62] R. Martel, V. Derycke, C. Lavoie, J. Appenzeller, K. K. Chan, J. Tersoff, and P. Avouris. Ambipolar electrical transport in semiconducting single-wall carbon nanotubes. *Physical Review Letters*, 87(25), 2001.

[63] C. Chen, S. Rosenblatt, K. I. Bolotin, W. Kalb, P. Kim, I. Kymissis, H/ L. Stormer, T. F. Heinz, and J. Hone. Performance of monolayer graphene nanomechanical resonators with electrical readout. *Nature Nanotechnology*, 4(12):861–867, 2009.

[64] M. Wu, A. C. Hryciw, C. Healey, D. P. Lake, H. Jayakumar, M. R. Freeman, J. P. Davis, and P. E. Barclay. Dissipative and dispersive optomechanics in a nanocavity torque sensor. *Physical Review X*, 4(2):021052 (11pp.), 2014.

[65] S. Imamura, R. Watahiki, R. Miura, T. Shimada, and Y. K. Kato. Optical control of individual carbon nanotube light emitters by spectral double resonance in silicon microdisk resonators. *Applied Physics Letters*, 102(16), 2013.

[66] S. Stapfner, L. Ost, D. Hunger, J. Reichel, I. Favero, and E. M. Weig. Cavity-enhanced optical detection of carbon nanotube Brownian motion. *Applied Physics Letters*, 102(15), 2013.

[67] J. Zhu, S. K. Ozdemir, YF. Xiao, L. Li, L. He, DR. Chen, and L. Yang. On-chip single nanoparticle detection and sizing by mode splitting in an ultrahigh-q microresonator. *Nature Photonics*, 4(2):122–122, 2010.